

Medical School, University of Crete

Doctoral Thesis

Multiparametric semi-quantitative and quantitative study of soft tissue tumors with advanced Magnetic Resonance methods

Author: Katerina Nikiforaki

*Supervisors: Apostolos Karantanas
Eelco de Bree
Kostas Marias*

A thesis submitted for the degree of Doctor of Philosophy in collaboration with the:

*Computational Bio-Medicine Laboratory
Institute of Computer Science (ICS), FORTH
Medical Imaging Department, PAGNI University Hospital*



March 23, 2020

Ιατρική Σχολή, Πανεπιστήμιο Κρήτης

Διδακτορική Διατριβή

**Πολυμετρική ημιποσοτική και ποσοτική μελέτη όγκων μαλακών μορίων
με νεότερες τεχνικές Μαγνητικού Συντονισμού.**

Συγγραφέας: *Κατερίνα Νικηφοράκη*

Επιβλέποντες: *Απόστολος Καραντάνας*
Eelco de Bree
Κωνσταντίνος Μαριάς

Μια διατριβή για την κατάκτηση του τίτλου διδακτορικών σπουδών σε
συνεργασία με το:

Εργαστήριο Υπολογιστικής Βιο-Ιατρικής

Ινστιτούτο Πληροφορικής (ΙΠ), Ι.Τ.Ε.

Εργαστήριο Ιατρικής Απεικόνισης, ΠΑΓΝΗ



March 23, 2020

Acknowledgments

Undertaking this PhD has been a truly life-changing experience for me and it would not have been possible to do without the support and guidance that I received from many people.

Firstly, I would like to thank my supervisor Professor A. Karantanas for his guidance, continuous encouragement and kind advice throughout my PhD research studies. I would like to thank him for always providing the most conducive conditions to work despite his overloaded work schedule.

I feel grateful to Professor Eelco de Bree for his immense support not only as a supervisor but also as a doctor of a close family member, always showing support in the most essential way.

I am deeply grateful to Professor Kostas Marias for kindly supporting me not only with his advice but also by sharing his way of addressing tribulations. His clarity of vision on research, critical thinking ability and dexterity in seeing through ideas from conception to realization has immensely helped me in learning how to perform research.

In particular, I would like to express my highest appreciation to my Professor Thomas G. Maris. It would never have been possible for me to take this work to completion without his incredible support, encouragement and, above all, his ability to share the enthusiasm and deep knowledge on all aspects of MR Imaging. Thank you for all the discussions held with a background sound of MR sequences.

I am also thankful to Professors I. Souglakos, A. Koutsopoulos and I. Seimenis for agreeing to be a part of the jury for the thesis defense. Thank you for your interest in improving our work with your insights.

I am grateful to have shared time with Dr E. Lagoudaki at her lab and watching the amount of effort that she allocates for each task. She has been very patient in explaining the complexities of identification of the histopathologic specific features in simpler terms and in helping me understand basic aspects and for provoking my interest in her field of expertise.

My sincere thanks also goes to Dr N. Papanikolaou and Professor A. Drevelegas for the time I have spent working by them and for having played a very significant role to gaining the background knowledge and experience that has been indispensable for me throughout this journey. I have resorted to this background at innumerable occasions.

I thank all the members of our team, G. Manikis , L. Kontopodis , G. Ioannidis, I. Karatzanis, E. Trivizakis, N. Tsiknakis, K. Spanakis, M. Venianaki, Th. Boursianis, G. Kalaitzakis, E. Tsiapa for working together and for sharing a very pleasant and fruitful collaboration and for creating an enviable working environment. They have all been very generous to me.

Πολυμετρική ημιποσοτική και ποσοτική μελέτη όγκων μαλακών μορίων με νεότερες τεχνικές Μαγνητικού Συντονισμού.

Σύνοψη

Οι όγκοι μαλακών μορίων αποτελούν μια ευρεία κατηγορία όγκων με διαβάθμιση στον βαθμό κακοήθειας. Ο ακριβής και έγκαιρος χαρακτηρισμός παίζει πολύ σημαντικό ρόλο στην καλύτερη διαχείριση του ασθενή και στην πρόγνωση της ασθένειας. Η απεικόνιση μαγνητικού συντονισμού (ΑΜΣ) αποτελεί την μέθοδο εκλογής για την προ-εγχειρητική εκτίμηση των όγκων μαλακών μορίων καθώς προσφέρει ειδική αντίθεση μεταξύ των ιστών μαλακών μορίων, προσφέρει απεικόνιση σε πολλαπλά επίπεδα και δεν ενέχει την χρήση ιοντίζουσας ακτινοβολίας. Σημαντικότερος λόγος όμως είναι ότι η πολύ-μεθοδική ΑΜΣ προσφέρει πληροφορία για την παθολογία του απεικονιζόμενου ιστού μέσω διαφορετικών μηχανισμών αντίθεσης εικόνες, καθένας από τους οποίους αναδεικνύει μια διαφορετική όψη του μικροπεριβάλλοντος του όγκου. Παρόλα αυτά ο τελικός χαρακτηρισμός του όγκου δίνεται από την ιστοπαθολογική εξέταση που αποτελεί απαραίτητο βήμα στην διαδικασία της διάγνωσης.

Η αντίθεση στις εικόνες ΑΜΣ δημιουργείται προσαρμόζοντας τις παραμέτρους της λήψης ώστε να αναδεικνύουν επιλεκτικά την επιθυμητή ιδιότητα του ιστού. Ειδικότερα η αντίθεση στις εικόνες απεικόνισης διάχυσης (DWI) συνδέεται με την κυτταροβρίθεια και την αιμάτωση όπως αυτά αποδίδονται από της αλλαγές στην δυνατότητα ελεύθερης διάχυσης των μορίων του νερού. Η δυναμική ακολουθία μαγνητικής επιδεκτικότητας αναδεικνύει τις περιοχές αυξημένης αγγειακής διαπερατότητας μέσω των δυναμικών εικόνων κατά την διάρκεια χορήγησης σκιαγραφικής παραμαγνητικής ουσίας. Εφόσον χαρακτηριστικά της αιμάτωσης μπορούν να βασιστούν σε απεικονιστικές τεχνικές τόσο αντίθεσης διάχυσης αλλά και δυναμικής ακολουθίας αιματικής διήθησης, με διαφορετική θεωρητική βάση η κάθε μία, μία μελέτη της συμφωνίας των αποτελεσμάτων αποτελεί αντικείμενο με ενδιαφέρον. Με δεδομένο ότι η ακολουθία αντίθεσης διάχυσης είναι επίσης ενδεικτική της κυτταροβρίθειας, αυτό την καθιστά ένα δυνατό εργαλείο στην μελέτη της επιθετικότητας του όγκου. Στην εργασία III παρουσιάζεται μια μελέτη σύγκλισης μεταξύ των δύο διαφορετικών τεχνικών (DWI-DCE) τόσο σε επίπεδο συμφωνίας με στατιστικά μεγέθη όσο και σε επίπεδο χωρικής συμφωνίας στα αποτελέσματα εντοπισμού των θέσεων μέσα στον όγκο της υψηλότερης κακοήθειας, καταλήγοντας σε έναν οπτικό οδηγό για την ανάδειξή τους οπτικά. Η εργασία IV αναφέρεται σε αναγνώριση νεκρωτικών, υποξικών ή περιοχών με αναπτυσσόμενο όγκο με βάση την καμπύλη ενίσχυσης ακολουθία DCE.

Ένα επίσης σημαντικό μέρος της απεικονιστικής διαδικασίας είναι οι T2 και T2* relaxometry τεχνικές καθώς παρέχουν μετρήσεις ειδικές για τον ιστό υπό εξέταση και δεν εξαρτώνται από τις παραμέτρους απεικόνισης. Για την διαδικασία της αξιολόγησης των μεθόδων, σε αυτό το μέρος της εργασίας απεικονίσθηκαν και ασθενείς με καλοήθεις λιπώδη νεοπλασμάτα για μετρήσεις αναφοράς. Αυτή η ανάλυση αφορούσε μόνο σε όγκους με λιπώδη σύσταση ή προέλευσης από λιπώδη ιστό, καθώς κατά την διάρκεια της συλλογής δεδομένων προέκυψε ότι στην πλειονότητά τους οι ασθενείς που εγγράφηκαν στην μελέτη να έχουν λιποσαρκώματα και επομένως αυτό το ανοιχτό προς έρευνα πεδίο μπορούσε να αντιμετωπιστεί από το συγκεκριμένο απεικονιστικό πρωτόκολλο και την συγκεκριμένη ομάδα ασθενών. Οι εργασίες II και IV συνάγουν συμπέρασμα για την ταυτότητα του απεικονιζόμενου ιστού και την σύσταση του όπως αυτή εμμέσως παρουσιάζεται στους δείκτες που προκύπτουν από τις T2 ακολουθίες πολλαπλών ηχών.

Η εργασία II εισάγει τον όρο Spin Coupling ratio (*SCratio*) ως μετρικό ενδεικτικό της ελάττωσης έντασης σήματος σχετιζόμενης με φαινόμενα σύζευξης στροφορμής σπιν (spin coupling) το οποίο αποτελεί γνωστό απεικονιστικό φαινόμενο στον υγιή λιπώδη ιστό σε εικόνες T2 αντίθεσης αλλά δεν έχει μελετηθεί η αξία του σαν βιοδείκτης για καλοήθειες ή όγκους λιπώδους αρχής όπως λιπώματα ή λιποσαρκώματα. Αυτός ο δείκτης έχει την δυνατότητα να χρησιμοποιηθεί για την αναγνώριση περιοχών αυξημένης ή μειωμένης κυτταρικής διαφοροποίησης μέσα σε ετερογενή νεοπλασμάτα προκειμένου να αποτελέσει προ-εγχειρητικό εργαλείο καθοδήγησης της βιοψίας. Αυτή η εργασία υποστηρίχθηκε από συμπεράσματα σε ομοιώματα που δημοσιεύτηκαν στην εργασία I.

Η εργασία V προτείνει μια συγκεκριμένη μεθοδολογία πολυεκθετικής προσαρμογής (Mexp) και αξιολογεί τα αποτελέσματα της με αντιπαραβολή με τα αποτελέσματα της ευρέως χρησιμοποιούμενης τεχνικής ILT σε ομοιώματα με σκοπό την αξιοποίηση της προτεινόμενης μεθόδου σε όγκους λιπώδους αρχής (εργασία VI). Η προτεινόμενη τεχνική έχει το πλεονέκτημα του χαρακτηρισμού του ιστού σε σχέση με τον αριθμό των διακριτών διαμερισμάτων όσον αφορά την χαλάρωση T2 σε επίπεδο εικονοστοιχείου και όσο σε επίπεδο ευρύτερης περιοχής ενδιαφέροντος όπως η μέθοδος αναφοράς, το οποίο αποτελεί σημαντικό στοιχείο για ετερογενή νεοπλασμάτα. Οι όγκοι λιπώδους αρχής με διαφορετικό βαθμό κακοήθειας εμφανίζονται με διαφορετικό μοτίβο χαλάρωσης συμπεριφορά στην προτεινόμενη τεχνική Mexp, και επομένως η προτεινόμενη τεχνική μπορεί να χρησιμοποιηθεί σε συνδυασμό με συμβατικές τεχνικές απεικόνισης για την προ-εγχειρητική εκτίμηση αυτών των νεοπλασμάτων.

Ένα νεότερο ογκολογικό πρωτόκολλο που περιλαμβάνει όλες τις προαναφερθείσες τεχνικές αξιοποιήθηκε στα πλαίσια αυτής της μελέτης και τα αποτελέσματα σε επίπεδο βιοδεικτών αξιολογήθηκαν ως προς την ικανότητα μη επεμβατικού χαρακτηρισμού του ιστού με

επιβεβαίωση από την ιστοπαθολογική εξέταση ώστε να δημιουργηθεί ένα σύνολο κλινικά σημαντικών βιοδεικτών. Η ιστοπαθολογική ανάλυση χρησιμοποιήθηκε για την κατηγοριοποίηση των ιστών που ήταν απαραίτητη για τις αναλύσεις των απεικονιστικών δεδομένων. Τα αποτελέσματα που παρουσιάζονται μπορούν να έχουν χρησιμότητα στην υποστήριξη της ακτινολογικής διάγνωσης και μπορούν επίσης να αποτελέσουν αποτελεσματικό εργαλείο για την επιλεκτική διαλογή ιστού από την προ-εγχειρητική βιοψία.

Multi-parametric semi-quantitative and quantitative study of soft tissue tumors with advanced MR techniques.

Abstract

Soft tissue tumors comprise a broad category of neoplasms with variable degree of malignancy. Accurate and early tissue characterization yields a vital role in patient management and disease prognosis. MRI is the imaging modality of choice for preoperative assessment of soft tissue tumors as it offers supreme soft tissue contrast, multi plane coverage and does not involve exposure to ionizing radiation. More importantly, multi modal MRI imaging offers insight into tissue pathology from a number of different contrast mechanisms each one highlighting a different aspect of tumor microenvironment. However, histopathologic correlation of MR findings is a necessary step for the validation of MR findings and definite tissue characterization.

Contrast on MR images can indirectly characterise these properties by adjusting image contrast to be dependent on a sought-after property of tissue. Specifically, contrast on DW images is related to cell density and vascularity as derived from water mobility in tissue. DCE dynamic protocol highlights areas of increased vascular permeability through dynamic imaging during contrast medium administration. Since biomarkers related to vascularity can be derived by both DCE and DWI methods based on different theoretical assumptions, a study of agreement attracts great interest. As DWI is also indicative of tissue cellularity, which along with vascularity/permeability, is a very powerful metric of tumor aggressiveness. In [paper III](#) a correlation study is presented between the two different methodologies (DWI-DCE) in terms of statistical correlation and spatial agreement for increased tumor malignancy and conclude to a visual guide of areas within the tumor with MR findings indicative of increased malignancy. Paper IV is a study of the different DCE enhancement patterns that are indicative of viable necrotic and hypoxic tumor sites.

Another robust quantitative MRI methodology dating from the early days of MR imaging is T2 and T2* relaxometry as it provides tissue specific metrics of magnetic properties, independent of acquisition parameters and thus indicative of tissue properties. For this part of the study benign lipoma patients were also enrolled and additionally phantoms were used for reference measurements. This study focused selectively on tumors of adipocytic origin as liposarcomas were the majority of soft tissue sarcomas in the patient cohort used in our study. [Paper II and V](#) inferred tissue identity and composition as manifested indirectly in multi echo T2 relaxometry measurements.

Paper II introduces Spin Coupling ratio (*SCratio*) metric indicative of signal loss related to the spin coupling phenomenon which is a known phenomenon for healthy adipose tissue (bright fat phenomenon) but has not been studied for other tissues of lipomatous origin, such as lipomas or liposarcomas. This marker has the potential to be used for identification of areas of increased / decreased tissue differentiation within a heterogeneous neoplasm and can be a helpful tool for pre-operative tissue characterization for biopsy guiding. The study was supported by preliminary phantom results published in paper I.

Paper V introduces a proposed methodology for multi exponential T2 relaxometry (Mexp) and validates the results also in comparison with the well-established ILT method on a phantom as a preliminary stage for the application of the proposed methodology to adipocytic tumors (paper VI). The proposed technique has the added advantage over the gold standard ILT method of producing voxel based parametric maps rather than ROI based T2 distributions, which is essential taking into account tissue heterogeneity. Lipomatous tumors with different degree of malignancy exhibit distinct behavior patterns as measured with Mexp, and thus the proposed method can be used along with conventional imaging methods for preoperative radiological assessment.

An advanced oncologic protocol hosting all abovementioned imaging techniques was deployed in this study and resulting biomarkers were validated with histopathologic assessment in order to constitute a set of robust and clinically relevant biomarkers for the characterization of soft tissue neoplasms. Histopathologic analysis results were used for final tissue classification, necessary for the analysis of MR findings. The results presented in this thesis are useful for supporting radiological diagnosis and can also be a useful tool for optimizing imaging-driven biopsies.

Original Papers

The thesis is built on the following papers:

- I. **The impact of spin coupling signal loss on fat content characterization in multi-echo acquisitions with different echo spacing**
Katerina Nikiforaki , Georgios C. Manikis, Themistoklis Boursianis, Kostas Marias, Apostolos Karantanas, Thomas G. Maris. Magn Reson Imaging 2017; 38.
- II. **T2, T2* and spin coupling ratio as biomarkers for the study of lipomatous tumors**
Katerina Nikiforaki, Georgios C. Manikis, Eleftherios Kontopodis, Eleni Lagoudaki, Eelco de Bree, Kostas Marias, Apostolos H. Karantanas, Thomas G. Maris
Physica Medica: European Journal of Medical Physics, Vol. 60, p76–82
- III. **Statistical and spatial correlation between diffusion and perfusion MR imaging parameters: A study on soft tissue sarcomas**
Georgios S. Ioannidis, Katerina Nikiforaki, Apostolos Karantanas
Physica Medica: European Journal of Medical Physics, Vol. 65, p59–66
- IV. **Pattern recognition and pharmacokinetic methods on DCE-MRI data for tumor hypoxia mapping in sarcoma**
Maria Venianaki, Ovidio Salvetti, Eelco de Bree, Thomas G. Maris, Apostolos Karantanas, Eleftherios Kontopodis, Katerina Nikiforaki, Kostas Marias
Multimedia Tools and Applications, vol. 77, no. 8, pp. 9417-9439, 2018
- V. **Inverse Laplace transform and multiexponential fitting analysis of T2 relaxometry data: a phantom study with aqueous and fat containing samples**
Georgios S. Ioannidis, Katerina Nikiforaki, Georgios Kalaitzakis, Apostolos Karantanas, Kostas Marias, Thomas G. Maris
European Radiology Experimental, March 2020
- VI. **A multiexponential T2 relaxometry study on benign and malignant adipocytic tumours**
Katerina Nikiforaki, Georgios S. Ioannidis, Eleni Lagoudaki, Georgios H. Manikis, Eelco de Bree, Apostolos Karantanas, Thomas G. Maris, Kostas Marias
(Under review, European Radiology Experimental)

Case Report

- I. **Perfusion and oxygenation changes after isolated limb perfusion with TNF- α in lower limb sarcoma**

Katerina Nikiforaki, Georgios C. Manikis, Maria Venianaki, Eleftherios Kontopodis, Eleni Lagoudaki, Thomas G. Maris, Kostas Marias, Eelco de Bree, Apostolos H.

Karantanas

Biomed Res Rev. 2018 Mar;1(1) : 101

Oral Presentations

The following preliminary reports were given at international/European meetings:

- I. **Visualizing sites of increased cellularity and high permeability in soft tissue sarcomas**
Katerina Nikiforaki, Georgios Kalaitzakis, Georgios Ioannidis, Thomas G. Maris, Kostas Marias, Apostolos Karantanas
Physica Medica: European Journal of Medical Physics, Vol. 52, p19
- II. **T2 and T2* relaxometry of benign and malignant lipomatous tumors**
Katerina Nikiforaki, Georgios C. Manikis, Eleni Lagoudaki, Maria Venianaki, Kostas Marias, Eelco Bree de, Thomas G. Maris, Apostolos Karantanas
Physica Medica: European Journal of Medical Physics, Vol. 52, p9–10
Published in issue: August 2018
- III. **Spin coupling signal loss correlates with differentiation grade of lipomatous tumors: Preliminary results**
Katerina Nikiforaki, Eleni Lagoudaki, Georgios C. Manikis, Eleftherios Kontopodis, Kostas Marias, Eelco Bree de, Apostolos Karantanas, Thomas G. Maris
Physica Medica: European Journal of Medical Physics, Vol. 52, p9
- IV. **A model-free approach for imaging tumor hypoxia from DCE-MRI data**
Maria Venianaki, Eleftherios Kontopodis, Katerina Nikiforaki, Eelco De Bree, Ovidio Salvetti, Kostas Marias :. In ACM Int Conf Proceeding Ser. Volume 28-June-01; 2016.
- V. **Improving hypoxia map estimation by using model-free classification techniques in DCE-MRI images**
Maria Venianaki, Eleftherios Kontopodis, Katerina Nikiforaki, et al. In IST 2016 - 2016 IEEE Int Conf Imaging Syst Tech Proc; 2016.
- VI. **Feasibility of fat fraction quantification by measuring J-coupling related signal modulation in multi echo fast spin echo sequences**
Katerina Nikiforaki, Themistoklis Boursianis, Georgios C. Manikis, Kostas Marias,

Apostolos Karantanas, Thomas G. Maris

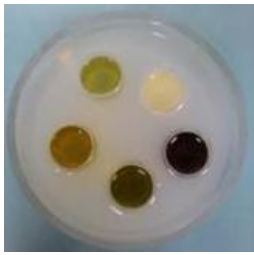
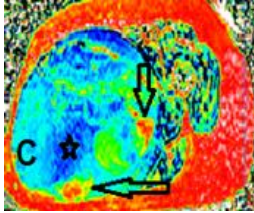
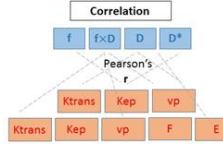
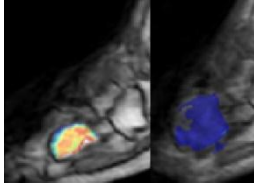
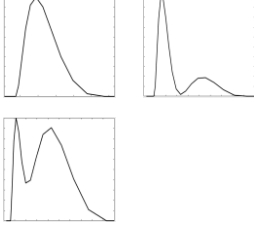
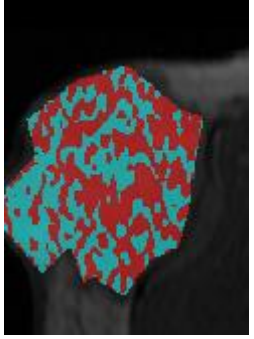
Physica Medica: European Journal of Medical Physics, Vol. 32, p249

Contents

Thesis at a glance	20
Acronyms.....	21
Chapter 1 Introduction.....	22
1.1 Epidemiology.....	22
1.2 MRI contribution	22
1.2.1 Assessment of cellularity.....	23
1.2.2 Assessment of vascularity	23
1.2.3 Response to treatment	24
1.2.4 Pre-operative biopsy planning	24
1.2.5 Assessment of microenvironment – phantom studies	25
1.2.6 Assessment of tissue microenvironment	26
1.3 Thesis Roadmap	27
Chapter 2 Soft Tissue Tumors	28
2. 1 Tumors of adipocytic origin.....	29
2.1.1 Dedifferentiated Liposarcoma	32
2.1.2 Pleomorphic Liposarcoma.....	35
2.1.3 Myxoid Liposarcoma	37
2.1.4 Atypical lipomatous tumor/well-differentiated liposarcoma	39
2.1.5 Lipoma.....	42
2.2 Tissue heterogeneity of malignant liposarcomas	44
Chapter 3 Advanced MRI imaging.....	52
3.1 Diffusion Weighted MRI (DW – MRI)	53
3.2 Dynamic Contrast Enhanced MRI (DCE-MRI).....	59
3.3 T2/ T2* relaxometry.....	63
Chapter 4 Statistical and spatial correlation between diffusion and perfusion MR imaging parameters on soft tissue sarcomas	70
4. 1 Motivation.....	70
4. 2 Method.....	71
4.3 Results	77
4.4 Discussion.....	82
Chapter 5 T2, T2* and Spin Coupling ratio as biomarkers for the study of lipomatous tumors	84
5.1 Motivation.....	84
5.2 Method.....	85
5.3 Results	90
5.4 Discussion.....	95

Chapter 6 Combined qualitative inverse Laplace transform and multi-exponential fitting study of T2 relaxometry data on a fat containing phantom: application of multi-exponential fitting on adipocytic tumors.....	97
6.1 Motivation.....	97
6.2 Method.....	97
6.3 Results	104
6.4 Discussion.....	111
Chapter 7 Conclusion	115
7.1 DWI – DCE imaging sequences.....	115
7.2 T2/T2* relaxometry sequences.....	115
7.3 T2 relaxometry sequence - Multi exponential methods.....	116
References.....	117

Thesis at a glance

Question	Method	Result	Figure	Conclusion
Impact of T2 relaxometry sequence ESP on fat quantitative imaging	Four MESE acquisitions with different ESP on a phantom with different fat samples	A threshold of approximately 20 ms for ESP differentiates acquisitions affected by spin coupling phenomena		Bright fat phenomenon is observed for ESP less than 20 ms
SCr related to signal loss because of scalar coupling and T2/T2* relaxometry as discriminators of lipomatous tumors	20 patients with benign and malignant adipocytic tumors imaged with 2 MESE of different ESP and MEGRE sequences	Proposed SCr biomarker has better classification performance than T2 and T2* relaxometry		SCr can provide valuable information for preoperative biopsy
Statistical and spatial correlation between DWI and DCE derived biomarkers in STS	25 patients with STS underwent DWI and DCE imaging in a 1.5 T scanner	f-IVIM and vp-GCTT were well correlated. Spatial agreement of DWI and DCE highlights areas suspicious of increased malignancy		Pre-operative DWI and DCE imaging can support diagnosis and facilitate interventional procedures
A case report: Assessment of response to locally aggressive neoadjuvant therapy	1 patient with lower limb sarcoma underwent advanced MR protocol before and after isolated limb perfusion with TNF-a	Ktrans, f and T2* voxel based histogram values had an overall shift, representing response to therapy		Advanced oncologic MR imaging can be used for assessing response to therapeutic procedures
Multi-exponential in comparison to Inverse Laplace method for T2 relaxometry	A phantom study comparing T2 relaxometry data with both methods	Strong agreement of the proposed multi-exponential method with the additional advantage of voxel based T2 mapping		Multi exponential T2 with no a priori assumption on the number of components can be used for robust T2 relaxometry
Multi exponential T2 relaxometry for the study of benign and malignant adipocytic tumors	T2 relaxometry study recruiting 25 patients with benign and malignant adipocytic tumors	Pure bi exponential behavior characterizes benign lipoma and liposarcoma of high degree of cell differentiation while more malignant adipocytic tumors have mixed mono and bi-exponential behavior		Adipocytic tumors of high malignancy requisite more complex fitting methods to highlight tissue heterogeneity

Acronyms

CPMG: Car Purcell Meiboom Gill

DCE: Dynamic Contrast Enhanced

DDLs: dedifferentiated Liposarcomas

DWI: Diffusion Weighted Imaging

ESP: Echo Spacing

ETM: Extended Tofts model

FNCLCC: Fédération Nationale des Centres de Lutte Contre Le Cancer

GCTT: Gamma Capillary Transit Time

GE: Gradient Echo

Hct: Hematocrit

ILT: Inverse Laplace Transform

IVIM: Intra-Voxel Incoherent Motion

MEGRE: Multi Echo Gradient Echo

MESE: Multi Echo Spin Echo

MLS: Myxoid Liposarcomas

PDLS: Poorly Differentiated Liposarcomas

PHAPS: Phase Alternating Phase Shift

SCr: Spin Coupling ratio

SE: Spin Echo

SNR: Signal to Noise

STT: Soft tissue tumors

WDLS: Well Differentiated Liposarcomas

WHO: World Health Organization

V_p: plasma volume

Chapter 1 Introduction

1.1 Epidemiology

Soft tissue can be defined as extraskeletal non-epithelial tissue of the body, represented by the voluntary muscles, fat, and fibrous tissue, the vessels serving these tissues and also the peripheral nervous system. Soft tissue sarcomas are relatively rare and constitute less than 1.5% of all cancers with an annual incidence of about 6 per 100,000 persons. Tumors arising from the soft tissue are classified by the line of differentiation, according to the adult tissue type that they resemble. Malignant tumors are also called sarcomas and, as opposed to benign soft tissue entities, are locally aggressive and are capable of invasive or destructive growth, recurrence, and also distant metastasis.

Sarcomas of adipocytic origin comprise the largest subtype of all sarcomas with a frequency of 1 in 5 sarcomas approximately. The degree of malignancy among liposarcomas ranges from low to high, and is assessed by applying a set of criteria during histopathologic analysis. Patients with a suspicion for a malignant soft tissue mass are referred for MR imaging as this is the modality of choice for supreme soft tissue contrast and imaging capabilities in multiplane planes. Moreover, advanced oncologic techniques offer the ability to adjust image contrast to a specific property of the tissue of interest and thus the MR acquisition can be tailored to the specific diagnostic needs of the patient for an individualized well targeted imaging acquisition.

1.2 MRI contribution

In the frame of this work, a prospective imaging protocol was set in order to examine a number of clinically relevant metrics for the characterization of soft tissue sarcomas based on imaging methods. Conventional T1 and fat suppressed T2 sequences in coronal and axial planes are usually used for the localization and the complete coverage of the lesion as a first step before proceeding to the sequences tailored for the quantitative part of the MR. In the frame of an advanced protocol, sequences tailored to be selectively sensitive to a specific tissue property are deployed, in order to highlight pathophysiological processes of clinical importance for diagnosis. Most common oncologic imaging targets are cellularity, vascular

permeability and tissue characterization on a sub-imaging scale. Apart from diagnosis, this information is very important for other subsequent diagnostic procedures, such as biopsy or for assessing tumor response to therapeutic interventions. The contribution of the imaging protocol utilized in this study are described in the sections below:

1.2.1 Assessment of cellularity

The MR sequence that is sensitive to the displacement of water molecules (diffusion) is based on T2-w sequence modified by the addition of two dephasing gradients symmetrically before and after the RF refocusing pulse serving to obscure the signal contribution from freely moving protons and highlight restricted motion. The degree of sensitivity to proton motion (b value) is adjusted by the proper choice of diffusion gradient amplitude and duration. Our diffusion imaging protocol comprised eight different diffusion weightings in order to comply with recommendations for imaging perfusion and thermal diffusion phenomena with the aim to decompose information from these two concurrent phenomena at a later post processing stage. B values were not chosen to be equidistant but they were chosen to sample the low b value area with higher frequency in order to capture the breaking point between the faster and slower decaying exponential signal and were more sparsely located at the higher b value area, with a maximum b of 1500. Such a protocol is suitable for almost all existing proposed models for biomarker extraction and thus it can serve for the purposes described within this work, but also can be suitable for further exploitation in the future.

1.2.2 Assessment of vascularity

Vascular properties of tissue can be visualized by perfusion sequences, which are sensitive to bulk blood flow and/or to the blood circulation at the level of the capillaries. Most widely used perfusion approaches entail the use of a gadolinium-based contrast medium that is intravenously administered to the patient. A sequential acquisition of consecutive dynamic T1-w phases before during and after the administration allow for the determination of the enhancement pattern of the contrast uptake. The resulting raw data, when combined with other imaging and clinical information allowed for the quantification of flow related parameters that are indicative of the vascular characteristics of the tumor.

1.2.3 Response to treatment

We also examined DWI and DCE combined results for the purposes of evaluation of response to treatment in a case report of a patient with an aggressive sarcoma of the foot who underwent administration of aggressive chemotherapy agent under conditions of isolated limb perfusion. The results showed that changes in tumor microenvironment following locally aggressive chemotherapy are evident in the parametric maps derived by both DWI and DCE techniques showing an overall shift in histogram based analysis to values representing non aggressive characteristics (viable tumor). At this case report we also briefly studied markers of hypoxia based on DCE enhancement curves and T2* relaxometry confirming the value of quantitative MRI to depict changes in tissue microenvironment concerning oxygen consumption. T2* histogram was accordingly shifted. This frame of analysis eloquently described changes happening at a microscopic scale that are manifested in metrics derived from imaging techniques with a multi-parametric protocol.

1.2.4 Pre-operative biopsy planning

The use of DWI derived information on tissue cellularity as well as the use of DCE derived information on tissue vascularity are very frequently used as surrogate markers of tumor aggressiveness. However, when examining a heterogeneous extensive mass it is important to examine if the two methods can reveal a common spatial component that exhibits characteristics of increased malignancy by both methods. This can serve as a guide for preoperative biopsy, reducing the possibility for sampling errors and tumor grade underestimation. To this end, we combined DCE and DWI data to serve a twofold purpose: firstly to identify possible correlations between biomarkers from the two different methodologies and secondly to localize voxels within the tumor area that have characteristics of increased malignancy based on both assumptions of increased cellularity based on restricted diffusion pattern and increased vascular permeability as indicated by DCE derived high K_{trans} values. The pair of biomarkers that exhibit the most statistically significant correlation was vp from the GCTT model on the part of DCE and f-IVIM from the DWI acquisition, expressing vascular tissue density within a voxel. Concerning the latter, for the majority of neoplasms voxels of both increased cellularity and permeability were not dispersed over the whole tumor volume but rather formed sub-areas within the tumor that could serve as indicative regions for optimal biopsy targets.

1.2.5 Assessment of microenvironment – phantom studies

Among the oldest and best established methods for examining tissue properties is T2 relaxometry as it attempts identification of tissue properties at a molecular level. By capturing the echo train evolution of transverse magnetization of a certain volume, suitable mathematical methods can attribute different relaxation patterns to distinct tissue compartments with an appropriate percentage, providing thus a description of tissue content. Moreover, a T2* sequence in selected echo times was used to acquire multiple in-phase and opposed phased images were collected to permit evaluation of T2* values and highlight areas of locally perturbed magnetic field.

Preliminary phantom studies were performed at two separate stages of the analysis process as a necessary step to test our methods prior to applying them on the patient cohort. The first phantom study aimed to approximate the most appropriate sequence setting in terms of echo spacing for producing bright and dark fat images on a set of different vegetable oil samples. The second stage where a phantom was necessary was for the application of multi-exponential analysis method of T2 relaxometry data for fat containing samples, in order to compare the results by the proposed method to the widely used method of inverse Laplace transform.

The first phantom used contained five different edible oil samples of different botanical origin for the analysis of T2 decay curve when T2 relaxometry sequences differ solely in the time interval between the successive RF refocusing pulses. Four sequences with echo spacing ranging from 6.7 to 40 ms and identical other sequence parameters were deployed for quantitative T2 relaxometry studies. The in-house built phantom contained liquid oil samples of different botanical origin and thus different composition. As expected based on theoretical calculations and earlier experimental studies, the results were similar among sequences with echo spacing above the threshold of 20 ms and similar between the two sequences with echo spacing below this threshold for all samples, but has significant differences among the two groups, underpinning thus the modulation of the echo train when spin coupling phenomena are allowed to evolve under the selected pulse sequence setting. Another interesting observation was that the amount of signal loss differed among samples, which can be explained on the basis of variable dependence of each fat resonance peak on the spin coupling related signal modulation. The result of this work was then used to optimize the T2 relaxometry scheme used for the patient study, with a set of two different echo spacing, one above and one below the verified threshold of 20 ms.

The second phantom used within the frame of this work was a phantom with aqueous, fatty an mixed samples in order to analyze the transverse relaxation behavior of fat containing samples and then use the results for T2 relaxometry for the analysis of similar data acquired from

patients with adipocytic tumors. A proposed multi exponential method requiring no a priori assumption on the number of exponential terms (limited to two) was implemented and compared to the widely used method of Inverse Laplace Transform for acquiring T2 spectrum of the sample verified the validity of the method. The advantage of the proposed method over the gold standard ILT is the ability for voxel-wise mapping and consequently the extraction of voxel based maps able to assess tumor micro-environment in terms of relaxation behavior and T2 components.

The phantom studies were performed in parallel and were adjusted to serve the purposes of validating and verifying results for extracting reliable information for the patient study. The endpoint of these preliminary studies was to provide useful regarding tissue heterogeneity as an indicative marker of malignancy.

1.2.6 Assessment of tissue microenvironment

Another quantitative MRI method deployed for the study of liposarcomas is the T2 and T2* relaxation technique as sensitive probes to tissue identity and tumor microenvironment characteristics. In particular, relaxometry was performed twice with a different ESP based on the results of the aforementioned phantom study that dictates that bright fat appearance requires ESP faster than 20ms. By keeping all other parameters identical between the two multi echo acquisitions and changing only ESP above or below the bright fat threshold we were able to measure the spin coupling effects on lipomatous tumors and introduce a new biomarker named SCr, standing for Spin Coupling ratio. After performing T2* relaxometry with a MEGRE sequence, we compared the classification performance of T2, T2* and SCr biomarkers for the classification of fat containing tumors of different degree of malignancy. Interestingly, SCr revealed potential to discriminate among almost all different adipocytic tumor subtypes, even between those of very similar radiological appearance, such as lipoma and well differentiated liposarcoma. In addition, another noteworthy finding was the discriminate power of T2 relaxation constant for identifying benign lipoma or well differentiated liposarcoma over subcutaneous fat. In conclusion this study evaluated the diagnostic value of T2/T2* relaxometry for adipocytic entities and in addition proposed a novel biomarker that specifically targets fat content of heterogeneous tumors.

Following the same direction, we used T2 relaxometry for obtaining T2 distributions of adipocytic tumors in order to identify the variable relaxation patterns of each subtype and based on the results to draw conclusions on the different relaxing (fast and slow) compartments of the tumors. The proposed method, as mentioned earlier, had been previously tested on a phantom with materials containing pure fatty, aqueous and mixed

samples in order to test the results in samples of known relaxation behavior as measured by gold standard methods. T2 relaxation curves were obtained per voxel for the volume assigned as tumor and a R2 based selection between one or two relaxation components was made in order to measure up to three independent variables (amplitudes and T2 constants) for each component. Benign neoplasms histopathologically identical to adipose tissue had a pure bi-exponential behavior at the entire tumor volume, as expected by the known relaxation pattern of fatty samples. Tumors of increased malignancy exhibited mixed mono- and bi-exponential behavior showing that tissue heterogeneity requires more complex relaxation fitting methods in order to account for myxoid, degenerative or fibrous components found within the adipocytic neoplasms. Apart from the number of distinct relaxation components, the T2 values themselves differed among the different tumor subtypes, with the myxoid group having the highest T2 relaxation constants attributed to the abundance of the gelatinous mucosal component.

To summarize, a multi-parametric advanced oncologic protocol applied to a group of patients with suspicion of tumor of the soft tissue was implemented in order to obtain information on the specific characteristics of each tumor subtype for supporting radiological decision-making and better preparation for needle core biopsy with the ultimate goal of accurate disease characterization and optimal patient management. Accurate pre-operative characterization of soft tissue tumors, embracing and addressing lesion heterogeneity, has been a long-lived diagnostic challenge for selecting the optimal therapeutic strategy that ensures the best possible outcome for the patient.

1.3 Thesis Roadmap

Firstly, in the following section (Chapter 2), a brief description of the pathological entities encountered during patient enrollment is given, with an illustration of the most significant radiological and histopathological findings that need to be identified in order to conclude on the specific subtype of pathology. Chapter 3 revises the most important quantitative MR methods used for clinical and research purposes that were used in order to extract information and attribute the characteristics of interest to the imaged volume. Then, the aim of the study is described in a concise manner based on the background and terminology described in Chapters 2 and 3. Chapters 4, 5 and 6 address the specific clinical questions raised and present the results and discussion related to them. Chapter 7 composes the final concluding aspect of this work as an epilogue. The extensive literature supporting arguments presented in this thesis is appended after the conclusions.

Chapter 2 Soft Tissue Tumors

Sarcomas can arise from a variety of soft tissues including fibrous connective tissue, fat, smooth or striated muscle, vascular tissue, peripheral neural tissue, and visceral tissue. Benign, intermediate and malignant soft tissue tumors can be differentiated histologically based on cell differentiation, mitotic activity and extent of necrosis. Rapid increase in current knowledge of the genetics and the cell biology of soft tissue tumors has led to recent changes in World Health Organization (WHO) classification of soft tissue tumors from 2013 relating to the allocation of known entities (Doyle, 2014). They comprise a vast category with more than 100 morphological types and subtypes. Malignant soft tissue tumors only represent 1% of all malignant tumors in adults with the largest subgroup of soft tissue tumors having adipocytic origin. Tumors were divided by the WHO into nine groups: adipocytic tumors, fibroblastic/myofibroblastic tumors, so-called fibrohistiocytic tumors, smooth muscle tumors, pericytic (perivascular) tumors, skeletal muscle tumors, vascular tumors, chondro-osseous tumors, and tumors of uncertain differentiation. The liposarcoma, which belongs to this subgroup is one of the most common malignant soft tissue tumors in adults.

The cohort of the present study comprised mainly of adipocytic tumors and thus the study focused on the unique imaging characteristics of this clinical entity as manifested in advanced MR Imaging techniques. Other more rare soft tissue tumors (alveolar sarcoma, Ewing sarcoma, malignant peripheral nerve sheath sarcoma, hibernoma) were imaged in the frame of this study but the number of each specific subtype was not sufficient for an extensive study.

2. 1 Tumors of adipocytic origin

Adipocytic tumors originate from mesenchymal cells and then differentiate to adipose tissue, without necessarily depending on fat cell maturation for tumor growth. These tumors can be highly heterogeneous, with the presence of non adipocytic components favoring a high-grade tumor diagnosis. Tumors of adipocytic origin comprise the vastest group of soft tissue tumors and can be both benign (lipomas) and malignant (liposarcomas). Liposarcomas, accounting for approximately 20% of all sarcomas, consist of a heterogeneous group comprising tumors with different degrees of adipocytic differentiation, ranging from well differentiated (well differentiated liposarcoma), to poorly differentiated (pleomorphic, dedifferentiated and round cell liposarcoma) as well as tumors with intermediate adipocytic differentiation (myxoid liposarcomas). The wide spectrum of pathologic appearances is also reflected in their clinical and biologic behavior, in terms of aggressiveness and metastatic potential.

Based on the FNCLCC scoring system (Table 1) evaluating tumor differentiation, mitotic count and percentage of tumor necrosis, each liposarcoma is characterized by a histological grade of malignancy which ranges from low (G1) to high (G3) ('WHO Classification of Soft Tissue Tumours', 2006). Histological type and grade are the most significant parameters in order to predict clinical behavior, i.e. rate of growth, possibility to metastasize, risk of recurrence and survival rate. Accuracy of the preoperative diagnosis, by means of identification the correct adipocytic tumor type, as well as the definition of its histological grade of malignancy, is essential for patients management as well as treatment planning (Callegaro *et al.*, 2018).

Table 1 FNCLCC Scoring system for soft tissue sarcomas

Factor	FNCLCC Scoring system
Differentiation	Score 1 (close similarity to normal cells) to score 3 (abnormal cell morphology)
Mitotic Count	Score 1 (low mitotic activity) to score 3 (high mitotic activity)
Extent of Necrosis	Score 0 (very little dying tissue) to score 2 (larger area of dying tissue)

In the case of a malignant soft tissue tumors (sarcomas), wide excision of the tumor together with a rim of adjacent healthy structures is the surgical treatment of choice to reduce the risk of local recurrence. Benign tumors on the other hand, are routinely treated by marginal resection (Casali *et al.*, 2018). Moreover, in sarcoma patients preoperative non-surgical treatment might be indicated (Callegaro *et al.*, 2018; Casali *et al.*, 2018). Unfortunately, nowadays accurate preoperative diagnosis is established only by tissue biopsy, usually core needle biopsy. However, biopsy procedures may be associated with patient’s discomfort and significant complications whereas in some cases the pathologist may not be able to determine the type of soft tissue tumor after examination of the biopsy samples (Mankin, Mankin and Simon, 1996). Hence precise non-invasive method for the differentiation between benign and malignant soft tissue tumors and the classification of their histological type is warranted.

Although definite diagnosis is established by biopsy, imaging techniques can offer very important information for their distinct characteristics in order to support diagnosis and optimize treatment. MRI in particular is superior to other imaging modalities, since it has multi-planar capabilities, a number of different contrast mechanisms for highlighting tumor morphology or function and lacks the use of ionizing radiation. Moreover, MR techniques have the ability to demonstrate even minute fatty tumor components and is able to stage soft tissue tumors accurately. The imaging differential diagnosis of adipocytic lesions is often extensive and includes non-neoplastic, benign and malignant entities, as presented in Table 2.

Table 2 Differential considerations in liposarcoma (adjusted from (Teniola *et al.*, 2018))

Imaging features	Differential Diagnosis (LPS)	Differential Diagnosis (non LPS)
Well defined fatty mass with non-fatty components	WDLS/DDLS	Angiomyolipoma, extramedullary hematopoiesis, fat necrosis, hemangioma, hibernoma, mature cystic teratoma, myelolipoma
heterogeneous mass with minimal fat	DDLS, Myxoid LS, Pleomorphic LS	Hibernoma
Fatty mass with thin septae	WDLS	Lipoblastoma, lipoma, retroperitoneal lipomatosis
Fatty mass with calcifications	WDLS, DDLS	Fat necrosis, hemangioma, heterotopic ossifications, lipoma, mature cyst teratoma
Fatty mass without well defined margins	WDLS, DDLS	Angiolipoma, fat necrosis, hemangioma, hibernoma, lipoblastoma, lipomatosis of nerve, massive localized lymphedema, mesenteric panniculitis, retroperitoneal

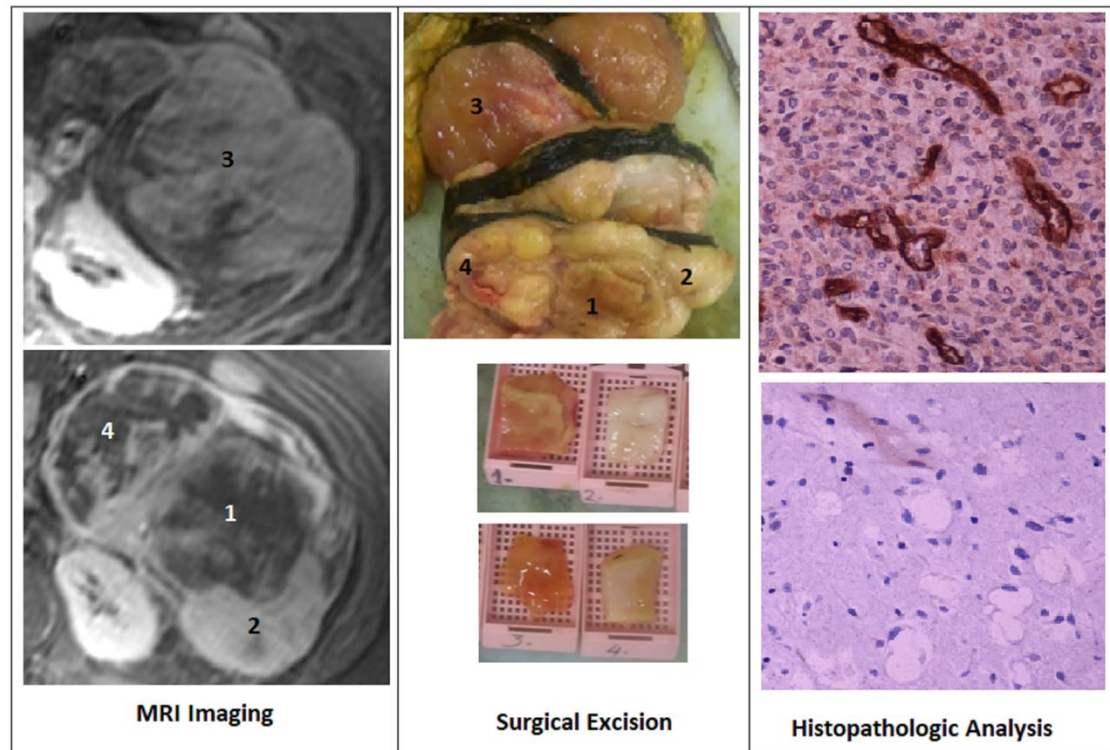


Figure 1 Diagnosis Workflow Steps followed during this study (images from dedifferentiated liposarcoma of the abdomen, female patient of 65y) Specimen 1: Necrosis, 2: poorly differentiated, 3: well differentiated, 4: moderately differentiated liposarcoma.

2.1.1 Dedifferentiated Liposarcoma

Dedifferentiated liposarcomas (DDLs) are malignant adipocytic tumors showing transition from atypical lipomatous tumor/well-differentiated liposarcoma (ALT/WDL) to a nonlipogenic sarcoma of variable histological grade. A small percentage of DDLs develop as a late complication of liposarcoma of lower grade or appear as 'de novo DDLs' meaning higher malignancy at the time of presentation (90%)(Gupta *et al.*, 2016).

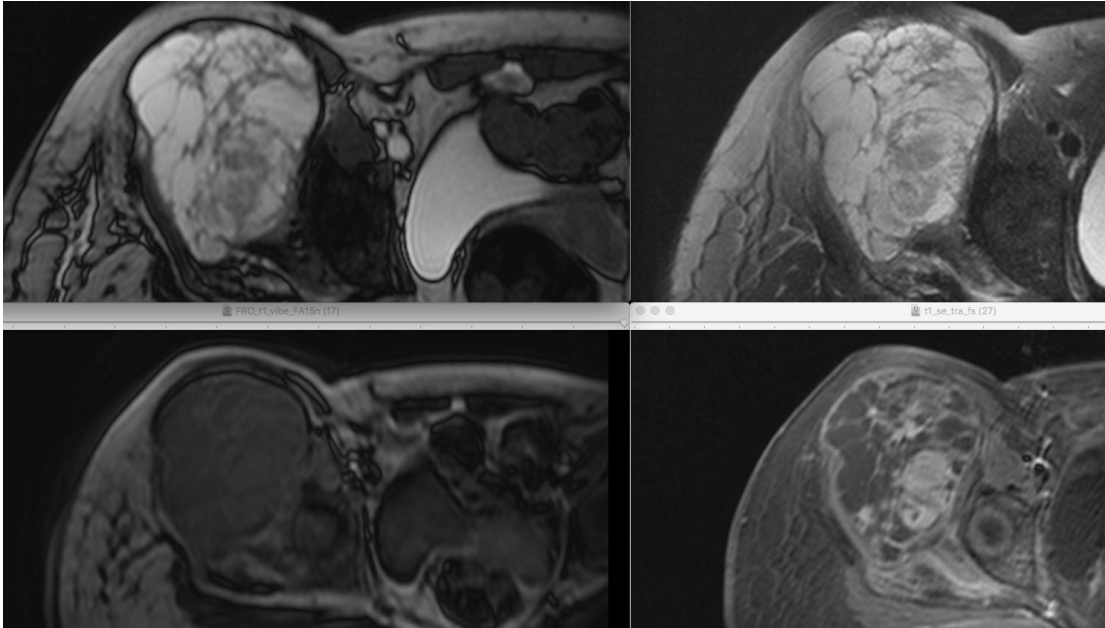


Figure 2 MR imaging of a dedifferentiated liposarcoma (Female patient, 67y, R. thigh) Above: TrueFISP and T2fat sat axial. Below: T1 GRE and T1 SE after contrast medium administration.

Considering the aggressiveness of dedifferentiated liposarcoma, therapeutic strategies include wide surgical excision in conjunction with radiotherapy or chemotherapy. It is of note that compared to other high grade pleomorphic sarcomas, dedifferentiated liposarcomas exhibit reduced aggressiveness and this can be attributed to the integrity of tumor suppression gene (tp 53)(Coindre, Pédeutour and Aurias, 2010). The vast majority of DDLs similar underlying chromosomal alterations (12q14–15 amplification involving *MDM2* gene) to well differentiated liposarcomas. This in turn shows the biological similarity among liposarcomas of different degree of differentiation representing a spectrum of the same disease. Often the spatial transition between the well and poorly differentiated areas is very abrupt and visually evident by difference in the color.

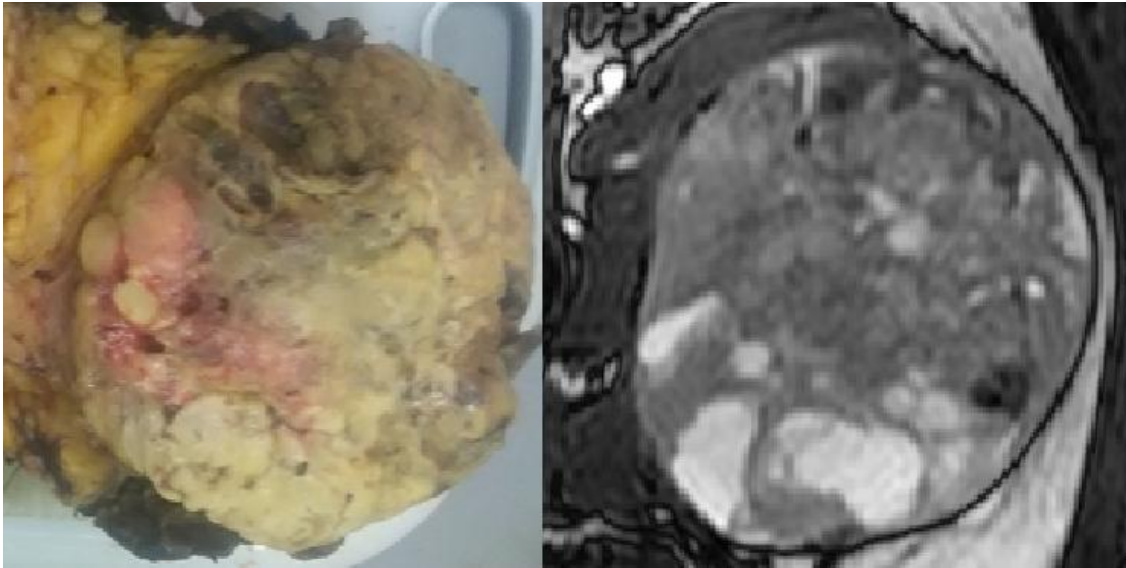


Figure 3 Surgical specimen and corresponding trueFISP slice of a dedifferentiated sarcoma (male patient, 40y, right thigh) where isles of well differentiated fat coexist with poorly differentiated fat. Hemorrhage and necrosis are also shown.

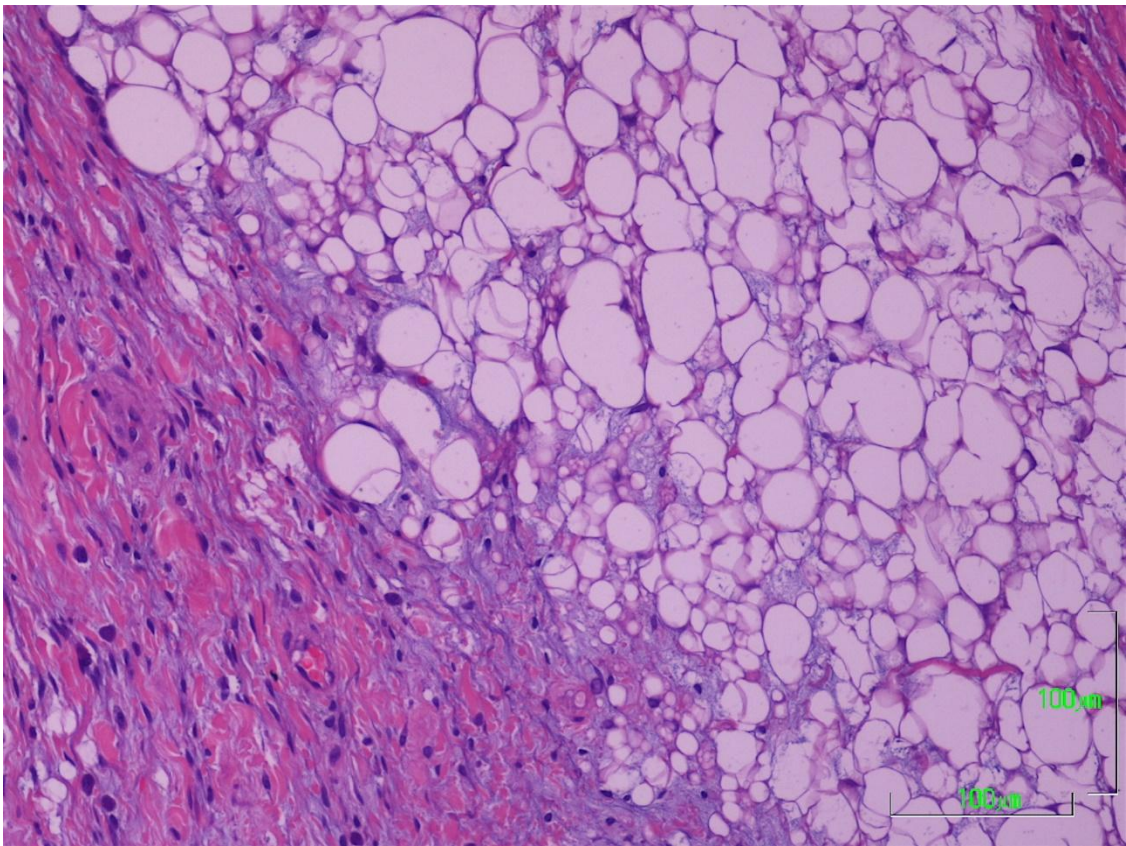


Figure 4 Abrupt transition between poorly and well differentiated liposarcoma (Female patient, 67y, R. thigh)

On MRI, ALT/WDL present as predominantly lipomatous tumors with thick septa (>2 mm), globular and/or nodular areas, and/or associated masses [6]. The nonlipomatous component has low signal intensity (SI) on T1-weighted images (T1WI) and various SIs on T2WI, depending on the type of tissue present. The thick septa or nodules enhance markedly after contrast administration. Dedifferentiation is suggested by the additional presence of a focal nodular nonlipomatous region greater than 1 cm in size with a low to intermediate SI on T1WI and intermediate to high SI on T2WI.

2.1.2 Pleomorphic Liposarcoma

Pleomorphic liposarcoma (PLS) is the least frequent liposarcoma (5%) characterized by increased malignancy, high metastatic potential and mortality. Identification of lipoblasts differentiates within the tumor differentiates it from other pleomorphic sarcomas. However, lipogenic differentiation may be focal only as linear, lacy or amorphous fat within the lesion. Lipoblasts are frequently very large and contain irregular, hyperchromatic, scalloped nuclei, with prominent nucleoli and multi-vacuolated cytoplasm. Genetically, pleomorphic liposarcomas have complex karyotypes with a high frequency of p53 mutations.

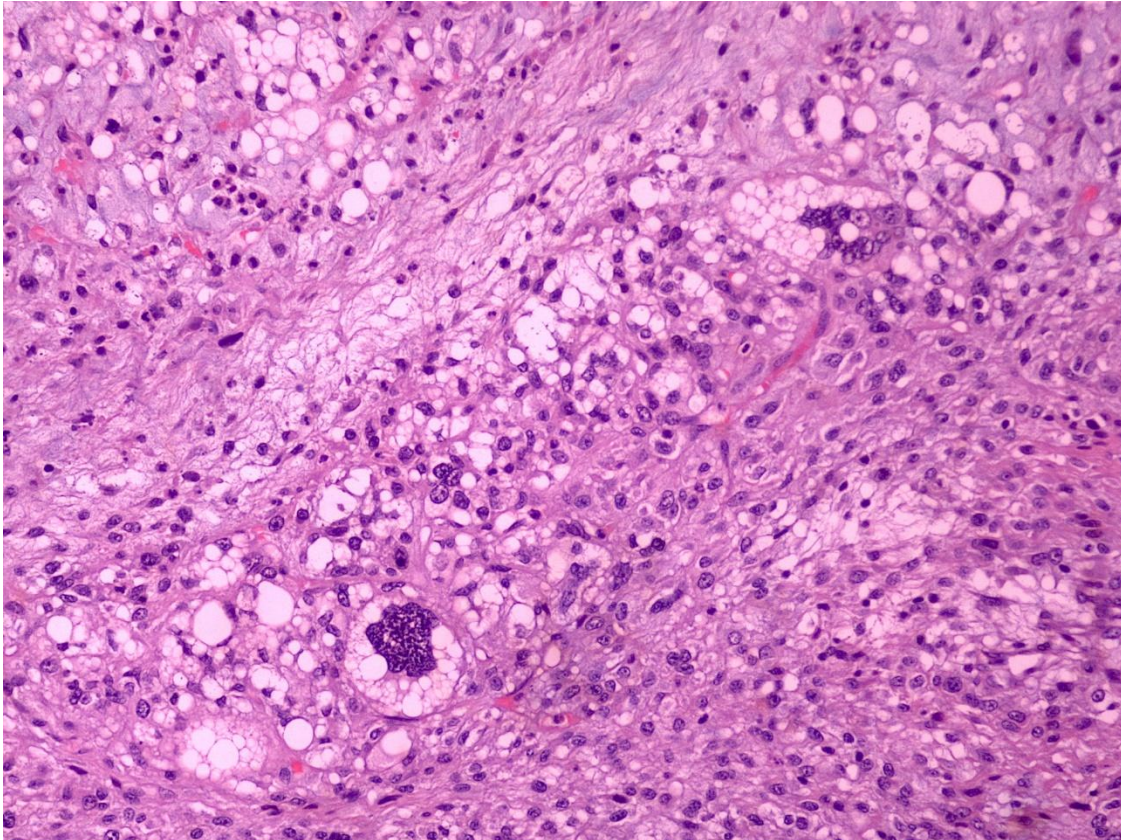


Figure 5 Pleomorphic lipoblasts (male patient of 58 y in the left shoulder)

At MR imaging, hemorrhage and/or extensive necrosis can be identified. They often do not contain a sufficient amount of fat to exhibit its radiological characteristics and therefore they exhibit low signal intensity on T1w images and high signal intensity in T2 weighted Spectral fat suppression may fail, suggesting different behavior and content from normal fat.

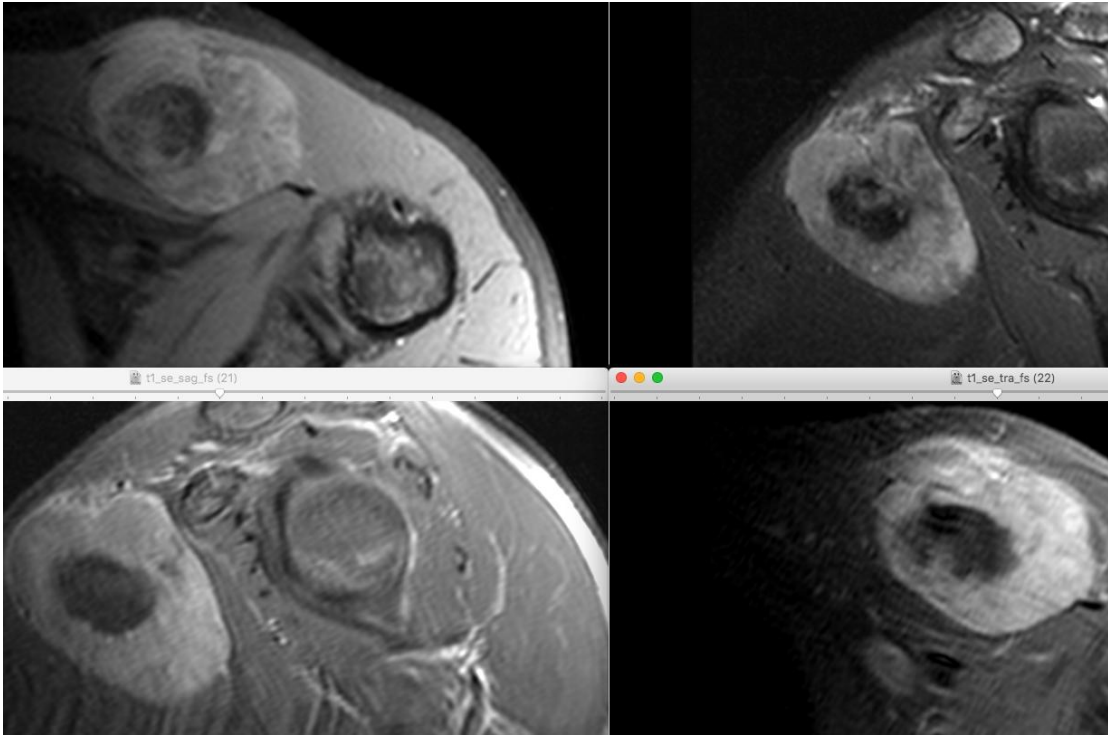


Figure 6 MR Imaging of a pleomorphic liposarcoma with an extensive area of necrosis (low signal intensity in all sequences) of a male patient of 58 y in the left shoulder. Above: PD fs axial, T2 fs sagittal. Below: T1 fat sat cor Below: T1 fat suppressed after contrast in sagittal and axial plane.

2.1.3 Myxoid Liposarcoma

Myxoid liposarcoma (MLS) comprehend a wide group of mesenchymal tumors and suggest the second most frequently encountered entity after well differentiated liposarcomas. They have a mixed composition of myxoid and round cell components, with the latter characterized by increased cellularity, higher mitotic activity and necrosis. They are characterized by solid sheets of primitive cells replacing the myxoid stroma and presenting a distinct vascular pattern (Murphey, Arcara and Fanburg-Smith, 2005). The myxoid components are presented as predominantly gelatinous lobules, with a delicate arborizing capillary network and primitive mesenchymal cells with variable number of lipoblast at the peripheries of the lobules. Myxoid and round cell components coexist in a variable degree and there is often a smooth transition from one to another, suggesting a histological continuum. Mature adipose tissue areas are sparse representing a small percentage of the tumor. The increased round part compartment above 5% increases possibility for metastatic disease and entails worse prognosis (Löwenthal *et al.*, 2013). High grade tumors are usually larger in size, encase large vessels and have a higher incidence of necrosis. Myxoid liposarcomas harbor a recurrent t(12;16) (q13;p11) translocation.

The extracellular mucoïd and myxoid compartments attract water from the blood supply which is trapped inside the lesion and is responsible for the cyst-mimicking appearance in MRI (Pai *et al.*, 2015) with high signal intensity in T2w images and extremely low in T1w. Hyperintense foci of lacy or linear shape can often be detected within the tumor, occupying a small percentage of its volume. These foci are composed of minute quantities of adipocytes and have the radiological characteristics of fat in all sequences. However, in contrast to cystic lesions, myxoid liposarcomas have prominent signal enhancement after contrast medium administration, with variable pattern (central, peripheral or diffuse enhancement)

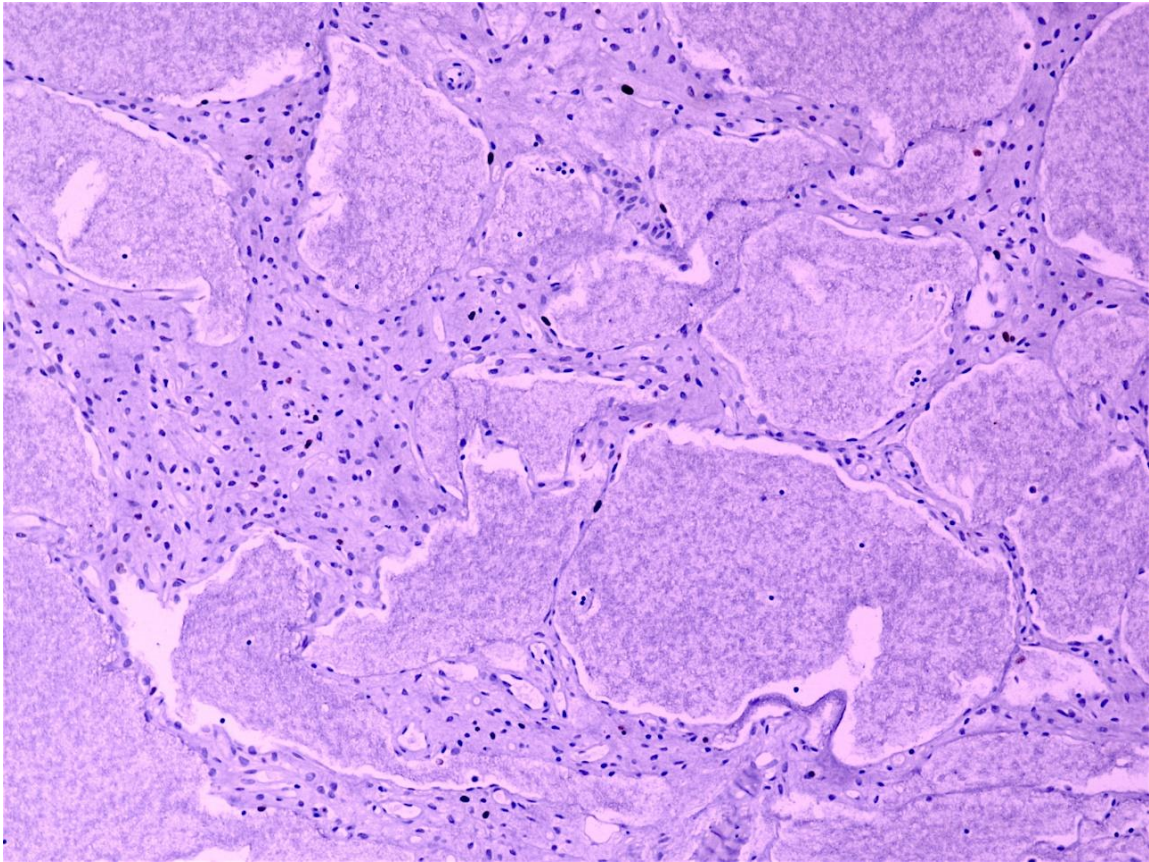


Figure 7 Ki-67 chromatin of a myxoid liposarcoma (Male, 35y, right thigh). Extensive myxoid areas are evident. magnification x 40

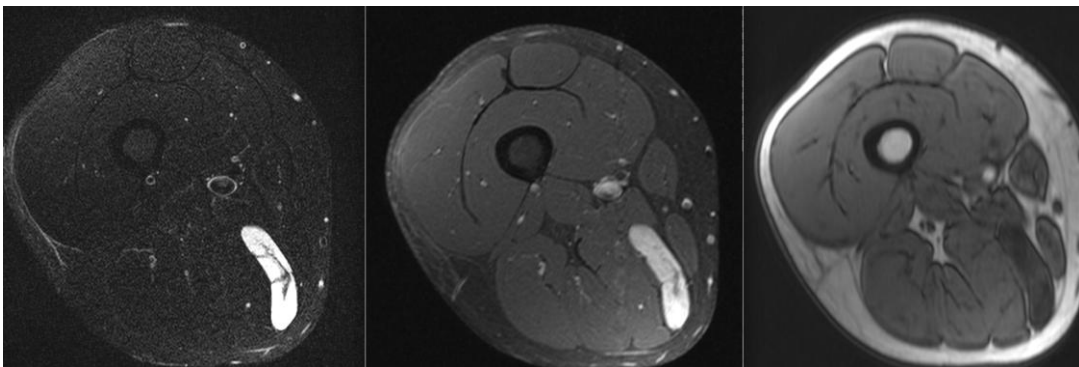


Figure 8 MR Imaging of a myxoid liposarcoma (Male, 35y, right thigh) From left to right: T2 STIR, T1 fat suppressed after contrast, T1 GRE.

2.1.4 Atypical lipomatous tumor/well-differentiated liposarcoma

Well differentiated liposarcomas (WDL) (which includes the adipocytic (or lipoma-like), sclerosing, inflammatory, and spindle cell variants) are low-grade malignant, locally aggressive mesenchymal neoplasms, accounting for approximately 50% of all liposarcomas. They usually arise in the deep soft tissues of the extremities (particularly the thigh) and less frequently in the retroperitoneum. Masses in the trunk (mediastinum/retroperitoneum) entail significant risk of local recurrence or metastasis (Mavrogenis *et al.*, 2011)(Henze and Bauer, 2013). On the contrary, WDLs of the extremities are often referred to atypical lipomatous tumors (ALT) reflecting less aggressive behavior of WDLs occurring at the limbs. The potential for dedifferentiation and conversion to a higher grade liposarcoma mandates accurate and prompt diagnosis.

They have predominantly adipose multi-lobulated and well circumscribed masses containing nonlipomatous components. Fat cells vary in size and there are also scattered lipoblasts and thick-walled blood vessels. Non lipomatous components are most often seen as prominent thick septa within the adipocytic part, characterized by limited morbidity and lack of significant potential for dedifferentiation. Differential diagnosis at the imaging stage includes benign lipomatous lesion or fat necrosis or less frequent findings such as intramuscular lipoma with atrophic muscle, normal fat with Lochkern (hole in the adipocyte nucleus) , spindle and pleomorphic cell lipomas, atrophy of fat or silicone reaction and more rarely localized massive lymphoedema associated with morbid obesity (Murphey, Arcara and Fanburg-Smith, 2005).

The key for the diagnosis of a WDL is mature adipocytic cells with a significant variation in size, associated with a variable number of atypical stromal cells. The latter appear to be more numerous in the fibrous regions (septae). The presence of lipoblasts (precursors of adipose cells) is not a frequent finding. Genetically, WDL are characterized by clonal abnormalities usually contain amplification of the 12q13–15 region (Fletcher *et al.*, 1996) constituting a distinction between WDL and benign lipomatous masses.

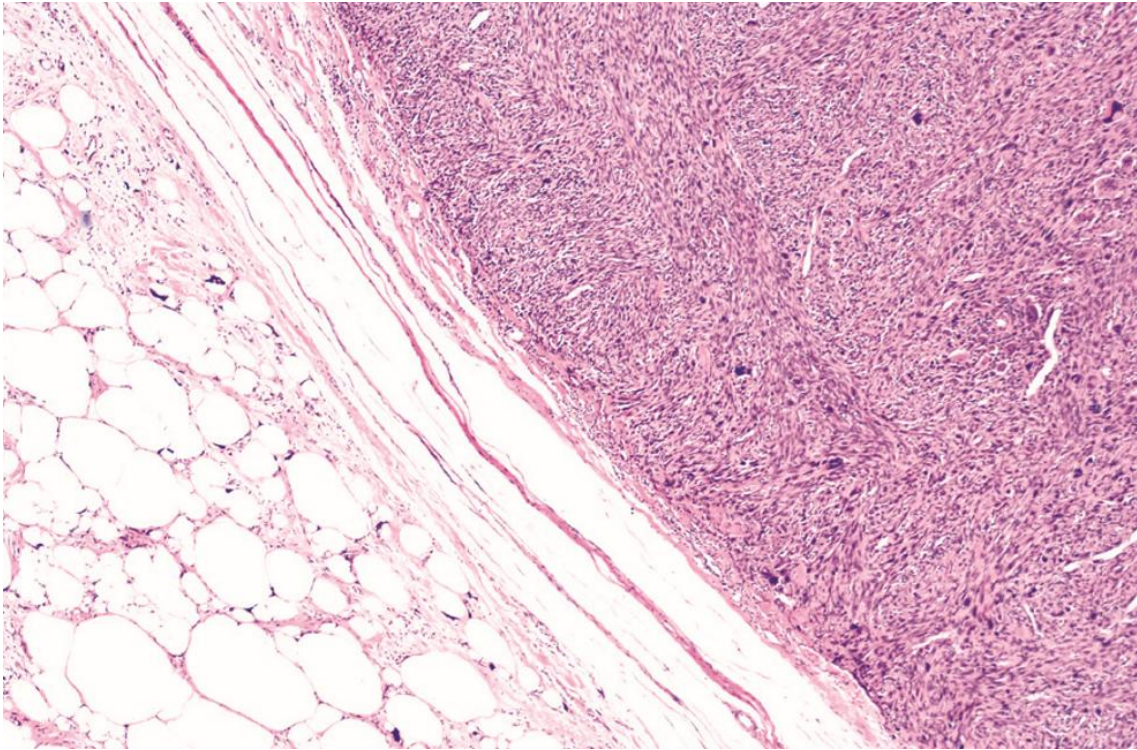


Figure 11 Well differentiated liposarcoma of a female patient, 84 y, in the right thigh (Ki-67,Magnification x 100)

Imaging findings of WDLS on conventional MRI is very similar to subcutaneous fat with high signal intensity in T1 and T2 images. However, they may also have thick septa, nodularity, internal cystic changes. This characteristics may account for signal intensity heterogeneity and areas of higher signal intensity in T2 images.

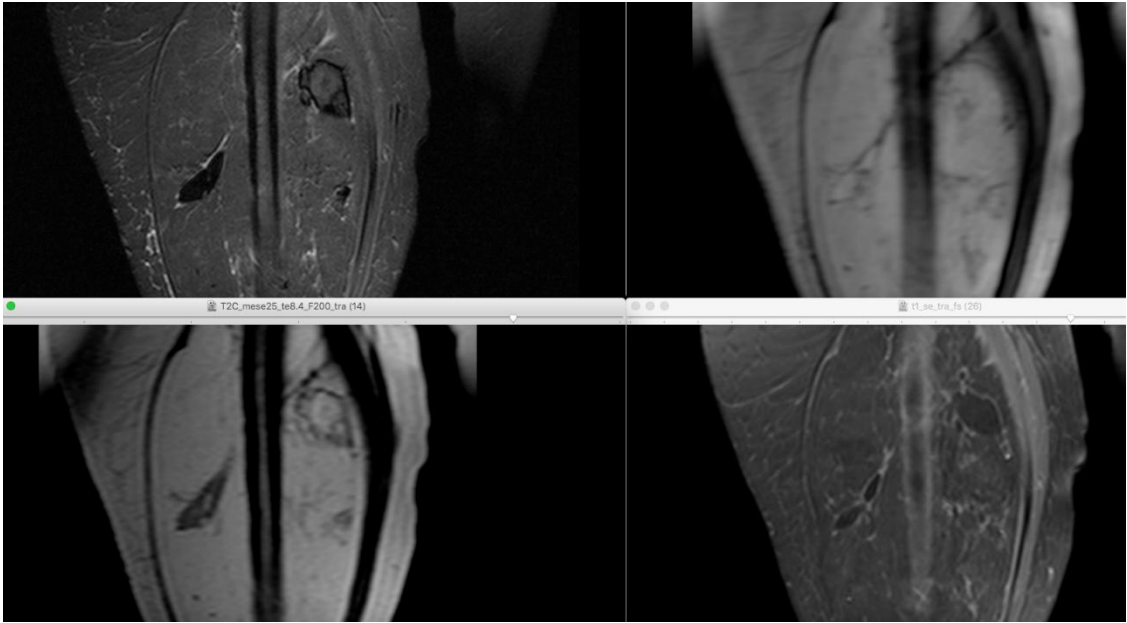


Figure 12 MRI of a well differentiated liposarcoma of the right thigh of a female patient, 84y. Above: T2 STIR, T1 GRE. Below: T2 MESE and T1 fat suppressed after contrast.

2.1.5 Lipoma

Lipomas are benign tumors of connective tissue composed of homogenous mature adipose cells (adipocytes), with gross appearance similar to subcutaneous fat. Normal adipose tissue and lipoma tissue is homogeneous, with intervening thin septae randomly distributed. They are monovacuolar cells containing a large lipid droplet surrounded by cytoplasm and the nucleus is flattened and located in the periphery of the cell. A typical size of a normal fat cell is 0.1mm. It is mainly composed of triglycerides and has the function of storing fat in a semi-liquid state. Lipomas are well vascularized, however this characteristic may not be readily apparent as vessels may be compressed by distended adipocytes.

Lipoma is itself a heterogeneous category as it also includes lipomatosis, lipomatosis of nerve, lipoblastoma, angioliipoma, myoliipoma of soft tissue, chondroid lipoma, spindle cell/pleomorphic lipoma, and hibernoma according to WHO classification. However, as differentiation between these entities is devoid of any clinical consequences this classification does not distinguish simple overgrowth of fat, true neoplasms or hamartomatous processes. Adipose cells in lipomas may have differences in composition as compared to subcutaneous fat, i.e. have increased levels of lipoprotein lipase. Lipomas may also contain a few thin septa of fibrous composition. The etiology is unknown and may occur at any age and sometimes one patient may have multiple lipomas. Lipomas originate from fatty tissue between the skin and the deep fascia, but are not attached to the overlying skin. Marginal resection is proposed as treatment in cases of symptomatic or lipomas of a size larger than 5 cm. Large size or lipoma location tethered to fascia can raise suspicion for a liposarcoma and consequently biopsy can be helpful.

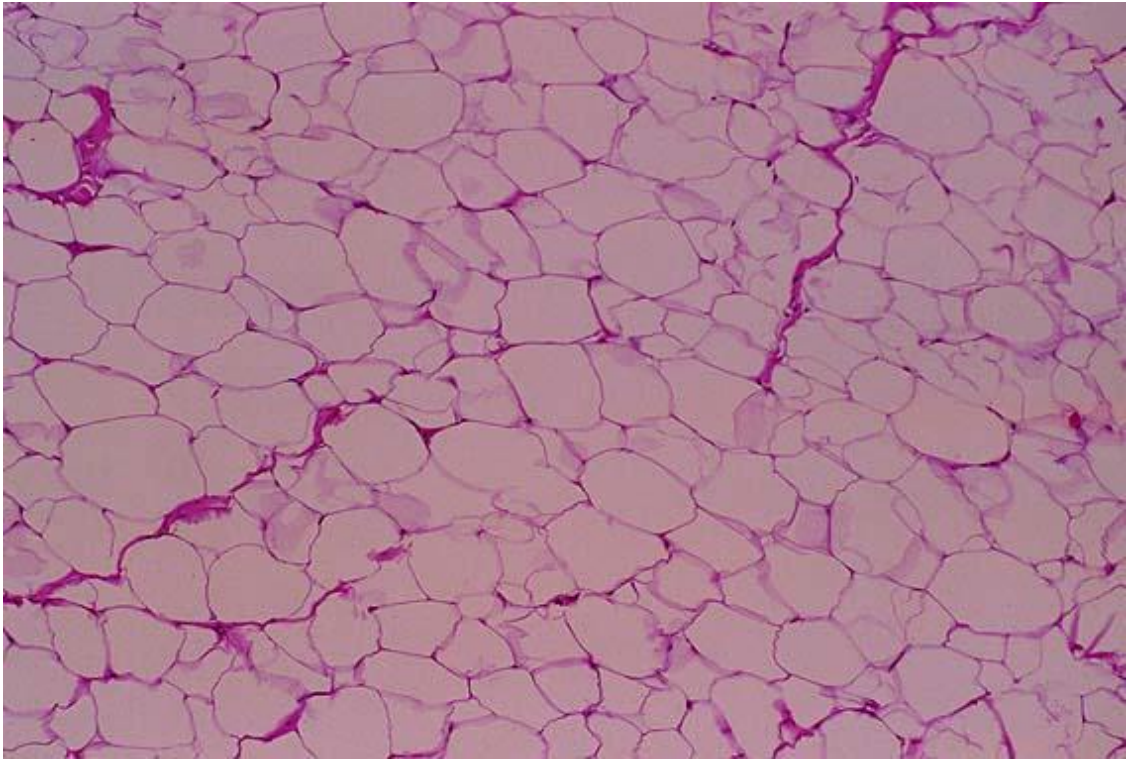


Figure 13 Normal adipose cells, magnification x 100

MRI appearance of benign lipomas resembles that of subcutaneous fat, presented with high signal intensity in both T1 and T2 sequences (short T1 and short T2 relaxation times) and also lacks signal enhancement after contrast medium administration. Setae are seen as low intensity strands on T1 images and have high signal intensity in T2w images probably because of blood vessels passing within them. Spectral profile is also similar to subcutaneous fat and consequently, signal is reduced in fat suppressed sequences. In this study lipomas were recruited in the analysis as reference tissue in respect to malignant liposarcomas.

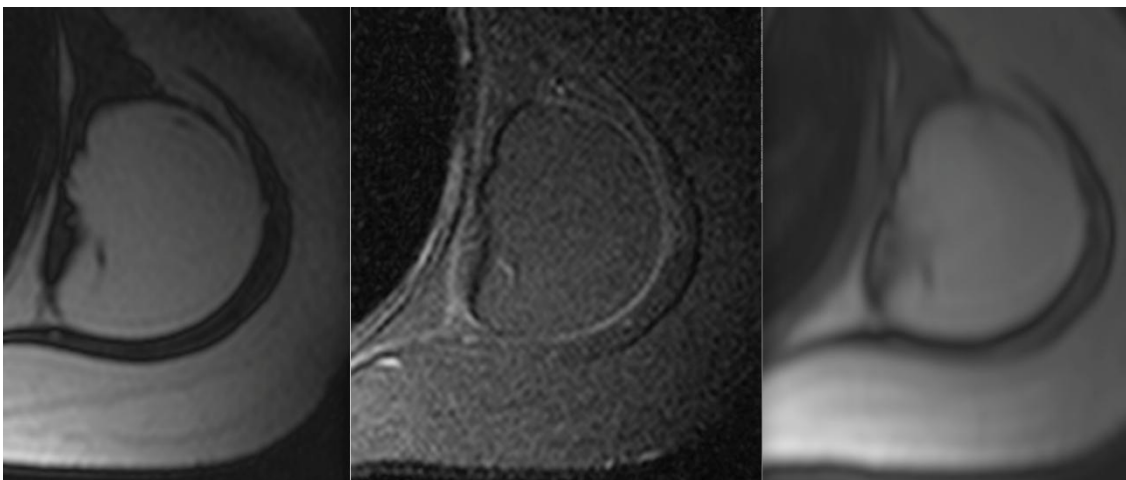


Figure 14 Lipoma of a male patient 63y on the left shoulder (From left to right: T2, T2 STIR and T1 sequences)

2.2 Tissue heterogeneity of malignant liposarcomas

In the following section, a number of histopathologic images is presented showing the large local tissue heterogeneity that characterizes malignant liposarcomas. Considering that each image is at least two orders of magnitude from a voxel of a high resolution MR image and that the measured signal is the spatial average of all components present in the volume of interest. As seen in figures 15-21 many pathologic entities co-exist within a heterogeneous malignant tumor, depending on its specific subtype. In figure 22, considering that its dimensions are at least one order of magnitude below the dimensions of a pixel, it is made obvious that the obtained signal carries information from a variety of different tissue types that needs to be accordingly post processed with mathematical methods in order to be indicative of the voxel composition. However, advances in scanner hardware as well as software capabilities and mathematical methods have rendered possible the extraction of information at sub-millimeter scale non-invasively. The main histopathologic findings present in a liposarcoma of high malignancy are presented as indicative imaging targets sought by the acquisition techniques that are described in the following chapter. All images have been collected at the Pathologic Department of the University Hospital of Crete and are published with their permission.

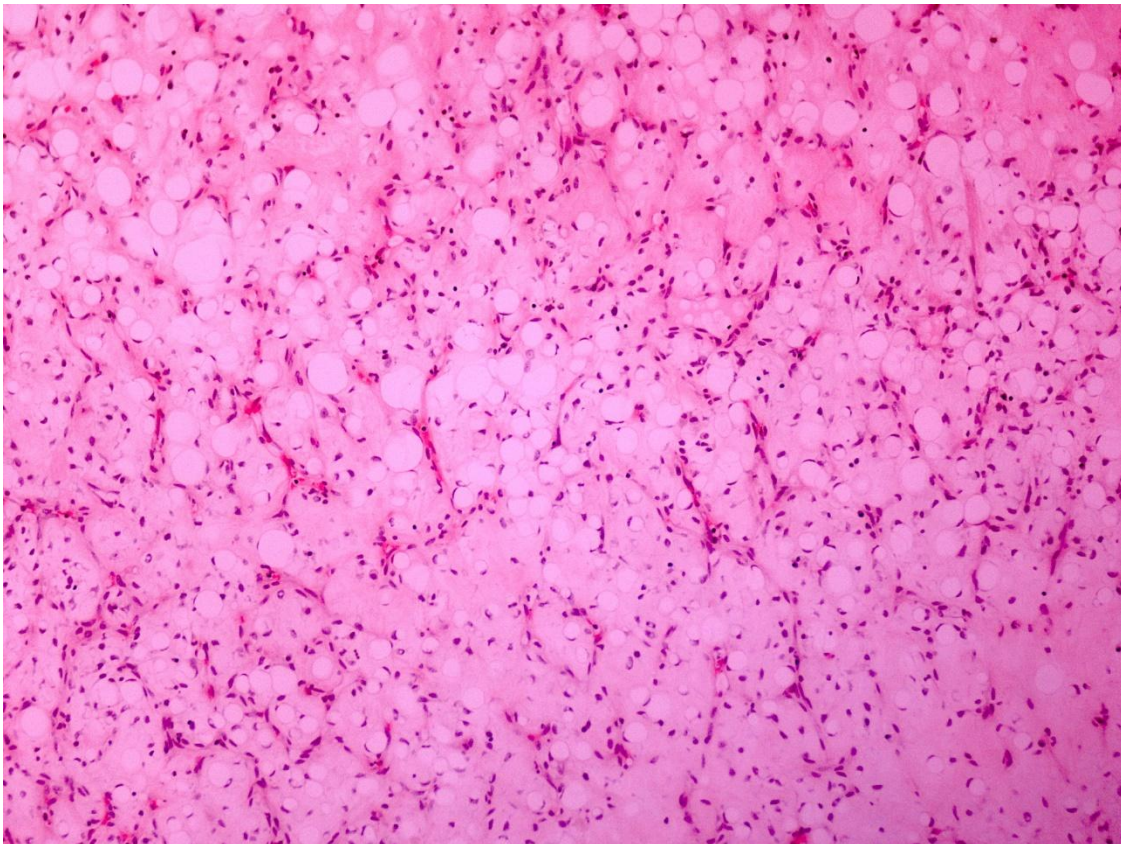


Figure 15 The presence of lipoblasts is necessary for the diagnosis of a myxoid liposarcoma

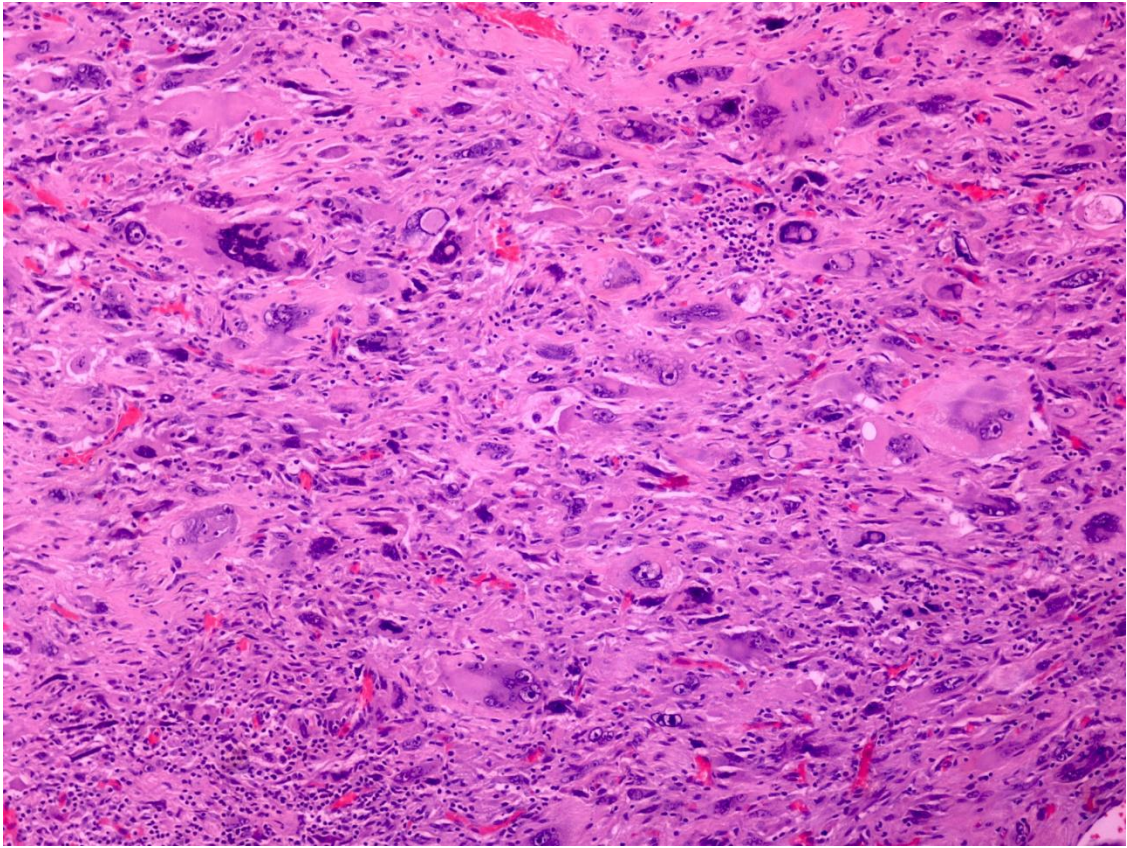


Figure 16 Important findings of a pleomorphic liposarcoma: Dense vascular network, presence of lipoblasts, inflammation, nuclear atypia

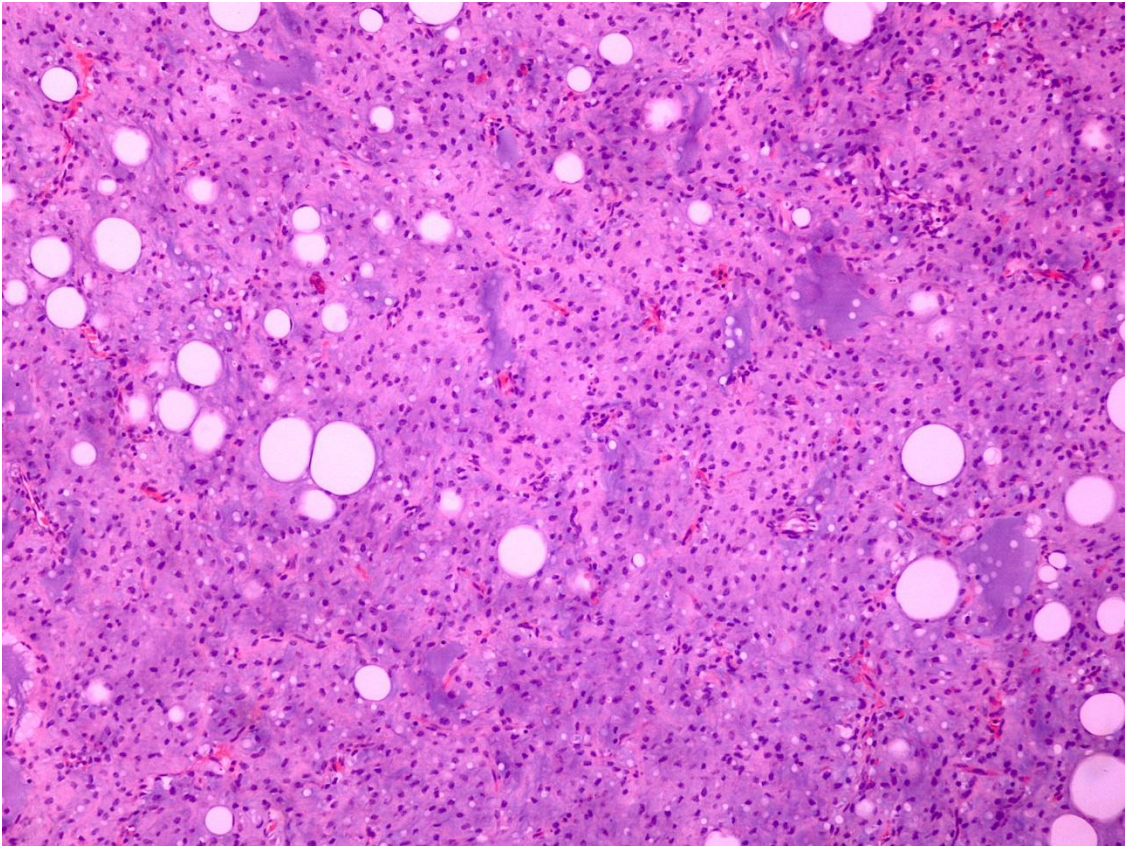


Figure 17 Viable highly cellular liposarcoma with sparse presence of lipoblasts

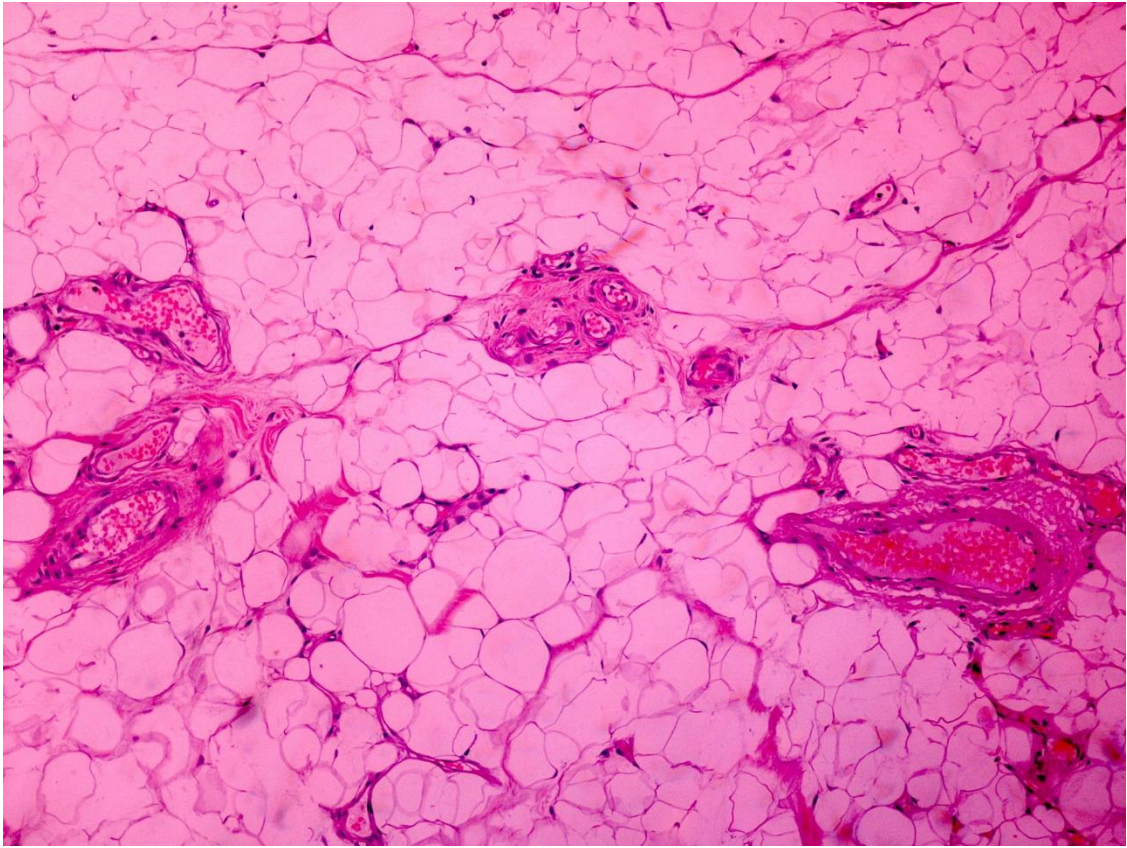


Figure 18 Vascularized adipocytic component

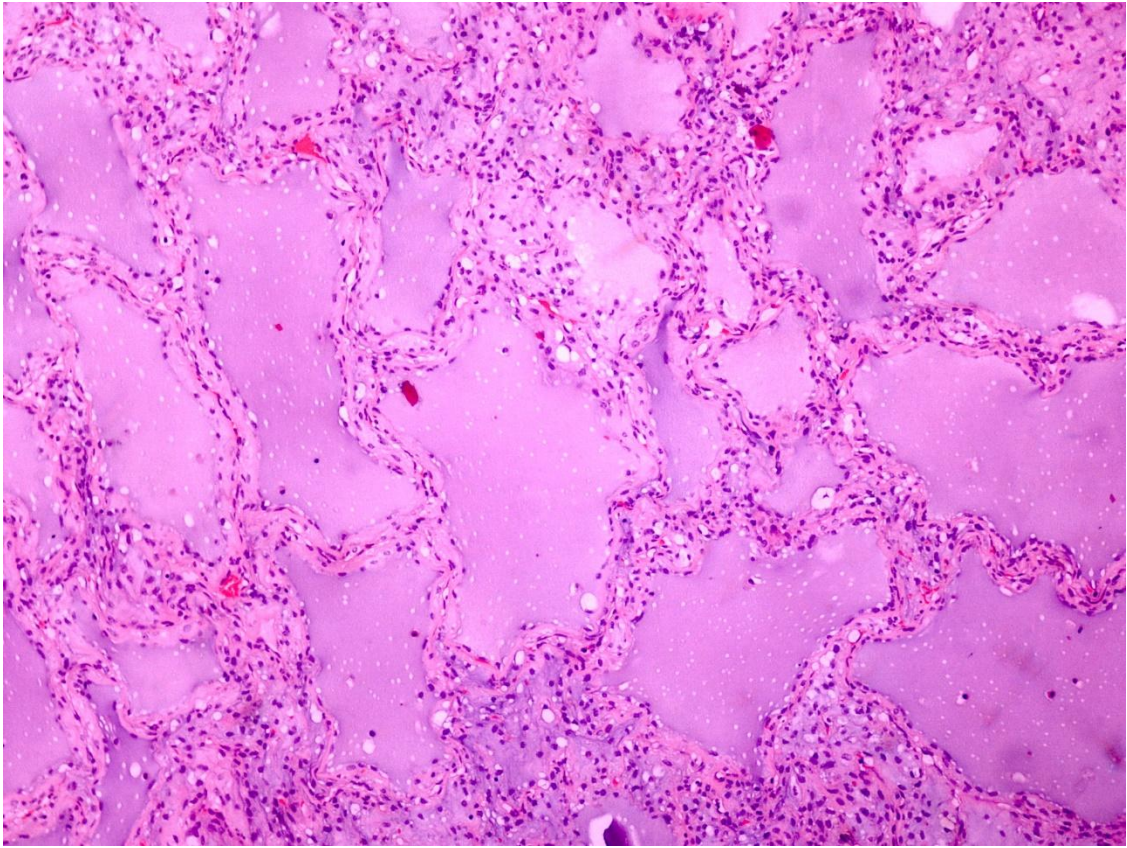


Figure 19 Cystic component of myxoid liposarcoma with alveolar pattern

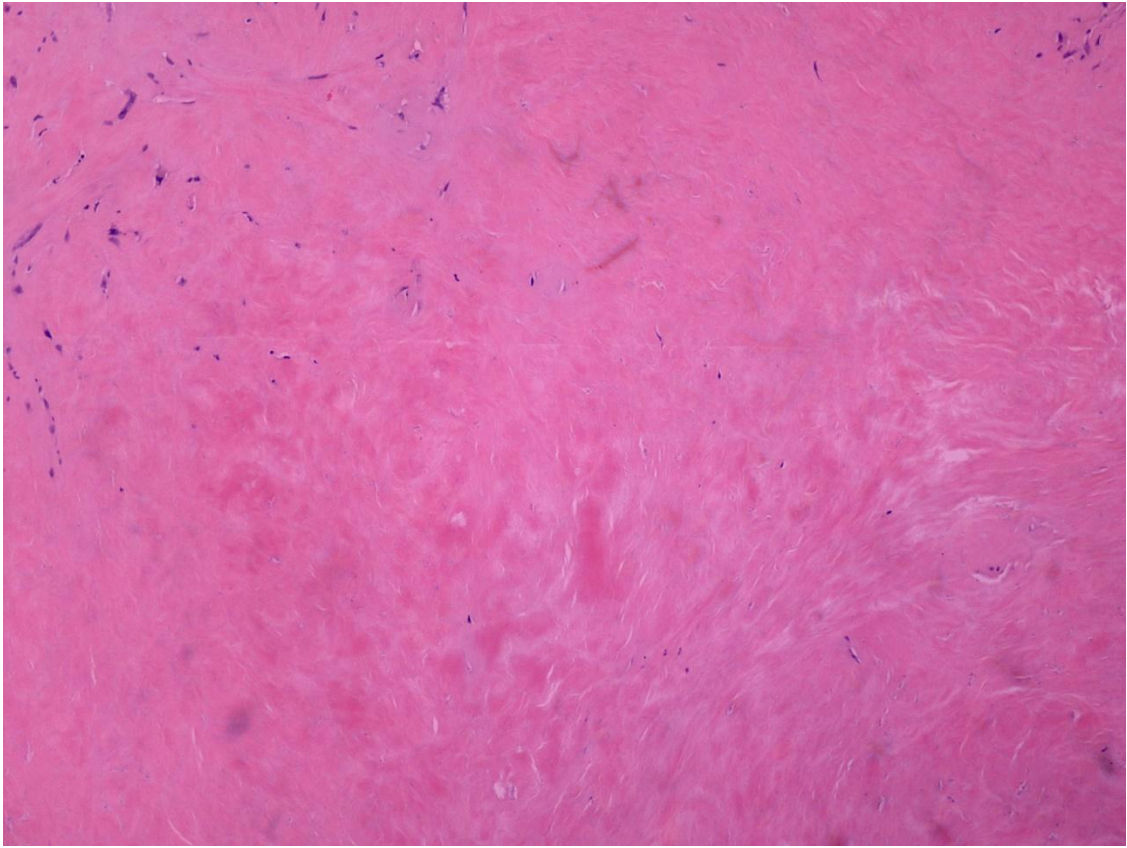


Figure 20 Necrosis – Absence of viable cells or vascular network.

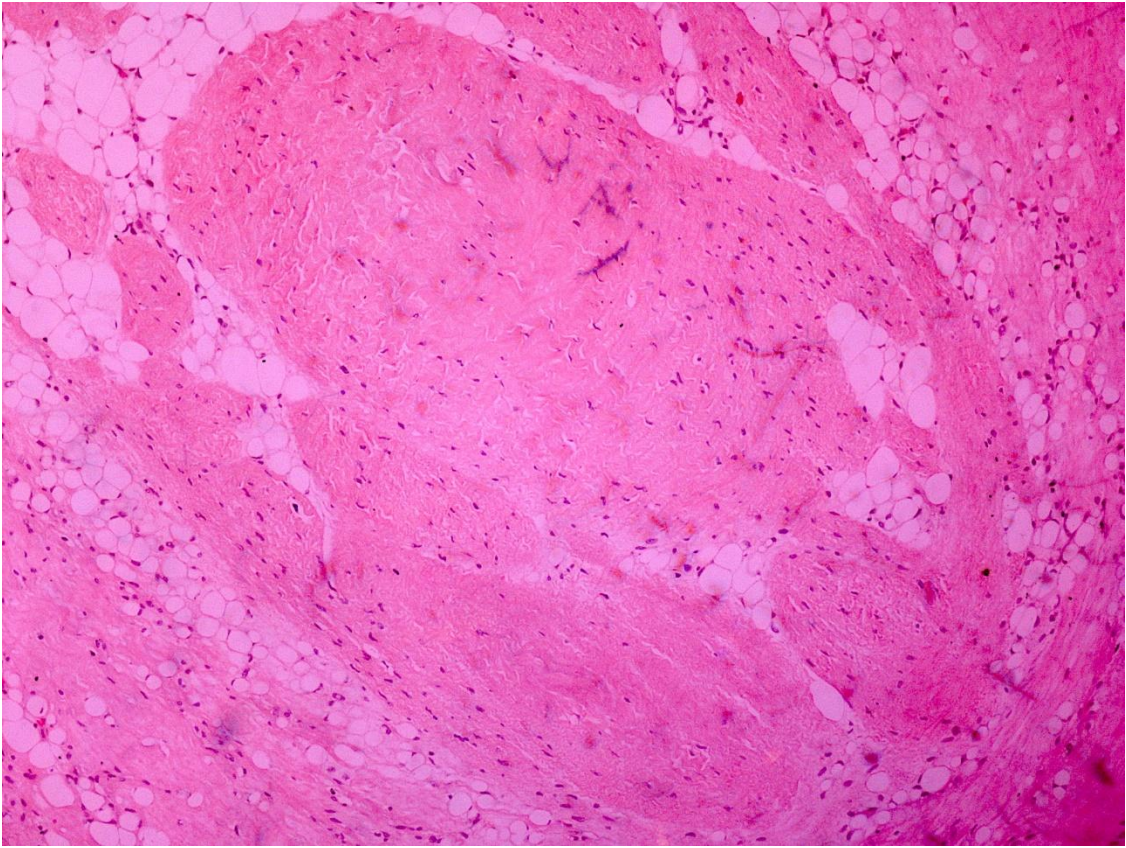


Figure 21 Fibrotic tissue among well differentiated adipocytic cells.

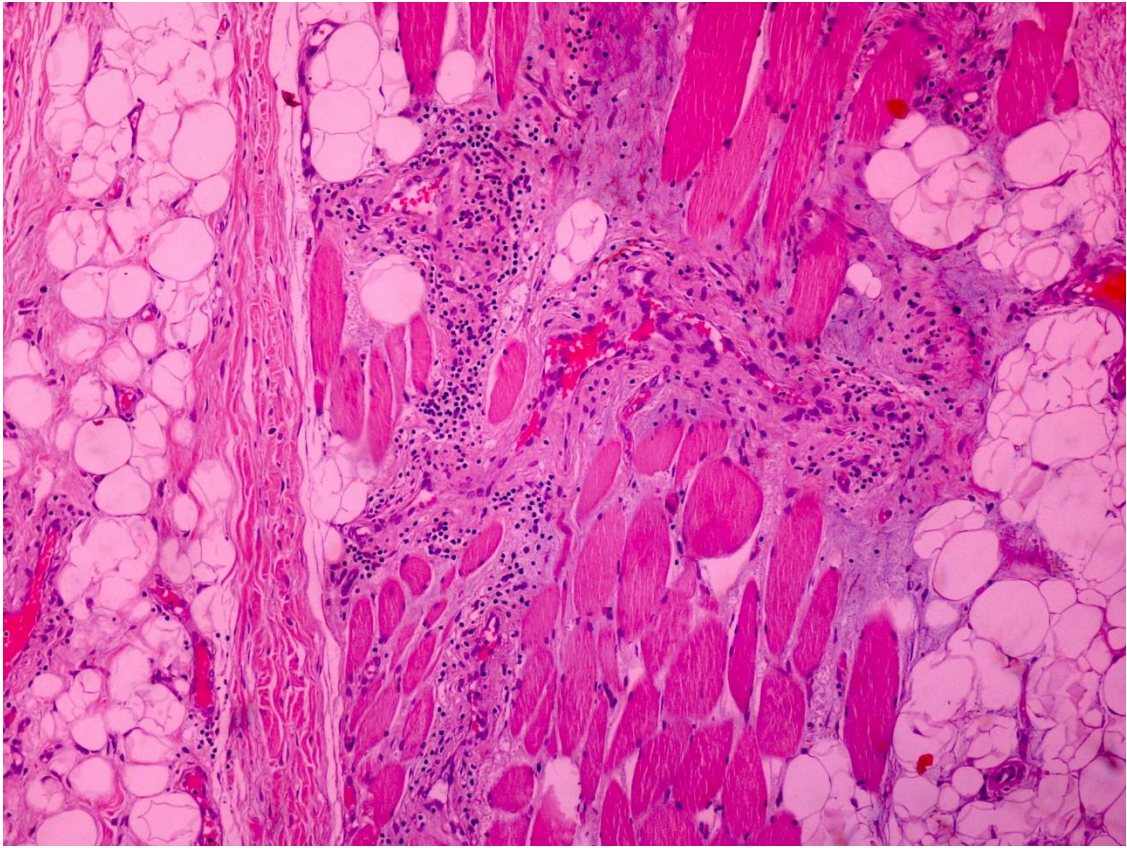


Figure 22 Tissue heterogeneity : vascularized adipocytic part, fibrotic tissue and muscle cells.

Chapter 3 Advanced MRI imaging

MR is the imaging modality of choice for local staging, monitoring response to therapy, and surveillance for recurrence. MR portfolio of biophysical contrasts is broad, exploiting differences among magnetic properties of different tissues and also by deploying a number of different families of pulse sequences. Combination of T1 and T2-weighted sequences are acquired to conclude on the location, extent and depth of the lesion without and with selective fat-saturation to identify adipocytic components. Large size and depth and heterogeneous signal are indications favoring malignancy (Gupta *et al.*, 2016),(Nishida *et al.*, 2007). However, MRI features can be nonspecific and overlap with more common pathologic conditions, making definite diagnosis difficult. To this end, advanced MR techniques complement the MR armamentarium with 4D data for soft tissue tumor classification. In order to elucidate tissue properties it is often necessary to acquire multiple series of images and quantify the progress of a certain parameter in time or the degree of response to an external perturbation. Specifically, Diffusion-weighted imaging (DWI) evaluates random motion of water molecules is sensitive for the detection of cellular dense lesions and has become a mainstay for oncologic imaging. Dynamic contrast-enhanced sequences examine the blood flow or vascular permeability of the tumor vessel network. Lastly, relaxometry techniques can identify tissue magnetic properties which are definite fingerprints of specific molecular characteristics and can be used to derive information on tissue function and composition.

3.1 Diffusion Weighted MRI (DW – MRI)

The target of diffusion weighted imaging is the random (Brownian) motion of water molecules in biological systems. The mathematical framework of this phenomenon was mathematically described by Albert Einstein in 1905, where the average distance travelled by particles over time can be estimated by taking into account temperature, medium viscosity and particle size ((*No Title*), no date). Free water molecules migrate faster in the absence of any cellular or subcellular impediments (intracellular organelles, cell membranes, cells densely structured) or in the absence of exchange phenomena with macromolecules and thus restriction of water movement is indicative of the microenvironment of tissue. More specifically, diffusion is sensitive to the time dependence of water proton displacement as a sensitive probe to the tissue molecular structure.

Diffusion of water molecules within human tissue happens in random directions inside cells, in the extracellular space and also in vessels. Motion related to thermal diffusion is incoherent meaning that particles under consideration at a given time will have a distribution of positions as opposed to coherent motion where all particles would have been equally displaced. This phase distribution of spins leads to a drop in the signal amplitude either acquired by spin or echo gradients. MR images can become sensitive to water diffusion with the addition of two identical gradients in the imaging sequence in opposite directions eliminating signal from static tissue and enhancing signal from water protons in a motionally restrictive environment. The degree of sensitivity is user-controlled by the selection of b value. At least two values are acquired at each imaging sequence in order to model DWI signal decay while the maximum number of b values should comply with hardware restrictions and is also limited by prolonged acquisition times.

Sensitivity to free water motion is an indicative measure of microenvironment complexity which in turn is a marker of normality. The first application of DWI was in acute ischemic stroke as immediate changes in the cellular and extracellular space (cell edema) preceding the episode could be visualized as high signal intensity in DW images (Fisher and Sotak, no date). In parallel diffusion imaging found a very large spectrum of applications in oncology as tumor growth this related to dense cell structure and reduced extracellular space.

The simplest fitting model to DWI data is a single exponential assuming that in biological tissues two main compartments can be identified: the intracellular and extracellular water fractions, partitioned by semipermeable membranes. The exchange of water between the two spaces through the membranes is assumed to be restricted during diffusivity time, thus the tissue is composed of two distinct non-exchanging compartments. Moreover, the contribution of macroscopic movement (blood microcirculation in the capillaries) can be neglected as it

accounts for a very small amount of the total signal. The DWI signal of a homogeneous medium, has a dominant mono-exponential decay curve of the form:

$$S(b)/S(0) = e^{-bADC} \text{ (Kwee et al., 2010).}$$

Apparent diffusion coefficient (ADC) represents the mean displacement of water molecules (typically a random walk) in space (Tofts, 2003)

Another important feature of oncogenesis is neovascularity with complex vessel structure of vessels of increased permeability. Consequently the study of perfusion represents an important aspect of tumor characterization and in the frame of an MR oncologic protocol it is important of obtain quantitative perfusion information, ideally at a voxel level considering tumor heterogeneity. Perfusion sensitive dynamic sequences measure signal changes during the passage of an amount of paramagnetic contrast medium, which is considered a minimally invasive procedure and moreover not free from contraindications.

IVIM intra-voxel incoherent motion

The pure mono-exponential model can be considered valid in a pure solution such as water where the only source of motion is thermal diffusion. More complicated models are appropriate to account for a second faster decaying component attributed to faster water motion mimicking diffusion process in tissue, most probably to arbitrary oriented flow in the micro-capillary network and not to thermal effects. For example, signal from the randomly oriented microcapillary network will be similar to fast diffusion of protons in tissue. The sequence has to be appropriately adjusted, by adding additional acquisitions at low b values to sample the signal in regions where the faster decaying component contributes significantly to the total signal.

The suggestion that information on local perfusion can be obtained quantitatively by perfusion imaging made by Le Bihan (Le Bihan, Denis, Eric Breton, 1988) was in itself very exciting as this meant the lack of need for contrast medium administration. It suggests that the signal contribution from other sources of incoherent motion, such as active transports in living tissue, can be decomposed from the total signal. Blood flow is assumed to be the dominant source of incoherent non thermal signal, concluding to two different compartments in tissue, a micro vascular and a non-vascular.

In its initial stage this idea was not adequately supported by the available hardware of the late 1980s and image quality in terms of signal to noise ratio was poor. However, the rapid and enormous progress on hardware and software prerequisites, i.e. pulse design, fast stable and rapidly alternating gradient systems, the idea of perfusion information based on diffusion

sensitized images emerged. Le Bihan et. al. proposed that micro-perfusion in the capillary network contributes to the DWI signal decay as a random walk (pseudo-random) because of the arbitrary organization of the capillary network (Le Bihan, Denis, Eric Breton, 1988). Thus, perfusion information can be obtained by the intra-voxel incoherent motion (IVIM) model as:

$$S(b)/S(0) = (1 - f)e^{-bD} + fe^{-bD^*} \quad (1)$$

where, $S(b)$ is the measured signal intensity at the current b -value and $S(0)$ is the measured signal intensity with $b=0$, meaning no diffusion weighting, D is the diffusion coefficient, D^* is the pseudo-diffusion coefficient which is considered as an order of magnitude greater than D and f is the micro-perfusion fraction that reflects the ratio of water flowing in capillaries to the total water contained in a voxel. IVIM is an extended form of the conventional mono-exponential model, which equates to the mono-exponential form in the absence of micro-perfusion fraction f . The effect of microcirculation of blood and thus the contribution of the faster decaying component depends on the organ or pathological characteristics of the tumor.

It is important to note that D is not equal to ADC and can be conceived as the perfusion-free ADC. D^* holds information on blood speed and is the measured diffusion coefficient of the microvascular compartment, also including thermal motion of the blood constituents. The parameter f can be related to the incoherently flowing blood volume and fD^* can be understood as a measure of blood flowing through tissue at a unit time (Federau *et al.*, 2014).

In order to capture diffusion contrast in the body including both thermal diffusion and bulk physiologic motion (of the order of 1 mm/s) under the same diffusion sensitization gradients it is essential to discard phase information from the raw images as phase differences caused by the latter are vastly larger than the ones created by the small (order of some microns) thermal displacements of protons. Consequently, only magnitude images are used, with an inevitable cost on image signal to noise ratio.

The lack of need for contrast agent injection and estimation of perfusion parameters with two diffusion gradients has rendered the use of DWI for vascularity assessment very attractive.

Parameter f has been found to have good positive correlation with histological microvascular density in a number of animal and human studies, and also with physiologically or pharmaceutically induce perfusion state changes, listed in the review article of Federau (Federau *et al.*, 2014).

Another active field of research has been the correlation of f with standard perfusion parameters, using the assumptions of a random capillary network and a sufficiently long diffusion time. Studies have investigated correlation of f with DSC derived blood volume in

healthy brain tissue or brain gliomas while less conclusive results have been found between f and DCE of ASL derived perfusion parameters.

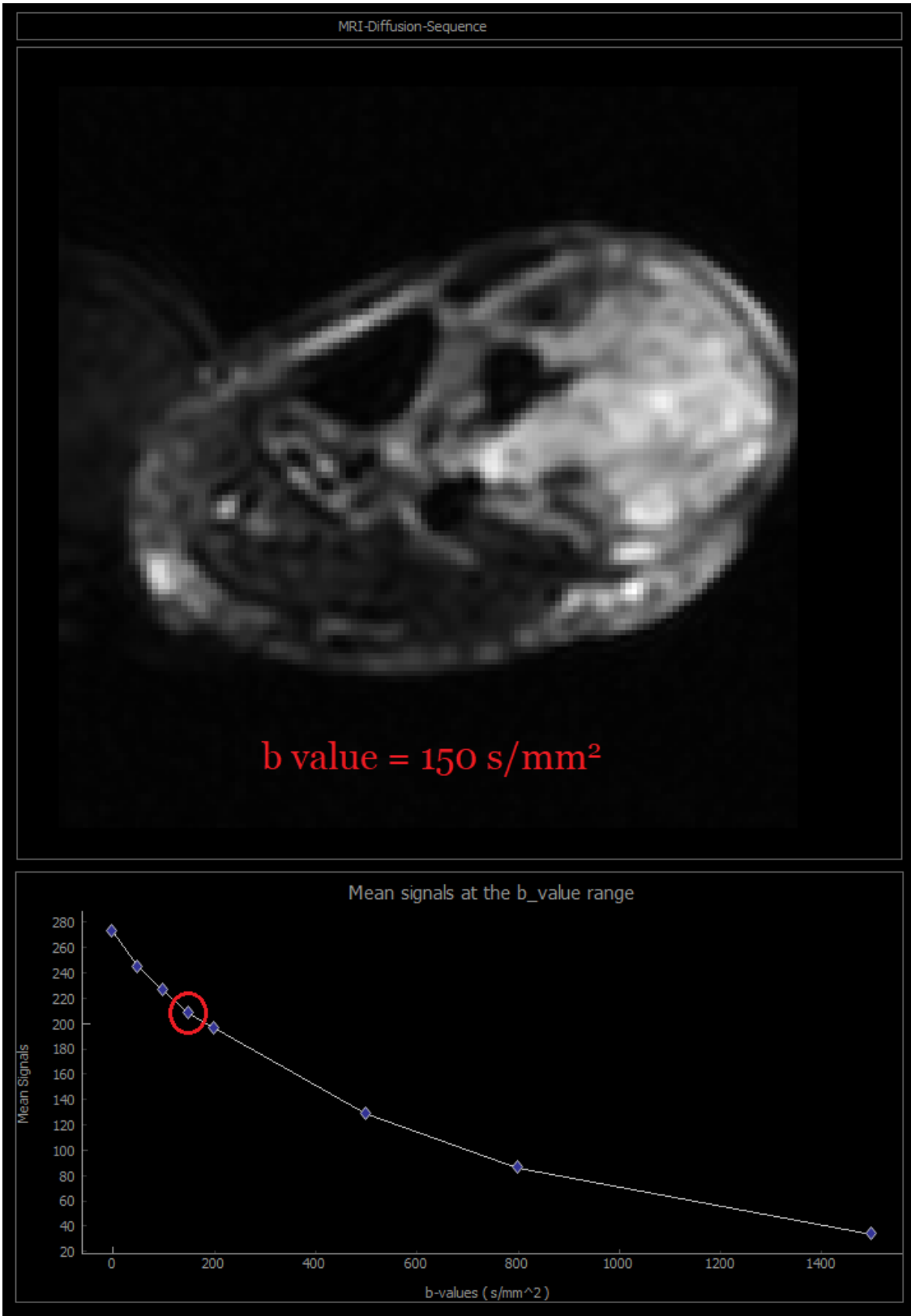


Figure 23 Image from the in house built software platform depicting a sarcoma of the lower limb at b of 150 s/mm^2 (above) and DWI signal decay curve for all b values measured at a 2D ROI

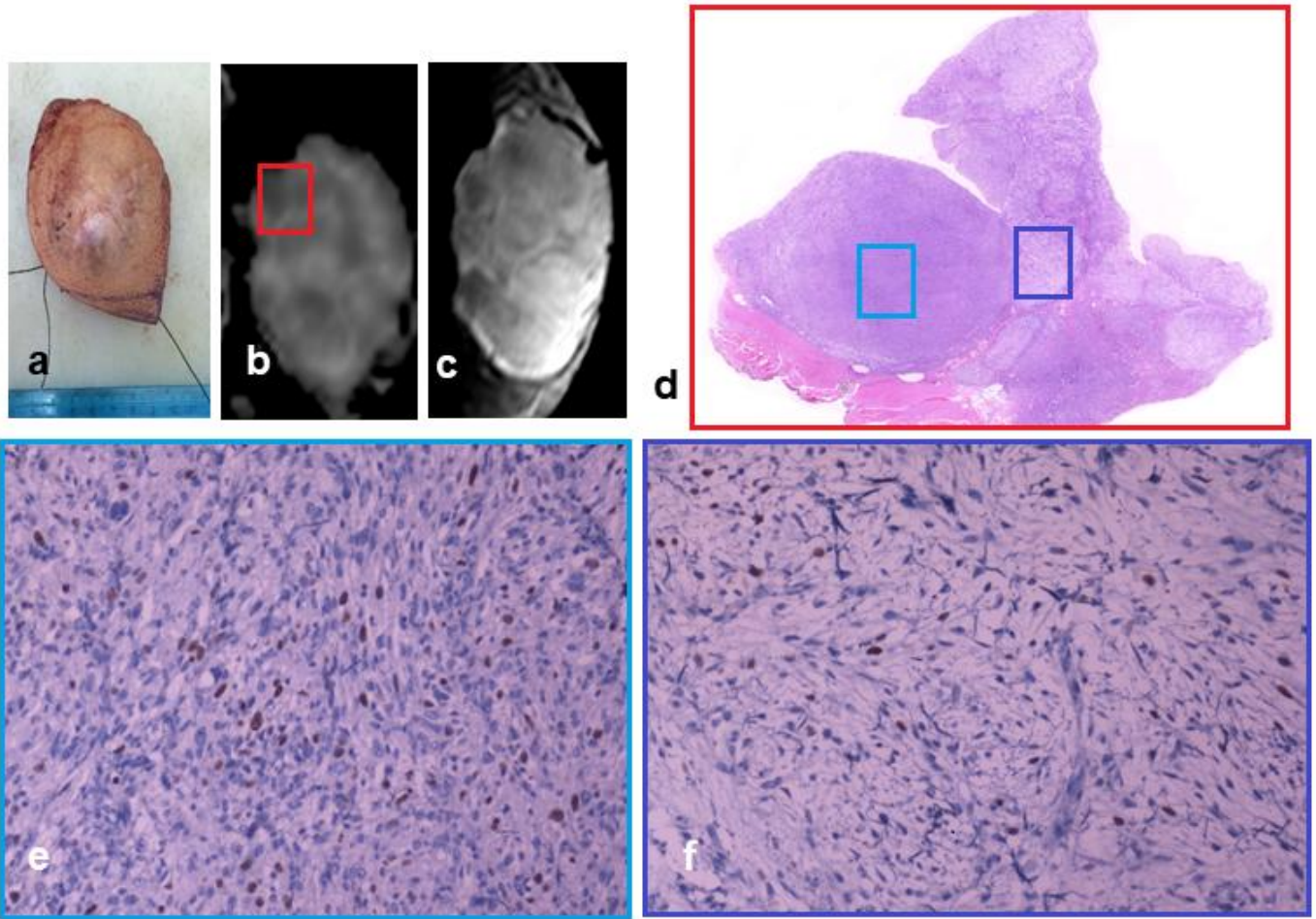


Figure 24 a. Surgical specimen, b. DWI, c. anatomical T2 imaged. d. photo of gross anatomical area of the specimen, e. Ki67 photo of hypercellular area, f. hypocellular area of the tumor

3.2 Dynamic Contrast Enhanced MRI (DCE-MRI)

Tumor angiogenesis is closely related to blood perfusion. While there is a number of different imaging modalities such as PET US or CT to estimate perfusion, MRI has the advantage of combining perfusion information with tumor morphology and the relationship to neighboring structures at high spatial resolution.

Dynamic contrast enhanced magnetic resonance imaging (DCE-MRI) is one of the most commonly used imaging techniques for capturing the perfusion characteristics of biological tissues. It comprises of dynamic sequential T1 acquisitions of low temporal resolution before, during and after the passage of a paramagnetic contrast agent of low molecular weight, which is able to diffuse out of neoplastic vessels. Tumor vascular network is composed of irregular, leaky vessels in a disordered structure. Thus, DCE-MRI acquisition quantifies metrics related to vascular permeability, tissue perfusion, and expansions of extravascular-extracellular spaces (EES) on a voxel basis. This process requires the use of appropriate mathematical models under certain assumptions in order to be fitted to the DCE signal intensity time curves to extract perfusion relevant biomarkers.

DCE-MRI analysis

In some studies, there is a direct processing of signal intensities (SIs) but this can lead to erroneous results due to non-linear relationship of SIs with concentration at high concentrations, dependent on factors such as native T1 of the examined tissue, and MR acquisition parameters. The conversion of the MR signal to concentration of the contrast agent (CA) in the tissues $C_t(t)$ was performed utilizing the flip angle method (Taheri *et al.*, 2011). For the quantification of the DCE-MRI signal, two pharmacokinetic models from the bibliography were selected. The first is the widely known Extended Tofts model (ETM) (Tofts, 1997), a single compartment model where the plasma space is ignored and the CA is moving to the parenchyma with a rate proportional to the difference of the concentrations between plasma and EES with three parameters (K_{trans} , K_{ep} , v_p) as shown in equation (2).

$$C_t(t) = K_{trans}e^{-K_{ep}t} \otimes C_a(t) + v_p C_a(t) \quad (2)$$

The symbol \otimes represents the convolution operator, $K^{Trans} \text{ min}^{-1}$ is the transfer constant from the blood plasma into the EES and $K_{ep} \text{ min}^{-1}$ is the transfer constant from the EES back to the blood plasma while v_p stands for the plasma volume and $C_a(t)$ for the time concentration curve of a feeding artery, also known as the arterial input function (AIF).

The second model used in our analysis is the Gamma capillary transit time model (GCTT) (Schabel, 2012) described by equation (3).

$$C_t(t) = F \left[\gamma\left(\frac{1}{a^{-1}}, \frac{t}{\tau}\right) + \frac{E e^{-K_{ep}t}}{(1 - K_{ep}\tau)^{1/a^{-1}}} \left[1 - \gamma\left(\frac{1}{a^{-1}}, \left(\frac{1}{\tau} - K_{ep}\right)t\right) \right] \right] \otimes C_a \quad (3)$$

The recently suggested GCTT model, unifies four well-known models such as the Tofts Model (Tofts, 1997), the ETM, the adiabatic tissue homogeneity (ATH) model (St Lawrence and Lee, no date) and the two compartment exchange (2CX) model (Brix *et al.*, 2012) depending on the value of a^{-1} being the shape parameter of the Gamma distribution of the capillary transit times. $F \text{ mL/mL/min}^{-1}$ is the blood flow or blood perfusion, $a^{-1} = t_c/\tau$ is the width of the distribution of the capillary transit times inside a voxel, $\gamma(a, z)$ is the Gamma function, E is the extraction fraction of CA that is extracted into the EES during a single capillary transit. The K_{trans} and v_p parameters are not calculated directly from the fitting process as in ETM. Therefore, these parameters are determined using the relations: $K_{trans} = FE$, $v_p = (1 - Hct) * Ft_c$ (Schabel, 2012). For our analysis hematocrit (Hct) value were considered 0.45 for male and 0.42 for female patients.

Importantly, since both DWI and DCE techniques examined tumor aggressiveness from different observation angles it would be very useful to conclude on a common location highly suspicious of locally increased malignancy pre-operatively. This non-invasive technique can be a very powerful tool for biopsy guidance and avoid possible errors of tumor grade misestimation from suboptimal sampling.

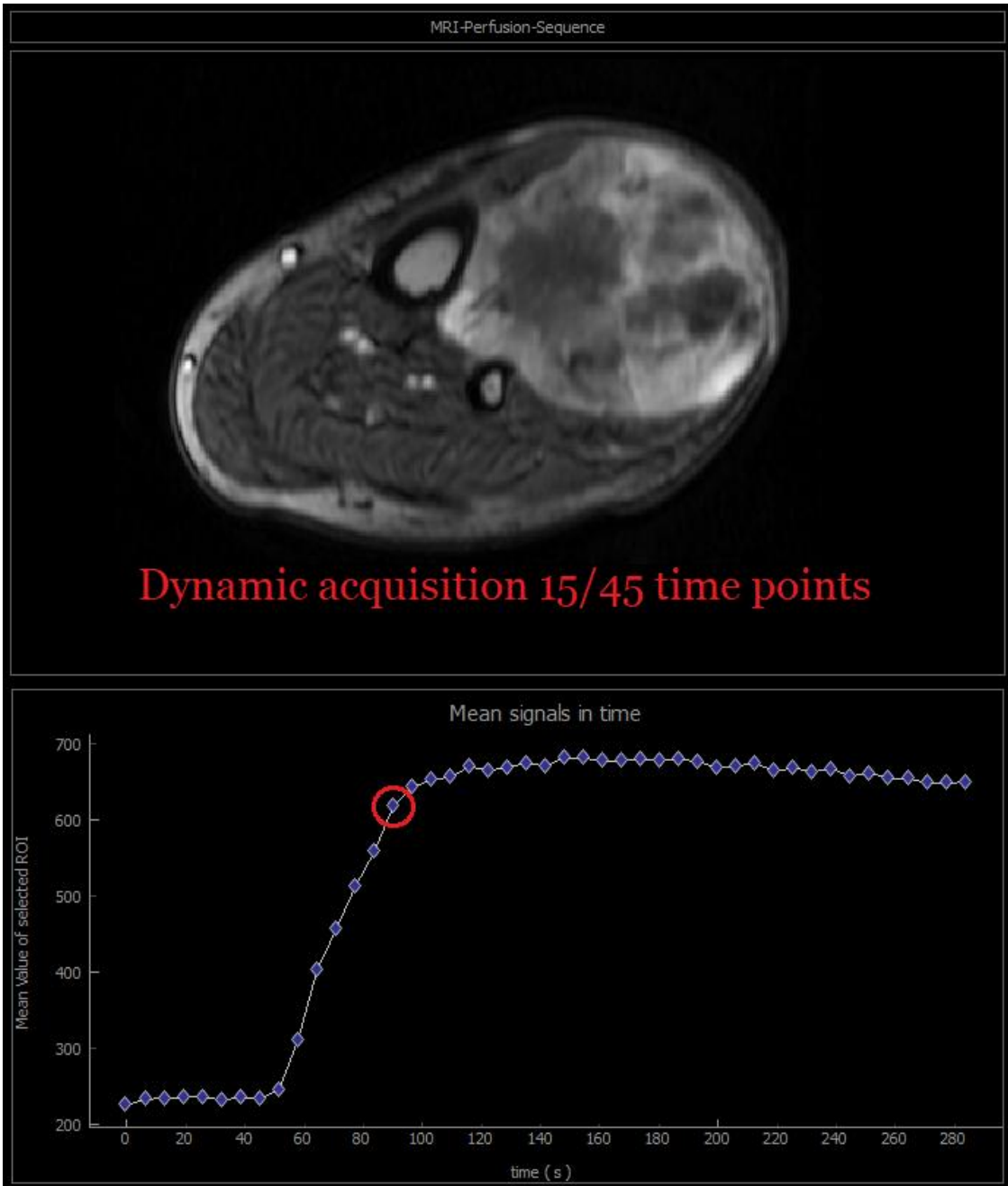


Figure 25 Snapshot of the dynamic phase of DCE acquisition for a lower limb sarcoma and the corresponding enhancement curve for the whole DCE series.

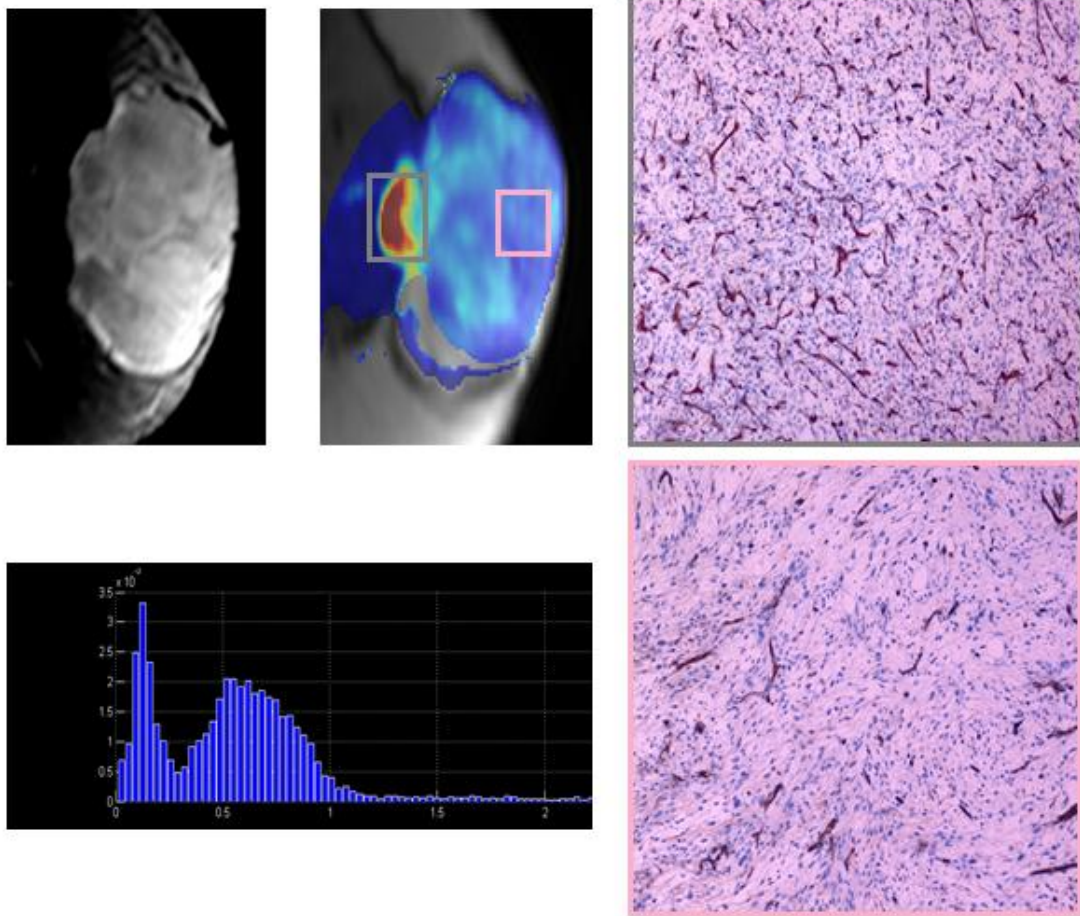


Figure 26 Evaluation of tumor vascularity with DCE MRI (Ktrans parametric map in the top middle and Ktrans histogram in the bottom left) and histopathologic images (CD 34 stain) of highly vascularized (top right) and poorly vascularized tissue (bottom right)

3.3 T2/ T2* relaxometry

T2 relaxometry has been a robust and sensitive method for tissue or material characterization based on MRI data, as T2 relaxation constant can be considered as a definite signature of the inner structure of the imaging object. T2 constant does not depend on the reader, pulse sequence parameters or magnetic field strength but rather on the local chemical and physical environment. It is thus sensitive to microstructure and composition of the sample and can quantitatively characterize material or tissue. It has been used from the early days of MRI not only in the medical field but also in other scientific domains such as food science, geological studies, radiation dosimetry etc. (Santos et al., 2017),(Loskutov and Zhakov, 2016),(Maris et al., 2016). In particular, T2 relaxation time of tissue is affected by water content, random movement of water molecules and macromolecules, local tissue temperature, tissue fat content, presence of paramagnetic particles and pH value (Chaland et al., 2019).

T2 relaxation rate measurement was firstly proposed by Hahn in 1952 (Hahn and Maxwell, 1952) with repetitive spin echo sequences but the method was later optimized by the CPMG sequence (Fransson et al., 1993a) which addresses the problem of imperfections in the refocusing RF pulses inducing errors to the measurement process. T2 relaxometry uses fitting models to the echo train data to obtain information on the number of decaying components and their relaxation rates. The simplest model assuming one component present in tissue is adequately fitted with one exponential term. However, tissues are heterogeneous in nature and thus one imaging voxel contains an ensemble of different cells and extracellular matrix components. In order to infer information on the content and interactions among these microscopic components at a sub-imaging level it is necessary to deploy more complex methods with more than one exponential terms for fitting of the signal decay curve over time.

Fat and water imaging

For some disease states or pathological situations it is very useful to decompose and quantify the amount of signal corresponding to fat or water. Such cases are fatty infiltration of the liver, acute phase of multiple sclerotic plaque formation, layered structure in the cartilage, bone marrow composition with age or after transplantation or irradiation and also for the distinction between various kinds of tumors on the basis of lipid content.

For tissues of interest to this study that contain fat to a greater or lesser extent it is important to describe certain particular characteristics of fat and water imaging. Routinely measured MR images, as opposed to spectroscopic sequences, measure signal reflecting the sum of signals from all mobile protons within a certain tissue volume. Water protons have a single resonance frequency and restore transverse relaxation at a slow rate (large T2 values) which can be adequately approximated with a single exponential term. However, water has a faster relaxation rate when bound to macromolecules or when spatially restricted by tissue structure. Lipid protons in fat cells (adipocytes) consist mainly of triacylglycerols and are in a liquid state in body temperature.

Lipid protons, as opposed to water protons, as parts of a macromolecule with magnetic field inhomogeneity at very local level, exhibit more complex relaxation patterns. In order to infer information on tissue composition and the relative fraction of different distinct components the plot of component weightings as a function of T2 values is measured (T2 distribution). This serves to identify its compartmental origin and the corresponding amplitude as a measure of the anatomical size of the compartment. The equation used for fitting the T2 decay curve is

$$S(T E_k) = \sum_{i=1}^N A_i \exp\left(-\frac{T E_k}{T_{2i}}\right), \quad N = 1,2$$

Where N is the number of components. Bi-exponential description adequately approximates the transverse relaxation decay curves, resulting in three independent variables which can be used for descriptive tissue characterization.

Typically only magnitude images are used for T2 relaxometry in order to avoid sensitivity to a large number of experimental factors, such as scanner type, field homogeneity, temperature, coil type and pulse sequence design inherent in the phase part of the complex signal. However reduced sensitivity to image artifacts comes at a penalty to SNR levels which is also a common obstacle for robust MR signal quantification.

The most widely used method for obtaining T2 distributions is fitting the magnitude MR images acquired by a multi-echo MRI pulse sequence using an Inverse Laplace Transform (ILT) algorithm. When ILT methods are used for magnitude only MR relaxometry data it is important to account for the Rician nature of the MR signal distribution, meaning that a correction process has to be followed for non-Gaussian distribution. In the alternative case of using the complex MR signal for increased SNR levels phase unwrapping methods have to be deployed in order to avoid miscalculations due to other factors affecting phase, such as local field inhomogeneities. However, direct fitting of mono or multi-exponential functions to an adequate number of sampling points during the signal decay evolution can reveal the distinct

decay patterns present in the measured signal. Based on that, an assumption can be made on the number of decaying components within the tissue. The advantage of the latter method over ILT is the possibility to obtain voxel wise information on the tissue content. However, this method usually requires a priori knowledge on the number of different relaxation patterns and moreover the solution becomes a non-trivial mathematical problem for a number of components greater than 2.

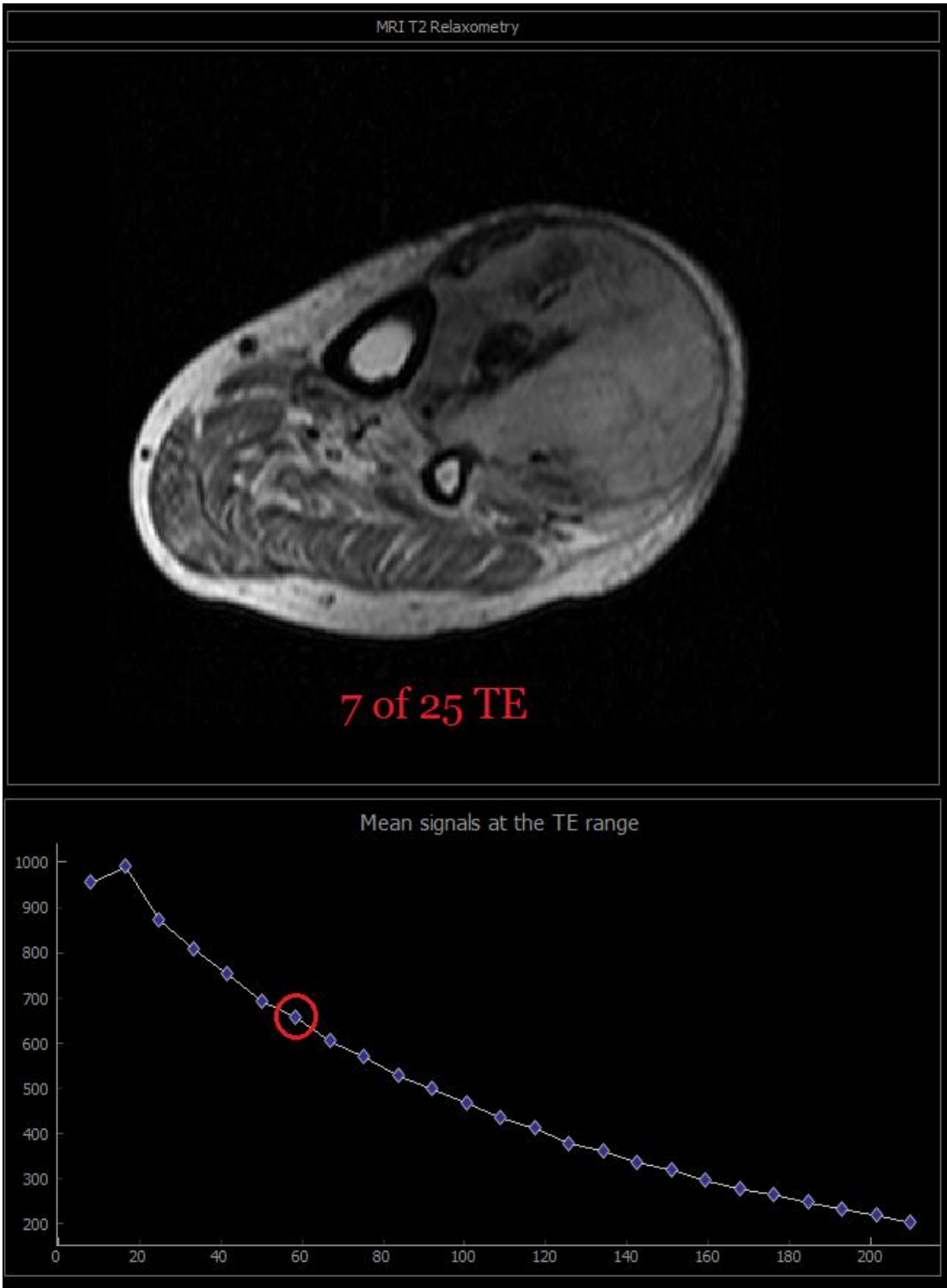


Figure 27 Snapshot from in house built T2 relaxometry software visualizing a lower limb sarcoma at the 7th echo.

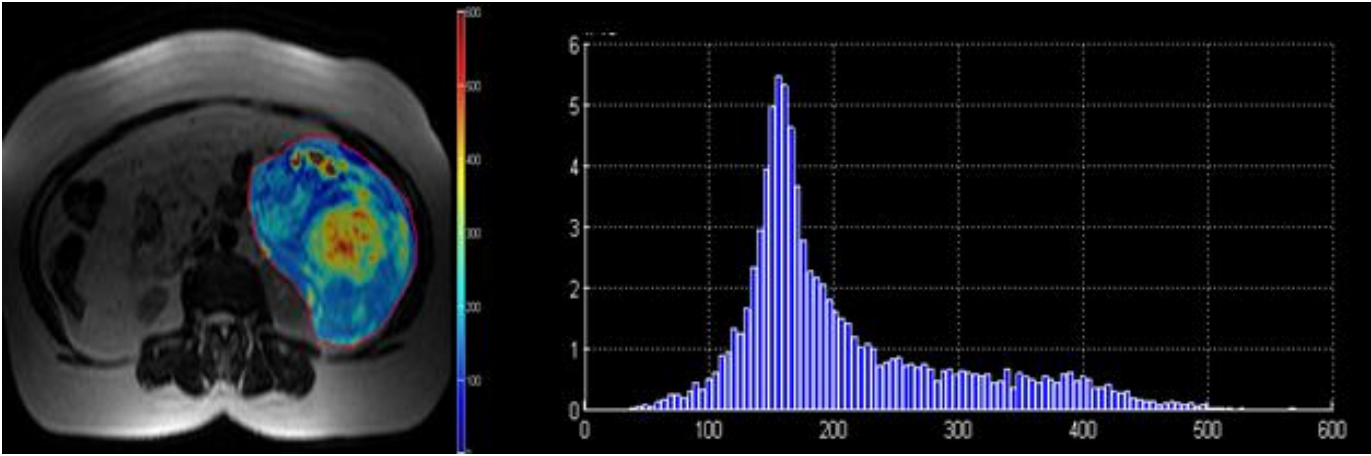


Figure 28 T2 parametric map on a patient with dedifferentiated liposarcoma of the abdomen (left) and corresponding T2 spectrum of the lesion (right).

Scope of the study

The overall aim of this work was to deploy an extended MR protocol for the study of soft tissue sarcomas and extract clinically relevant information based on quantitative markers for the support of diagnosis by maximizing the amount of information that can be derived by an advanced extended MR examination. Each sequence was designed to serve a specific clinical question and the final result is a set of imaging biomarkers that are indicative of the tumor subtype, when used along with conventional diagnostic techniques.

The specific sub-tasks delivered within the frame of this study can be summarized hereupon:

To examine the possible correlation of DWI and DCE imaging markers, indicative of cellularity and vascularity respectively, derived from well-established mathematical models (IVIM for DWI while ETM and GCTT for DCE as described in the following sections) on patients with soft tissue sarcomas. As both vascularity and cellularity are measures of tumor aggressiveness, we study the spatial correlation of relevant imaging markers in order to have a visual representation of the most malignant parts. The impact of spatial correlation of DWI and DCE metrics of malignancy is the mitigation of possible sampling errors from pre-operative biopsy, which might underestimate the tumor grade or even give a false negative result. This point is thoroughly discussed in chapter 4.

Considering that fat detection is essential for the diagnosis of liposarcoma, we examined an imaging phenomenon tightly linked to the properties of fat, selectively. Subcutaneous fat may have variable signal intensity on T2w images depending on the choice of imaging parameters and more specifically, in the time interval between consecutive refocusing RF pulses (ESP, Echo SPacing) in fast spin echo imaging. We examined the use of T2, T2* relaxometry and spin coupling related signal changes (Spin Coupling ratio, SCr) on two different imaging protocols as clinically relevant markers of fat cell differentiation. Based on previous work that confirmed that the amount of signal loss due to spin coupling is significant for ESP below 20 ms on fat phantoms, we extend this research to the clinical field. The role of spin coupling and T2/T2*

relaxometry was studied for the support of pathognomonic evidence for the characterization of fat containing soft tissue masses. These issues are discussed in detail in chapter 5.

Another specific goal of this work was to examine an alternative method to ILT for the analysis of T2 relaxometry data for the calculation of T2 spectrum regarding fat containing samples. The purpose of examining an alternative method is to gain the advantage of voxelwise parametric maps that are impossible when using ILT but are essential for imaging heterogeneous masses in clinical practice. After establishing the validity of the method, we deployed it for the voxel wise characterization of the relaxation pattern of benign and malignant fat containing tumors of variable degree of malignancy. The proposed method requires no a priori assumption on the number of components (maximum two) and is thoroughly discussed in chapter 6.

Lastly, chapter 7 briefly repeats the main points ensued by the relevant subparts of the study dedicated to the analysis of specific sequences as an overall conclusion.

Chapter 4 Statistical and spatial correlation between diffusion and perfusion MR imaging parameters on soft tissue sarcomas

4. 1 Motivation

The purpose of this part of study was to examine the correlation of diffusion and perfusion quantitative MR parameters, on patients with malignant soft tissue tumors. Moreover, in the frame of DWI-DCE correlation study, we investigated the spatial agreement of hallmarks of malignancy as indicated by diffusion and perfusion biomarkers respectively.

The importance of this work relies on the ability to obtain perfusion information from a non-invasive MRI method, considering that contrast medium administration is considered as a minimally invasive procedure and there are cases where its use is contraindicated. The possible correlation of DCE and DWI results will simplify the acquisition process without compromising the diagnostic information that can be derived from an MRI examination with an advanced oncologic protocol.

For the second part of this work, we made a visual representation of the tumor areas that present more aggressive imaging feature in either DWI or DCE with thresholding above the mean value. Then we fused the two maps onto the anatomical image in order to identify the areas that are more suitable for tissue harvesting during pre-operative biopsy.

4. 2 Method

30 patients (18 males, 12 females median age: 63 y) were recruited for the MRI examination with suspicion for soft tissue tumor, during a 2 year study period (2016-2018). Lesions showing no enhancement or tumors with very low signal in fat suppressed sequences, such as benign lipomas or well differentiated liposarcomas were excluded. Similarly to common practice, cases where MRI examination is contraindicated (pacemakers, ferromagnetic implants, claustrophobia, contraindications for administration of Gadolinium contrast medium) were also excluded. Moreover, severe image degradation from artifacts especially for abdominal STT also led to the exclusion of 3 patients. The examination protocol has been approved by the local ethics committee and all patients have signed an informed consent for the use of their data for research purposes. The final patient cohort of the analysis comprised the following STT: 6 dedifferentiated liposarcoma, 5 pleomorphic liposarcoma, 4 myxoid liposarcoma, 4 leiomyosarcoma, 2 alveolar sarcoma, 3 malignant peripheral nerve sheath sarcoma, 1 Ewing sarcoma. The diagnostic procedure also included biopsy, either with CT or US guidance proceeding the MR examination. Patients with malignant findings in biopsy were subltitted to the surgical excision of the tumor. As a final step, the surgical specimen was immediately transferred to histopathologic department for analysis. A graphical representation of the described workflow is shown in Fig. 20

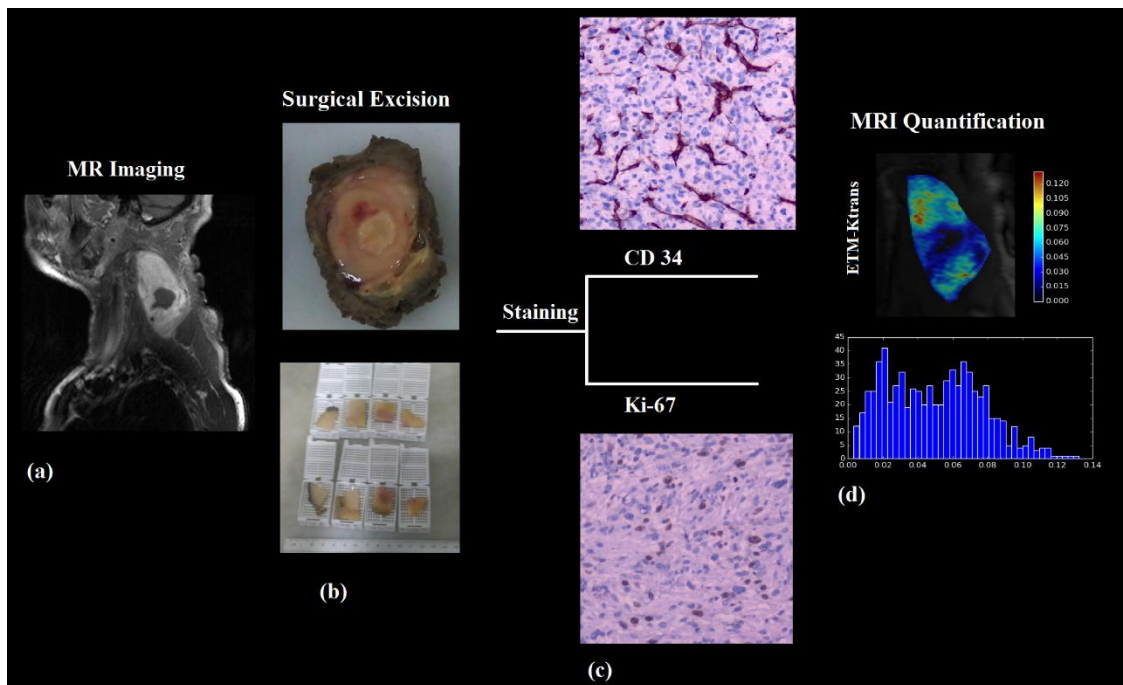


Figure 29 Workflow description. (a) MR imaging (fat suppressed contrast enhanced T1W) of a soft tissue mass in the neck. (b) Surgically excised specimen and tissue preparation sampling for staining. (c) Assessment of vascularity (CD

34) and mitotic activity (Ki-67) based on specific staining. (d) Quantitative analysis of MR data, indicative Ktrans parametric map and the corresponding histogram.

MRI Protocol

The imaging protocol, apart from the conventional sequences, included DWI and DCE-MRI quantitative techniques. Depending on the lesion site the appropriate choice of coil and FOV was made on the basis of complete lesion coverage at highest SNR. DW axial images were acquired utilizing an EPI (Echo Planar Imaging) sequence with fat suppression, diffusion sensitizing gradients in 3 directions ($b = 0, 50, 100, 150, 200, 500, 800, 1500 \text{ s/mm}^2$), number of slices = 14-18, echo time (TE) =100 ms, repetition time (TR) = 3500 ms, matrix size =128×128, field of view either (FOV)=200×200mm (alternative for torso 400x400mm), slice thickness=5mm. This technique has been applied for the reduction of machine related geometrical distortions or apparent distortions in signal intensities. T1W DCE perfusion MR imaging was performed by utilizing a 3D VIBE (volume interpolated breath hold examination) sequence in the axial plane with variable flip angles (FA=5o, 10o, 15o, 20o, 25o, 30o) for the initial calculation of the parametric T1 maps. Consequently, an intravenous bolus injection of the paramagnetic CA (Magnevist, Gadopentetate Dimeglumine, Bayer Healthcare, Bayer, 0.1 mmol/kg) was performed. The aforementioned T1W DCE VIBE perfusion sequence comprised 45 dynamic acquisitions (6.5 s temporal resolution) after the intravenous injection of the CA with the following imaging parameters: number of slices=14, FA=15o, TE=3.23 ms, TR=7.1 ms, matrix size=384x384, FOV=200×200mm (400x400 mm) and slice thickness=5 mm.

Histopathologic analysis

Within a period of 14 days after MR examination, all patients with relevant indications from biopsy underwent surgery during which the surgeon marked the specimen with sutures in predefined points in order to enable the actual three-dimensional orientation of the specimen in relation with the patient's body. The excised specimens were transferred to the department of pathology for classification and grading. The outer surface of the specimen was marked with permanent ink in order to identify the surgical markings. The pathologist confirmed the original orientation of the specimen in the body based on the sutures and then cut consecutive thin slices from the top and the bottom of the specimen in order to identify the upper and lower rim of the neoplasm. The central slice of the tumor, corresponding to the lesion's central imaging slice, was selected after measuring the distances from the upper and lower margins,

was divided in orthogonal slabs (in a grid-manner), and placed into plastic cassettes (Fig. 19(b)). Tumor tissue sections were processed according to CAP guidelines (Lester, 2010) and recommendations for specimen handling 4 μm thick sections of each tumor slab were cut, placed into glass slides, stained and examined microscopically (Nikon Eclipse E-200) in order to characterize each area of the central tumor slice in terms of differentiation, cell type, cellular atypia, cellularity, mitotic activity, vascularity and presence of necrosis. More specifically, Ki-67 staining, indicative of mitotic activity was used to give insight into the presence of areas of high or low cellularity which is also the contrast mechanism of DWI. Analogously, CD 34 staining, indicative of vascular density was performed to locate highly perfused areas of the tumor to be studied alongside with DCE imaging Fig. 19(c). Histopathologic analysis results were used to verify findings from MRI data post processing analysis, graphically represented as voxel-based parametric maps and ROI histograms in order to have a visual overview of the distribution of the calculated values for each marker Fig. 19(d).

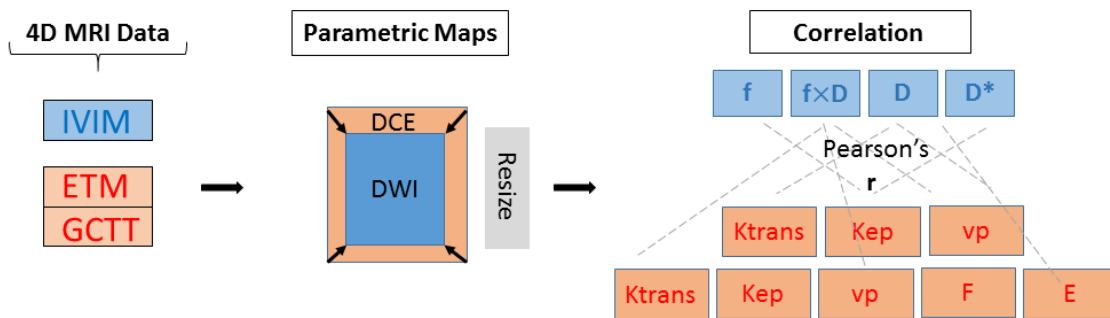


Figure 30 Image post processing workflow (data acquisition, generation of parametric maps and resizing, Pearson's correlation between derived markers).

Mathematical framework for IVIM-MRI analysis

The quantification of diffusion and perfusion parameters was implemented in python 3.5 (www.python.org). The parametric maps were extracted with the trust region reflective algorithm, of the SciPy library (scipy.optimize.least_squares).

The DWI signal of a homogeneous medium, has a dominant mono-exponential decay curve of the form: $S(b)/S(0) = e^{-bADC}$ (Kwee *et al.*, 2010). Apparent diffusion coefficient (ADC) represents the mean displacement of water molecules (typically a random walk) in space (Tofts, 2003). Le Bihan *et al.* proposed that micro-perfusion in the capillary network contributes to the DWI signal decay as a random walk (pseudo-random) because of the arbitrary organization of the capillary network (Le Bihan, Denis, Eric Breton, 1988). Thus, perfusion information can be obtained by the intra-voxel incoherent motion (IVIM) model as:

$$S(b)/S(0) = (1 - f)e^{-bD} + fe^{-bD^*} \quad (1)$$

where, $S(b)$ is the measured signal intensity at the current b -value and $S(0)$ is the measured signal intensity with $b=0$, meaning no diffusion weighting, D is the diffusion coefficient, D^* is the pseudo-diffusion coefficient which is considered as an order of magnitude greater than D and f is the micro-perfusion fraction that reflects the ratio of water flowing in capillaries to the total water contained in a voxel.

The IVIM parameters were obtained by using the aforementioned nonlinear fitting algorithm with the following constraints for each parameter: $f \in [0,1]$, $D \in [0,5] \times 10^{-3} \text{ mm}^2/\text{s}$, $D^* \in [10,200] \times 10^{-3} \text{ mm}^2/\text{s}$.

DCE-MRI analysis

The conversion of the MR signal to concentration of the contrast agent (CA) in the tissues $C_t(t)$ was performed utilizing the flip angle method (Taheri *et al.*, 2011). For the quantification of the DCE-MRI signal, two pharmacokinetic models from the bibliography were selected. The first is the widely known Extended Tofts model (ETM) (Tofts, 1997) with three parameters (K_{trans} , K_{ep} , v_p) as shown in equation (2).

$$C_t(t) = K_{trans}e^{-K_{ep}t} \otimes C_a(t) + v_p C_a(t) \quad (2)$$

The symbol \otimes represents the convolution operator, $K^{Trans} \text{ min}^{-1}$ is the transfer constant from the blood plasma into the EES and $K_{ep} \text{ min}^{-1}$ is the transfer constant from the EES back to the blood plasma while v_p stands for the plasma volume and $C_a(t)$ for the time concentration curve of a feeding artery, also known as the arterial input function (AIF).

The second model used in our analysis is the Gamma capillary transit time model (GCTT) (Schabel, 2012) described by equation (3).

$$C_t(t) = F \left[\gamma\left(\frac{1}{a^{-1}}, \frac{t}{\tau}\right) + \frac{E e^{-K_{ep}t}}{(1 - K_{ep}\tau)^{1/a^{-1}}} \left[1 - \gamma\left(\frac{1}{a^{-1}}, \left(\frac{1}{\tau} - K_{ep}\right)t\right) \right] \right] \otimes C_a(t) \quad (3)$$

The recently suggested GCTT model, unifies four well-known models such as the Tofts Model (Tofts, 1997), the ETM, the adiabatic tissue homogeneity (ATH) model (St Lawrence and Lee, no date) and the two compartment exchange (2CX) model (Brix *et al.*, 2012) depending on the value of a^{-1} being the shape parameter of the Gamma distribution of the capillary transit times. $F \text{ mL/mL/min}^{-1}$ is the blood flow or blood perfusion, $a^{-1} = t_c/\tau$ is the width of the distribution of the capillary transit times inside a voxel, $\gamma(a, z)$ is the Gamma function, E is the

extraction fraction of CA that is extracted into the EES during a single capillary transit. The K_{trans} and v_p parameters are not calculated directly from the fitting process as in ETM. Therefore, these parameters are determined using the relations: $K_{trans} = FE$, $v_p = (1 - Hct) * Ft_c$ (Schabel, 2012). For our analysis hematocrit (Hct) value were considered 0.45 for male and 0.42 for female patients.

To assess the quality of the fits between the data and the pharmacokinetic models (assume $G(x, t)$) the root mean squared error (RMSE) was chosen. Considering, parameters $x = \{x_1, x_2, \dots, x_p\}$ and d data points of size N the RMSE formula is given by equation (4).

$$RMSE = \sqrt{\sum_{i=1}^N \frac{(G(x, t_i) - d_i)^2}{N}} \quad (4)$$

Correlation Analysis

As a first step, perfusion derived maps were resized through cubic interpolation (to mitigate information loss) to match the size of the diffusion parametric maps. Then the slice location of each DICOM tag was used to align the two sequences in the z-axis. Images from each 4D dataset were masked according to the corresponding 3D ROI delineated by an experienced (>30years) musculoskeletal radiologist. To avoid false or biased results of correlation between non perfused areas ($v_p < 0.05$ or $f < 0.05$) were excluded from the analysis. Thus for every 3D ROI Pearson's correlation coefficient was calculated by (5).

$$r_{f,vp} = \frac{\sqrt{\sum_{i=1}^N (f_i - \bar{f})(vp_i - \bar{vp})}}{\sqrt{\sum_{i=1}^N (f_i - \bar{f})^2} \sqrt{\sum_{i=1}^N (vp_i - \bar{vp})^2}} \quad (5)$$

A graphical representation of the post processing process is shown in Fig. 2 describing the steps from data acquisition to the correlation of all possible pairs of IVIM ($f, D, D^*, f \times D, f \times D^*$) and DCE ($K_{trans}, K_{ep}, v_p, E, F$) derived parameters.

Spatial identification of tumor aggressiveness

As both high cellularity and high vascular supply are markers of tumor aggressiveness, we calculated the percentage of tumor voxels meeting both criteria of low D and high K_{trans} . Between the two models used for K_{trans} extraction in this study we proceeded in this step

with the ETM based calculation as it is more widely used and tested for quantitative studies (Litjens *et al.*, 2010). For every 3D whole tumor ROI, the mean value of D and Ktrans were used as thresholds between high and low cellularity and vascularity respectively.

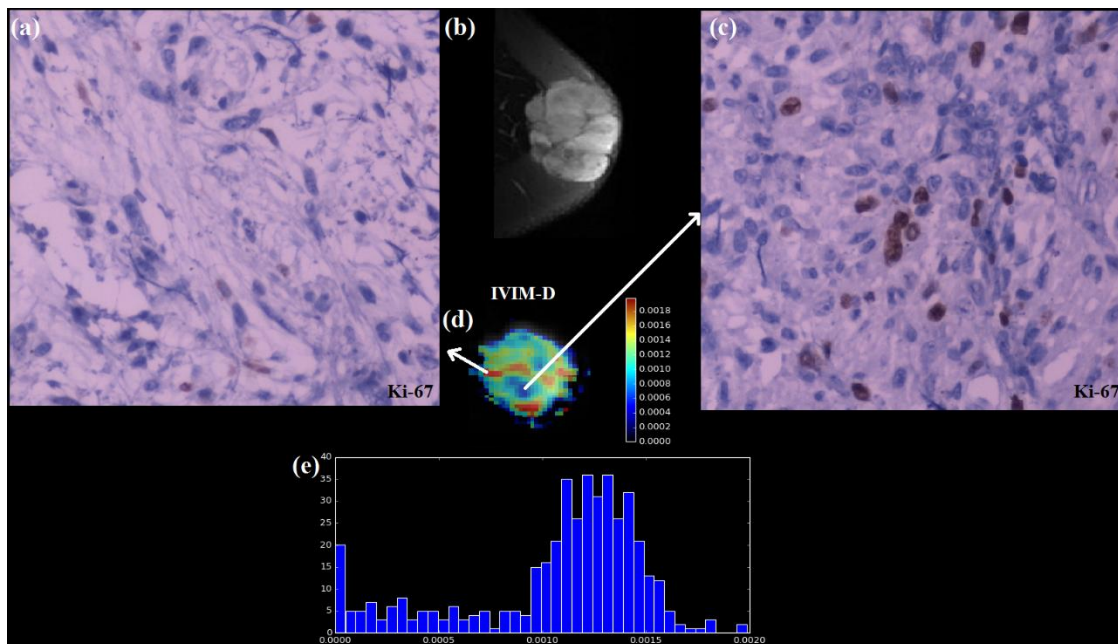


Figure 31 Malignant tumor (MPNST) of the left shoulder (axial STIR MR image (b)). Histopathologic analysis Ki-67(x100) showed alternation of areas with low (a) and high (c) cellularity areas. Corresponding IVIM-D parametric map (d) and corresponding histogram (e).

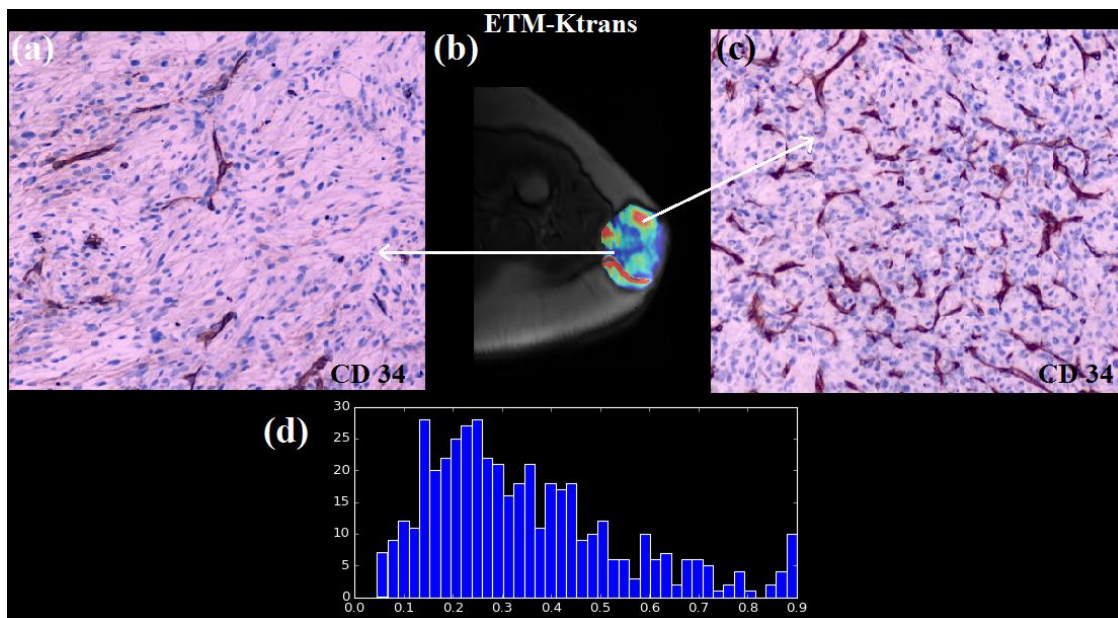


Figure 32 Malignant tumor (MPNST) of the left shoulder. ETM Ktrans map is overlaid to T1 VIBE image for the tumor ROI (b). Histopathologic analysis CD34 (x100) showed diverse pattern of vascularity (i.e. areas of low vascularity (a) neighboring to areas of high vascularity (c) and corresponding Ktrans histogram as calculated by the ETM.

4.3 Results

The best aimed value describing tissue cellularity, is D calculated by the IVIM model deprived of the contribution of macro-diffusion movement (blood flow) from the vascular part of the tissue. Voxel based parametric maps were calculated for all patients and results were studied for reference based on the histopathologic analysis of the central tumor slice and more specifically Ki-67 stain images, showing nuclei density and mitotic activity and thus cellularity (Fig. 20). Similarly, CD 34 stain was used for assessing regional tumor vascularity (Fig.22).

In terms of fitting accuracy, both pharmacokinetic models performed equally well, exhibiting low RMSE values. The mean RMSE and standard deviation values for ETM and GCTT models were $RMSE_{ETM} = 0.0879 \pm 0.1264$ and $RMSE_{GCTT} = 0.1062 \pm 0.1350$ respectively.

The Pearson's correlation r of both vp-ETM and vp-GCTT with f-IVIM per patient, as markers of tumor perfusion, is presented in Table I. The third column of Table I summarizes the % percentage of volume overlap between voxels meeting both criteria of high cellularity (low D) and high vascular permeability (high Ktrans) as described in Correlation Analysis. The mean r values of the patient cohort are greater than 0.5 ($r > 0.5$: linear relationship) only for f-IVIM and vp-GCTT. To graphically illustrate the linear relationship of f-IVIM and vp-GCTT quantile-quantile plots (q-q plots) were also appended in Fig. 5 for a patient with Ewing sarcoma of the shoulder. It is important to note that the corresponding p-values per patient were significantly lower than 10^{-5} for all cases because the analysis was voxel based rather than ROI based.

As a next step, we studied the spatial correlation of the most aggressive tumor areas as indicated by the two different MR methodologies, i.e. cellularity as indicated by D and tumor vascular supply as indicated by DCE Ktrans. A criterion of low D and high Ktrans was set and then the intersection of the two subsets of tumor voxels was graphically represented overlaid on anatomy to constitute a guide for tumor biopsy within such heterogeneous and large masses (Fig. 6,7).

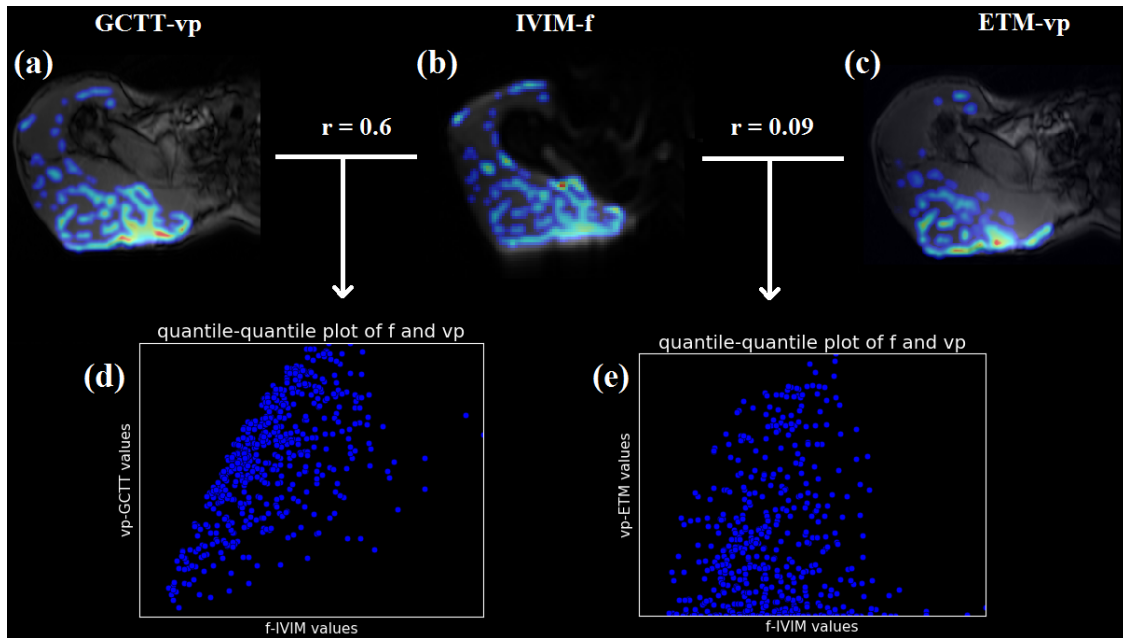


Figure 33. Parametric vp maps for an Ewing sarcoma of the right shoulder computed by: GCTT (a) and ETM (c) models. In the middle IVIM-f parametric map. In the lower part, q-q plot between f and GCTT-vp (d) clearly shows the linear relationship with Pearson's $r = 0.6$ as opposed to f-ETM vp where annr of 0.09 indicates neutral correlation.

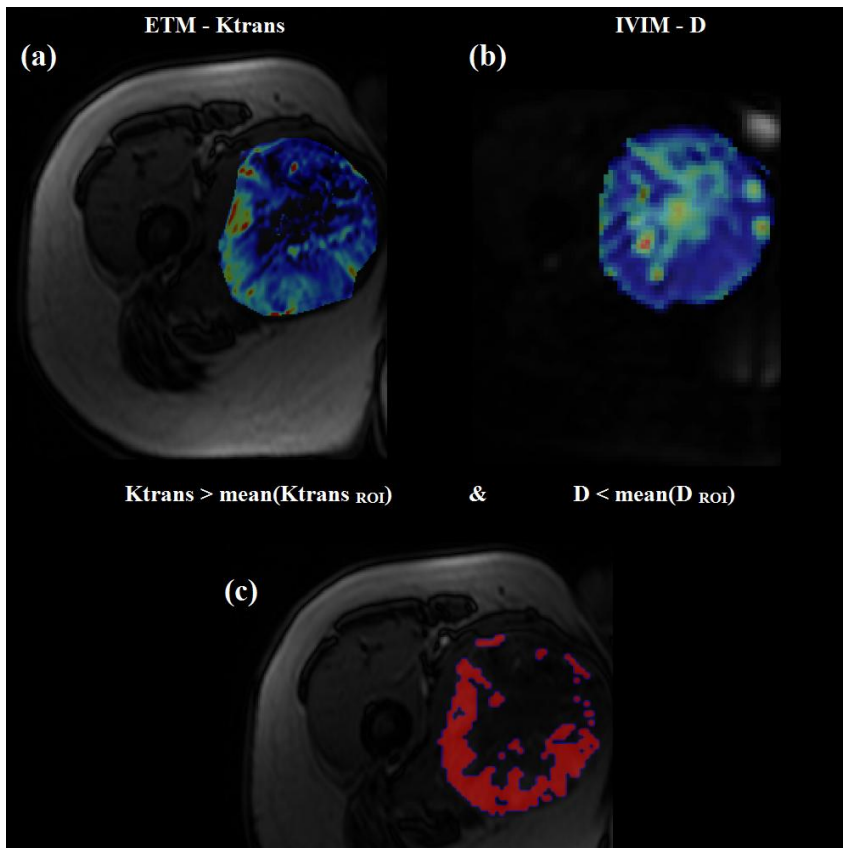


Figure 34 Dedifferentiated liposarcoma of the right thigh. Parametric maps of ETM K_{trans} (a) and IVIM D (b) superimposed on DCE T1 GE and DWI images respectively. The lower image (c) shows the areas meeting both criteria of high K_{trans} (high vascular permeability) and low D (high cellularity.)

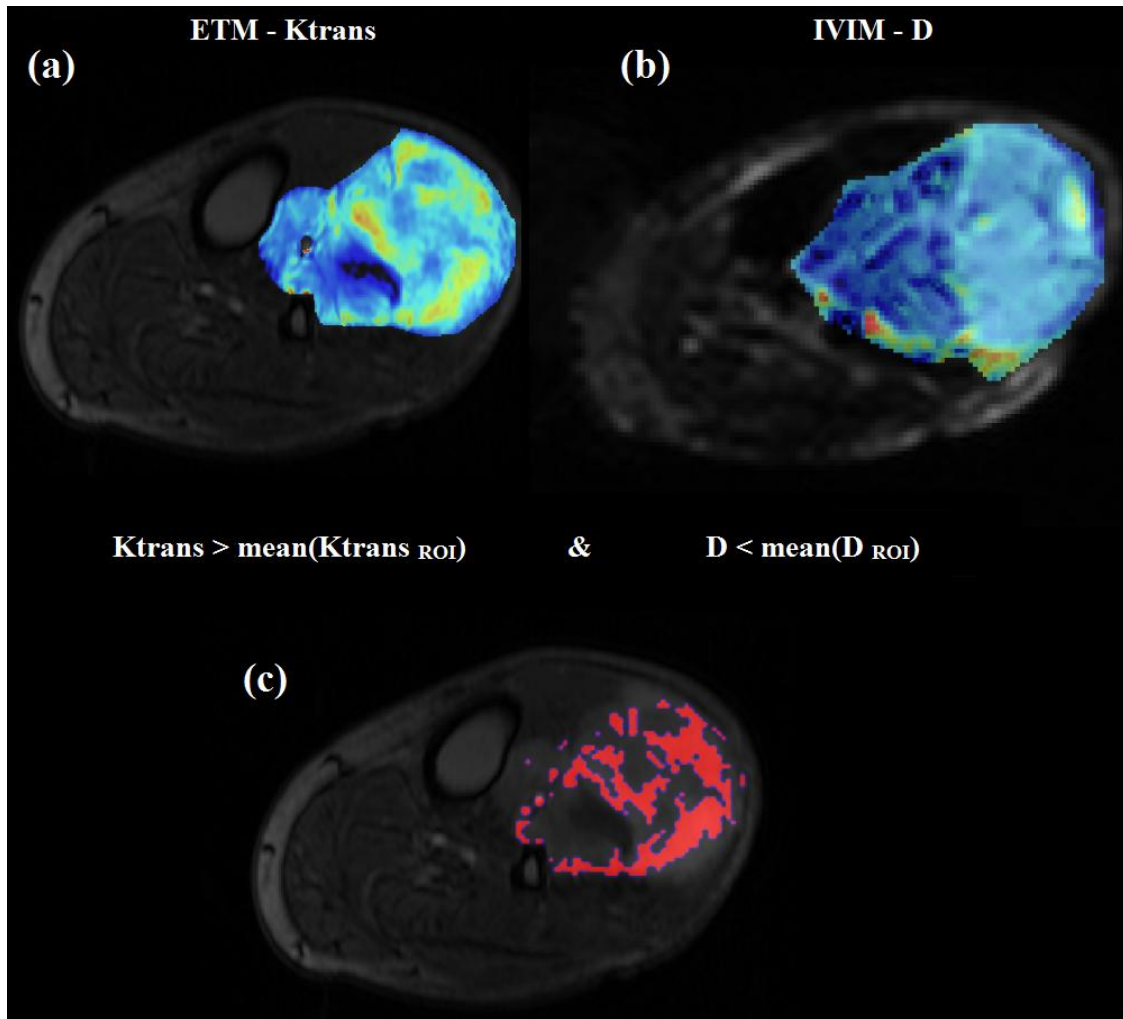


Figure 35 Malignant tumor (MPNST) of the left calf. Parametric maps of ETM Ktrans (a) and IVIM D (b) superimposed on DCE T1 GE and DWI images respectively. The lower image (c) shows the areas meeting both criteria of high Ktrans (high vascular permeability) and low D (high cellularity).

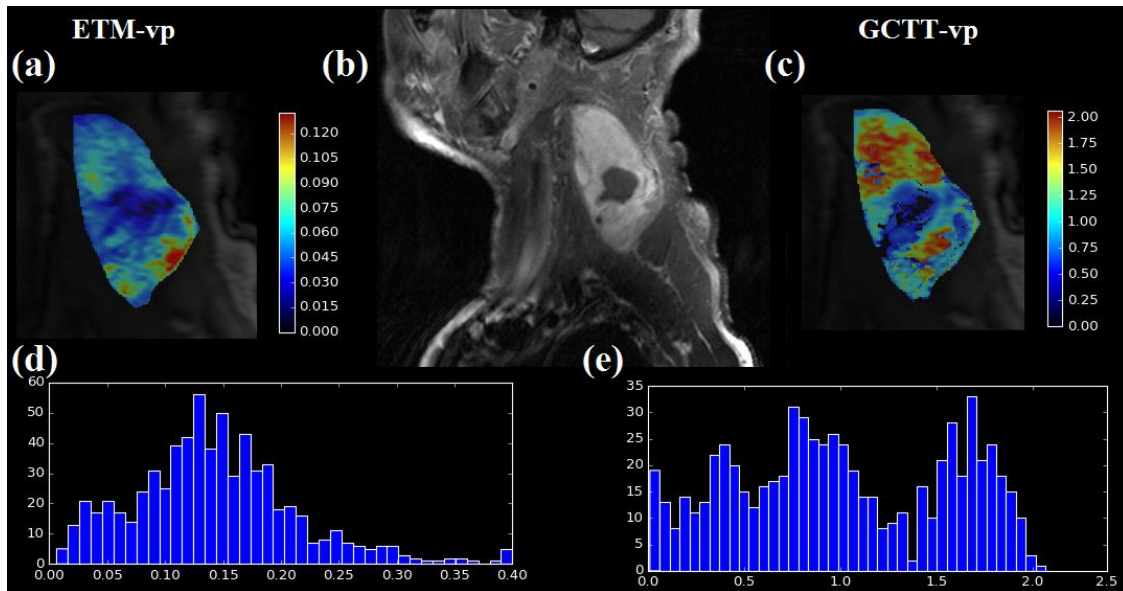


Figure 36 Alveolar soft tissue sarcoma of the neck (same patient as in fig. 1). (a) ETM vp map, (b) parasagittal fat suppressed contrast enhanced T1W MR image. (c) GCTT-vp map, (d) ETM vp histogram, (e) GCTT vp histogram

Table I. Pearson's correlation coefficient between DWI and DCE derived parametric maps and percentages of voxel overlap with high Ktrans and low ADC as described in materials and methods section.

Patients	Pearson's r		DCE-DWI ov
	f-vp ETM	f-vp GCTT	%
p.1	0.310873	0.534515	23.509
p.2	0.181833	0.630569	6.009
p.3	0.149587	0.570498	24.493
p.4	0.24293	0.38424	28.62
p.5	0.608346	0.49826	14.537
p.6	0.413949	0.618321	6.898
p.7	0.019283	0.524793	30.208
p.8	0.30969	0.482717	20.439
p.9	0.468085	0.471851	8.698
p.10	0.208291	0.514515	31.344
p.11	0.168474	0.483627	28.808
p.12	0.46131	0.698278	11.772
p.13	0.050655	0.586594	18.39
p.14	0.485701	0.454904	10.838

p.15	0.41729	0.671383	6.681
p.16	0.600212	0.510584	9.756
p.17	0.164873	0.62538	9.597
p.18	0.417714	0.476529	10.998
p.19	0.224486	0.551787	15.431
p.20	0.311413	0.609723	6.241
p.21	0.166259	0.667271	27.567
p.22	0.340793	0.647787	28.619
p.23	0.205189	0.564165	17.271
p.24	0.361632	0.540817	17.231
p.25	0.375686	0.403571	13.442
mean	0.306582	0.532072	

Table 3

4.4 Discussion

The first aim of the present study was to validate associations of IVIM derived parameters with known DCE models on STT data. Secondly, the most aggressive sub-regions of the tumor were located individually, as indicated either by DWI or DCE and then the spatial correlation between two methods was presented.

Initially we examined the sensitivity of IVIM to measure perfusion related parameters as this could theoretically simplify an MR oncologic protocol including both DWI and DCE sequences and also help to avoid the intravenous injection of contrast medium. This in turn positively affects acquisition time, patient discomfort and imaging cost whereas there are cases that gadolinium administration is clinically contraindicated. Relevant published studies have shown positive correlation of DCE and DWI MRI parameters. Suo et al. performed semi-quantitative perfusion DCE analysis on breast cancer with a 3T MR scanner reported correlation of (f-IVIM) with relative enhancement ratio exhibiting $r = 0.55$ and f-IVIM with AUC with $r = 0.56$ (Suo *et al.*, 2015). In the brain region two correlative DWI-DSC studies by Kim et al. (Kim *et al.*, 2014) and Federau et al. (Federau *et al.*, 2014) reported correlation of f-IVIM and CBV with $r=0.67$ and $r=0.75$ respectively. The experimental DWI protocol of the latter consisted of 16 b-values and this can partially explain the high r value reported. To the best of our knowledge, this is the first DCE and DWI study concerning soft tissue sarcomas.

The results of the first part showed positive correlation between f-IVIM and vp-GCTT with a Pearson's r of 0.532 while the correlation between f-IVIM and vp-ETM was neutral, $r = 0.306$. It is important to note that our analysis sought correlation between all pairs of DWI ($f, D, D^*, f \times$

$D, f \times D^*$) and DCE (Ktrans, Kep, vp, E, F) derived parameters with r values ranging from -0.132 to 0.263 indicating no significant correlation.

DCE derived parameter values and repeatability can vary widely by analytical methodology (Ng *et al.*, 2015). As this work deploys two different models for DCE data quantification differences between parametric maps calculated by GCTT or ETM models respectively are expected because of different assumptions made (number of compartments, directionality of CA transfer between the blood plasma and the EES). Indicatively Fig. 8 shows the differences between vp-GCTT and vp-ETM not only in the absolute values but also in the pattern of the parametric map. This variability is a possible explanation for the positive correlation between vp-GCTT and f-IVIM as opposed to the neutral correlation of vp-ETM and f-IVIM.

With regard to the second part of the analysis, we used the mean value of each biomarker for thresholding but the use of other histogram metrics, such as 5%, 10% percentiles, could have also been used for the same purpose. All patients had non-zero volume overlap between voxels with metrics showing aggressiveness indicated from the two different methodologies. Preliminary results from this study previously reported (Nikiforaki *et al.*, 2018), had shown spatial correlation on a smaller patient population. A frequently encountered finding among the patient cohort was the thresholded DCE-DWI overlap in the periphery of the tumor which was consistent with findings of histopathologic analysis. This in turn shows the possible application of DCE-DWI overlap for preoperative biopsy guidance as in all cases overlapping voxels were not dispersed in the tumor 3D tumor volume but congregated in specific sub-regions as depicted with red in the lower part of Fig. 5 and 6.

The most challenging datasets proved to be in the abdominal region, probably due to respiratory artifacts hampering DCE-DWI alignment and degradation of 4D data quality. Another limitation of our study arises from the necessary step of resizing the DCE parametric maps to match the size of DWI maps. Among available interpolation methods, bicubic interpolation was preferred over linear or nearest neighbor as it outperforms the other two (Pan, Yang and Tang, 2012).

In conclusion, a free correlation study among all DCE and DWI derived pairs of parameters showed a linear relationship between f-IVIM and vp-GCTT in patients with soft tissue sarcomas. Moreover, the spatial relationship between low cellularity and high vascular permeability areas was illustrated as a possible visual guide for pre-operative biopsy.

Chapter 5 T2, T2* and Spin Coupling ratio as biomarkers for the study of lipomatous tumors

5.1 Motivation

It has been reported from the early days of MR imaging that subcutaneous fat may have variable signal intensity on T2w images depending on the choice of imaging parameters and more specifically the time interval between the consecutive RF refocusing pulses. In this part of the study we deployed T2/T2* relaxometry sequences with appropriate parameters in order to quantify T2 and T2* relaxation constants. Moreover, we repeated T2 relaxometry in the absence of spin coupling phenomena in order to quantify spin coupling related signal changes and correlate this information with the degree of differentiation of benign and malignant adipocytic tumors. For this purpose we introduced a specific marker called Spin Coupling ratio, SCR, that represents the % signal difference of signal loss between two different T2 relaxometry acquisition schemes between the lesion and healthy subcutaneous fat. The patients recruited for this study had a diagnosis for lipoma, well differentiated liposarcoma, myxoid liposarcoma, pleomorphic liposarcoma or poorly differentiated liposarcoma. We concluded that T2, T2* and SCR can be used for the classification of fat containing tumors, which may be important for biopsy guidance in heterogeneous masses and treatment planning SCR surpassed the classification performance of T2 and T2* relaxometry.

5.2 Method

Patient Population

During this study twenty patients with lipomatous tumors were recruited for MRI examination with the selected advanced protocol from July 2017 to May 2018. One patient was excluded because of compromised cooperation resulting in severe motion artifacts. All patients had signed an informed consent for the use of clinical and imaging data for research purposes. Surgeon marked the specimen with sutures in predefined points in order to enable the actual three-dimensional orientation of the specimen in relation with the patient's body and to warrant the implementation of sections of the tumor in its true axial plane.

Imaging protocol

All MRI exams were performed on a 1.5T MR scanner. The protocol includes apart from conventional imaging sequences to present the location and the extent of the lesion (a dual echo Proton density and T2w TSE with fat suppression in axial and coronal plane, TR/TE1/TE2/TI: 3360/14/83 msec, 5 mm slice thickness / 0.5 mm gap, 19 slices) functional imaging sequences to highlight showed tumor cellularity (8-b values 2D EPI DWI TR/TE: 2900/100 msec, 5 mm slice thickness / 0 mm gap, b values: 0/50/100/150/200/500/800/1500, 19 axial slices) and vascularity (a dynamic 3D T1w fast low angle shot (FLASH) (TR/TE: 7.09/3.27msec, temporal resolution 7.09 sec 5 mm slice thickness/1.6 mm gap, 14 axial slices). Imaging planes were non-oblique for easier co-localization of imaging slice and site of histological examination.

The T2 quantitative MRI protocol consists of two 2D multislice MESE, PD-to-T2-weighted sequence were obtained with no interslice delay time. For the first sequence: n=25 equidistant spin echoes with TE1=13.4 ms, ESP =13.4 ms and for the second n=10, TE1 =26.8ms, ESP=26.8ms while TR was 2500ms for both sequences.. The latter sequence (10 echoes: 26.8, ... , 80.4,..., 268 ms) was used for T2 relaxometry as it does not suffer from the bright fat appearance from spin coupling while the former sequence (25 TEs: 13.4, 26.8, ..,80.4,..335) was used for subtraction of images between the two relaxometry sequences at identical echo times. Fourteen axial slices of 5 mm slice thickness and 5 mm interslice distance were obtained. A rectangular field of view (280 × 210 mm) with a rectangular reconstruction matrix (256 × 192 pixels) was utilized. The final 3D spatial resolution was therefore: 1.1 × 1.1 × 8 mm³. The MESE sequence was based on a 2D multiecho CPMG spin echo sequence with alternating 180° RF pulses under the phase-alternating-phase-shift (PHAPS) scheme (Fransson

et al., 1993b). A selective refocusing RF pulse scheme was utilized. Additionally, a multi echo T2* MEGRE with 4 in phase echoes (4.77, 9.59, 14.41, 19.23) and 4 out of phase echoes (2.38, 7.18, 12, 16.82) was used for the calculation of T2* maps.

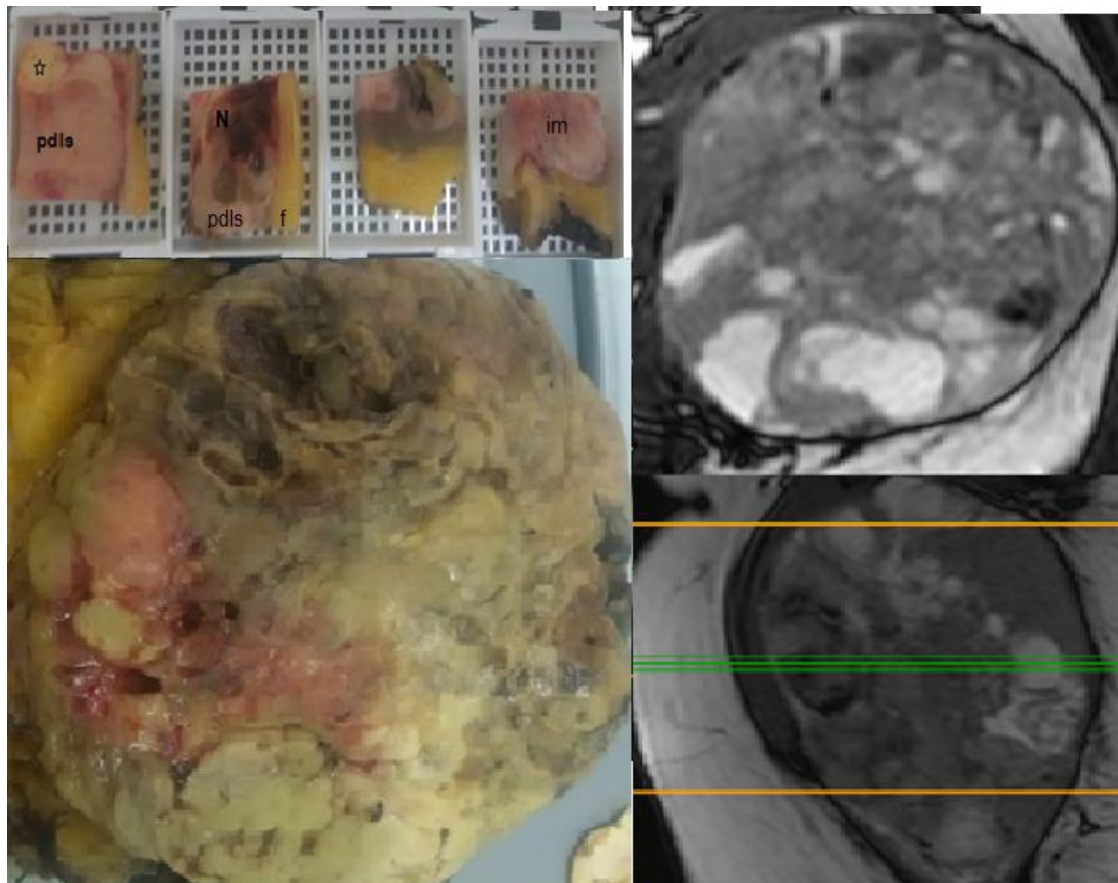


Figure 37 Surgical specimen (dedifferentiated liposarcoma of the thigh). The central slice was divided into 26 orthogonal sections. Area of well differentiated liposarcoma (asterisk) is adjacent to area of poor differentiation (pdl's). Necrotic (N), hemorrhagic areas, infiltrated muscle (im) and fat (f) were identified. Corresponding anatomical T2/T1w images are shown on the right.

Histological Correlation

The intact surgical specimen was transported immediately after excision to the pathology department, where it was delivered to and handled by a trained pathologist who performed the gross examination, photographed and marked the specimen with permanent ink according to the surgical markings and margins. Furthermore, after identifying the upper and lower margins of the tumor, in the superior-inferior direction, parallel sections perpendicular to the axial plane of 1 cm thickness were taken. The central slice of the tumor, corresponding to the

lesion's central imaging slice, was selected after measuring the distances from the upper and lower margins, was divided in orthogonal slabs (in a grid-manner), and placed into plastic cassettes (Fig. 1). Tumor tissue sections were processed according to CAP guidelines and recommendations for specimen handling (Lester, 2010). In brief after 48 hours' fixation into 10 % neutral buffered formalin, sections were embedded into paraffin, dehydrated through a series of graded ethanol baths, infiltrated with wax and then embedded into wax blocks. 4 μ m thick sections of each tumor slab were cut, placed into glass slides, stained with H/E and examined microscopically (Nikon Eclipse E-200) in order to characterize each area of the central tumor slice in terms of differentiation, cell type, cellular atypia, cellularity, mitotic activity, vascularity and presence of necrosis.

The histopathologic topographic characterization guided the imaging post-processing stage so as to recognize the histologically designated "benign", "necrotic", malignant areas and also to conclude on differentiation grade on a very locally restricted area which could be used for ROI measurements. The corresponding site was located on the central imaging slice as distance from the center and angle in a virtual axially located 360 degree cycle.

A case of hibernoma was included in the patient cohort because of its interest but was not included in the statistical analysis as it cannot constitute a category by itself. Data from patients diagnosed with dedifferentiated liposarcoma were assigned as either well or poorly differentiated tissue according to the result of histological examination for the selected slice.

Data post processing

Pixel based parametric T2/T2*maps were produced after mono-exponential fitting of the multi echo MESE/MEGRE data from in-house built software platform (Manikis *et al.*, 2016). Mean T2/T2* was calculated for each Region of Interest (ROI) which was delineated by an expert radiologist within the tumor central slice at a homogeneous region, excluding necrosis and hemorrhage. In the case of dedifferentiated liposarcoma, ROI delineation was performed after the pathologist suggested areas of poor differentiation. Image based calculations (subtraction and division of T2MESE images to calculate relative signal loss at identical TE) were performed with Mango software (Mango Software, Research Imaging Institute, UTHSCSA). Statistical analysis was performed using R. Each examined biomarker was descriptively summarized and presented as mean \pm standard deviation (SD). Pairwise comparisons were assessed quantitatively using Student's T-test. Boxplots depicting the different subject groups were

displayed. For all tests, a p-value of less than 0.05 was considered to indicate statistical significance.

The relative signal loss percentage of the fatty tissue between two T2 acquisitions of different echo spacing, 13.4 ms and 26.8 ms respectively was calculated (Spin Coupling, SC) for all image pixels (Eq. 1).

$$SC = \frac{T2_1 - T2_2}{T2_1} \quad (1)$$

SC value calculated for the tumor ROI was then divided by SC value calculated for subcutaneous fat ROI of the same patient from the same acquisition in order to produce a patient specific metric, Spin Coupling ratio, (SCr) (Eq.2).

$$SC_{ratio} = \frac{SC_{tumor}}{SC_{fat}} \quad (2)$$

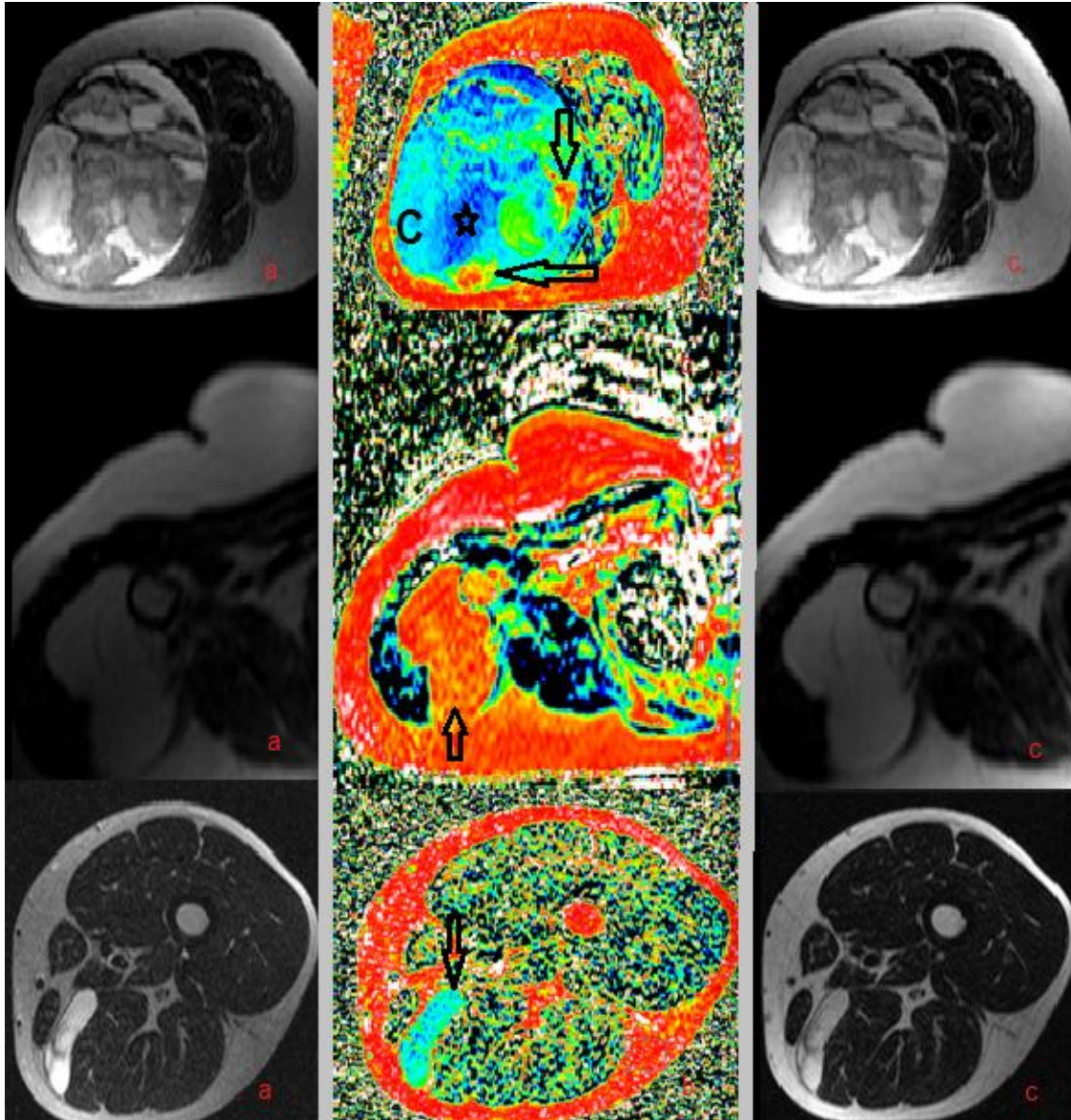


Figure 38 SCratio maps for three lipomatous masses of variable degree of malignancy. Above: Dedifferentiated liposarcoma of the thigh: a) T2 MESE ESP: 26.8 ms, TE: 80.4 ms, b) SCr map [-10, 50] %, c) T2MESE ESP:13.4 ms TE: 80.4 ms. Histopathologic examination confirmed sites of well differentiation at the tumor periphery at locations 6o'clock and 3o' clock respectively at the periphery (arrows) that should be avoided for needle biopsy. Cystic components (C) were also observed and also sites of poor differentiation (asterisk). Fig. 2 middle: Benign Lipoma a) T2 MESE ESP: 26.8 ms, TE: 80.4 ms, b) SCr map [-10, 50], c) T2MESE ESP: 13.4 ms TE: 80.4 ms. Fig. 2 below: Myxoid Liposarcoma Lipoma a) T2 MESE ESP: 26.8 ms, TE: 80.4 ms, b) SCr map [-10, 50], c) T2MESE ESP:13.4 ms TE: 80.4 ms. All MR images are displayed at [0,1000] a.u.

5.3 Results

Resulting pixel based parametric maps of SCr are shown on Fig. 29, complemented by original bright and dark fat T2w images, ROI based mean apparent T2, mean apparent mean T2* were calculated for the lesion as well as for uninvolved fat adjacent to the tumor volume to be used as reference for protocol robustness (Table I). Subcutaneous fat sustains a relatively constant value for mean apparent T2/T2* within the patient population, unlike fat containing tumors that exhibit an extensive range of values. Similarly SCr remains relatively constant for healthy fat among all patients while there is a significant range of measured values between different types of fat containing neoplasms.

Statistical analysis (pairwise t-test with Bonferroni correction) was performed to find significant differences in mean apparent T2, mean apparent T2* and SCr between five distinct categories, i.e lipoma, well differentiated liposarcoma, myxoid liposarcoma, pleomorphic liposarcomas and poorly differentiated liposarcoma. Difference was considered significant for $p < 0.05$, and is marked by * for p between [0.01-0.05), ** for p [0.001-0.01) and lastly marked with *** for p between [0-0.001) as shown in Table II. Non-significant differences are noted as ns. Figure 3 graphically represents SCr results, as this was proved (from results shown on Table II) the metric with the higher discriminative power among all three.

It is of note that only SCratio succeeded in classification between pleomorphic liposarcoma and poorly differentiated part of dedifferentiated liposarcoma, both of which are graded as highly malignant (histologic specific grade: 3) and have similar imaging characteristics.

No metric could find significant differences between lipoma and well differentiated liposarcoma in the 5-class problem. However, when performing a 2-class classification between the two classes of low malignancy and very similar imaging characteristics, SCr shows significant differences between lipoma and well differentiated liposarcoma while all the other metrics fail (Figure 4 left).

Furthermore a pairwise t-test was performed between an “extended” class including two entities (lipoma and well differentiated liposarcoma) tested versus healthy subcutaneous fat visible in the same acquisition based on T2 relaxation constant. Significant differences are found between tumors and normal appearing adjacent fatty tissue (Figure 4 right).

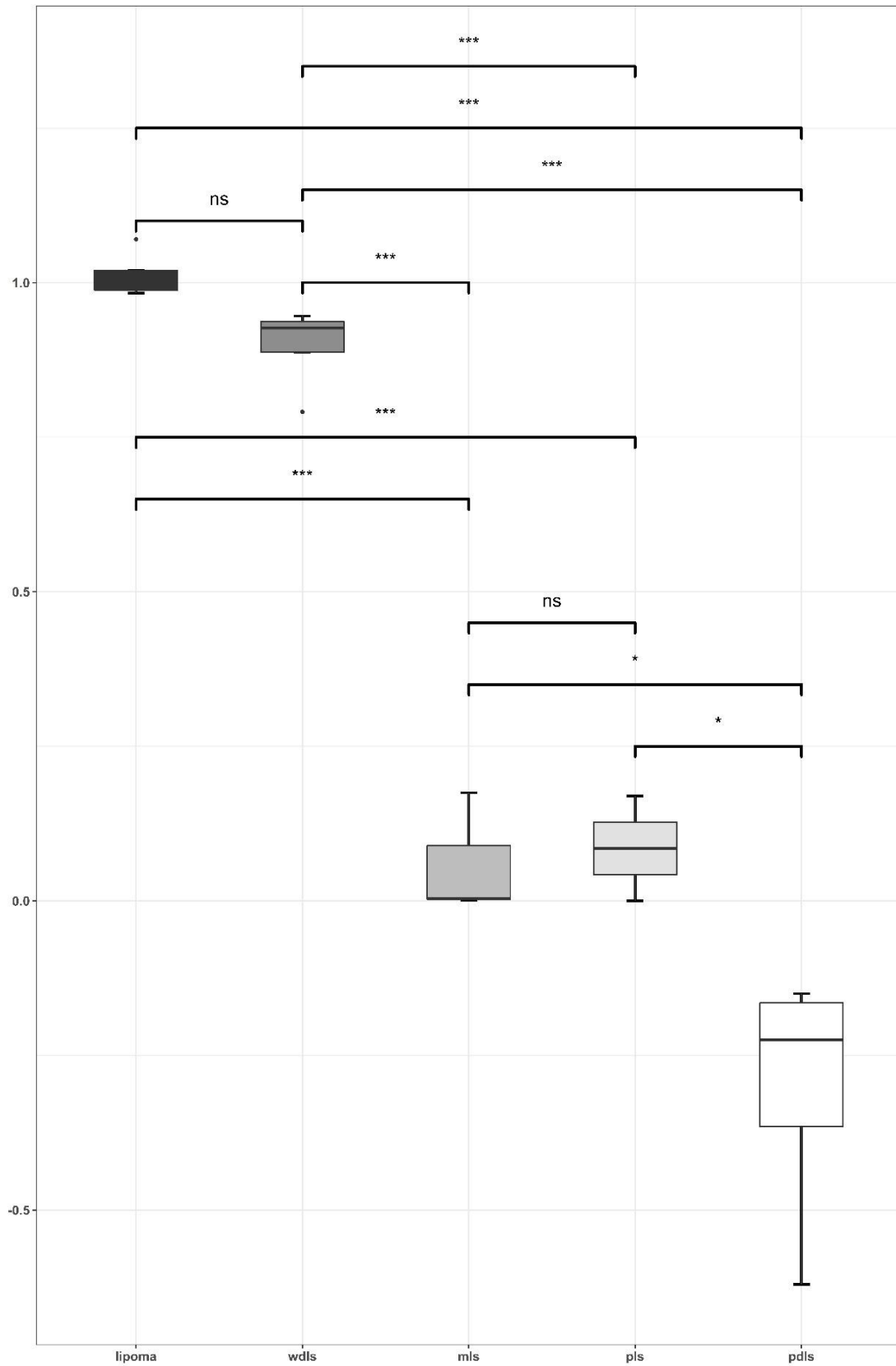


Figure 39 Box plot graphically representing mean value and standard deviation for each category based on SCr. for all lipomatous tumor types. p-value is marked by “*”, “**”, “***”, and “ns” for values between [0.01-0.05), [0.001-0.01), [0-0.001) and [0.05-1] respectively.

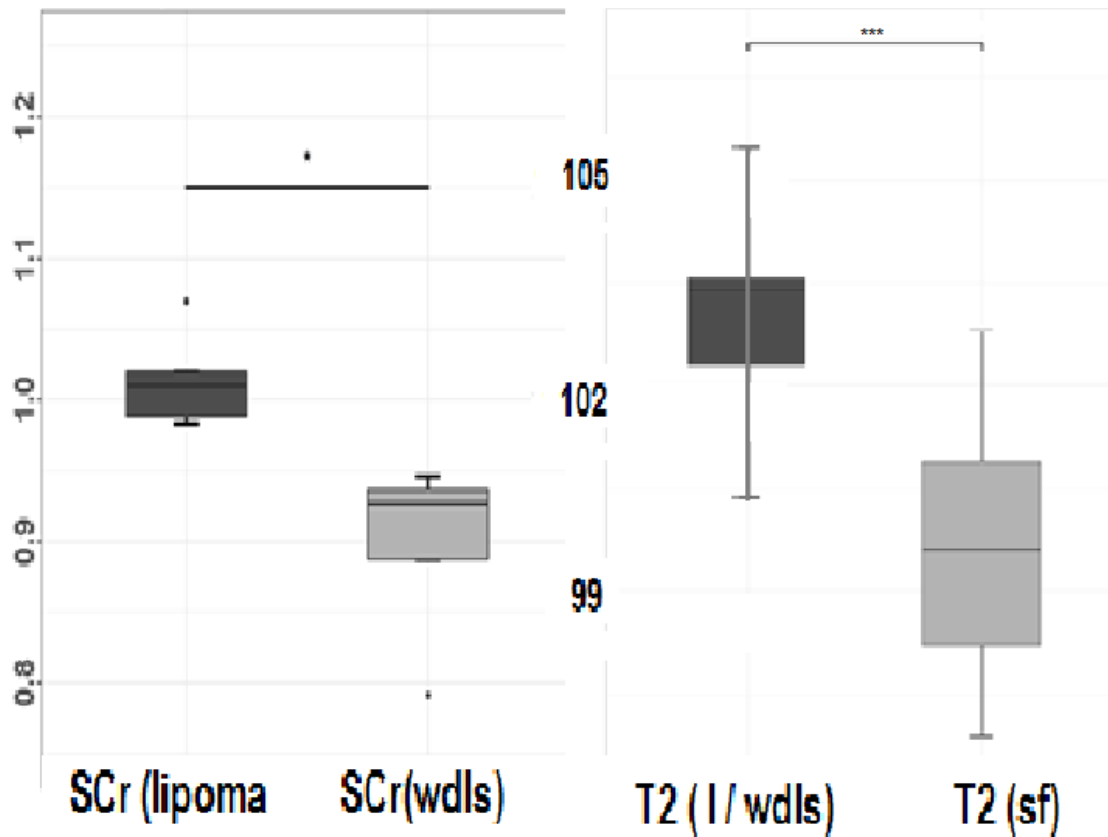


Figure 40 Classification problem simplified to two categories. Left: Significant difference is found between lipoma and well differentiated liposarcoma based on SCr. Right: Lipoma or well differentiated liposarcoma have significant differences in measured T2 value from uninvolved subcutaneous fat (sf)

Table 4. T2, T2*, Spin coupling percentage (SC) and Spin Coupling ratio (SCr) for 5 lipomas, 1 hibernoma (not included in further statistics), 4 well differentiated liposarcomas (wlds), 3 myxoid liposarcomas (mls), 2 pleomorphic liposarcomas and 4 poorly differentiated liposarcomas (pdls). Subscripts l and sf declare lesion and subcutaneous fat respectively. SCr is the ratio of spin coupling loss of the lesion over the same value of uninvolved healthy fat of the same acquisition. SD = Standard Deviation

	T2l (ms)	T2sf (ms)	T2*I (ms)	T2*sf (ms)	SCI (%)	SCsf (%)	SCr I
lipoma 1	104,9	102,8	31,4	29,8	39,9	40,4	0,99
lipoma 2	100,4	100,9	29,2	28,0	41,3	42,0	0,98
lipoma 3	103,6	96,9	30,8	30,6	37,8	36,9	1,02
lipoma 4	102,3	99,6	28,6	29,5	38,7	36,2	1,07
lipoma 5	103,5	98,0	30,4	30,6	40,1	39,8	1,01
Mean	102,9	99,6	30,1	29,7	39,6	39,1	1,01
SD	1,5	2,1	1,0	1,0	1,2	2,2	0,03
hibernoma	196,7	96,5	103,7	29,2	-0,4	35,2	-0,01
wdls 1	103,4	99,7	44,6	29,8	36,7	39,8	0,92
wdls 2	102,5	98,7	28,8	28,5	37,1	39,7	0,93
wdls 3	101,5	98,2	31,7	29,3	49,0	51,8	0,95
wdls 4	105,5	102,0	57,3	28,4	31,9	40,3	0,79
Mean	103,2	99,7	40,6	29,0	38,7	42,9	0,90
SD	1,7	1,5	11,3	0,6	6,3	5,1	0,1
mls 1	572,0	99,5	287,0	32,0	0,2	40,5	0,00
mls 2	535,1	99,4	370,7	29,6	0,1	36,9	0,00
mls 3	383,8	100,5	282,4	28,8	7,3	41,7	0,18
Mean	497,0	99,8	313,4	30,1	2,5	39,7	0,06
SD	99,7	0,6	49,7	1,7	4,1	2,5	0,1
pls 1	144,6	100,2	78,6	28,5	6,1	34,9	0,17
pls 2	135,4	104,7	90,1	29,0	0,0	34,1	0,00
Mean	140,0	102,5	84,4	28,8	3,1	34,5	0,09
SD	6,5	3,2	8,1	0,4	4,3	0,6	0,1
pdls 1	145,4	100,7	69,3	27,1	-20,1	32,1	-0,62
pdls 2	169,3	94,9	129,5	29,5	-6,2	41,4	-0,15
pdls 3	144,3	100,5	84,4	28,8	-12,6	45	-0,28
pdls 4	131,9	99,7	59,4	30,2	-7,1	41,8	-0,17
Mean	147,7	98,9	85,6	28,9	-11,5	40,1	-0,3
SD	15,6	2,7	31,0	1,3	6,4	5,6	0,2

Table 5. Classification performance for T2, T2*, SC and SCr between lipomatous tumors. p-value is marked by “*”, “**”, “***”, and “ns” for values between [0.01-0.05), [0.001-0.01), [0-0.001) and [0.05-1] respectively.

T2	lipoma	wdls	mls	pls	SC	lipoma	wdls	mls	pls
wdls	ns				wdls	ns			
mls	***	***			mls	***	***		
pls	ns	ns	***		pls	***	***	ns	
pdls	ns	ns	***	ns	pdls	***	***	*	ns
T2*					SCr				
wdls	ns				wdls	ns			
mls	***	***			mls	***	***		
pls	ns	ns	***		pls	***	***	ns	
pdls	ns	ns	***	ns	pdls	***	***	*	*

5.4 Discussion

Fat quantification and fat content determination has been a long-standing target of quantitative MRI. To our knowledge, the first use of spin coupling as contrast for clinical imaging was published in 1993 (Todd Constable, Smith and Gore, 1993).

Currently, the most widely used NMR based method for the study of tissue structure is *in vivo* MR spectroscopy. It offers direct recognition of each spectral peak and its relative amplitude for a given sample, but it has many inherent constraints that prevent extensive use in a routine basis. It requires special software and post processing, human expertise, adequate sample homogeneity and main field homogeneity. *Ex-vivo* ^{13}C MRS has been used by S. Singer *et al.* to differentiate between fat-containing tumors based on tissue biochemistry (Singer *et al.*, 1997). The major findings of this study were significant differences in the fatty acyl chain content (ratio between lipomas: wdl: pls or dediff. liposarcomas is 1 : 3 : 0.01) probably attributed to the increase of the poly-unsaturation degree of high grade sarcomas as compared to intermediate or low grade. The latter suggests an increase in the number of double bonds present in the fatty acyl chain which affects the motion and order of the acyl chain and in turn affects membrane proteins. This can be an important factor determining the invasive and metastatic capacity of the high grade liposarcoma cell types. Moreover, they remarked the presence of free fatty acids and phospholipids in dedifferentiated/pleomorphic sarcomas which were not detectable in normal fat, lipoma or well differentiated liposarcoma.

The proposed method based on spin coupling ratio does not rely on direct detection of tissue composition but taking into account the biochemical differences observed in the spectrum, changes in lipid specific imaging contrast are expected. Differences in the measured S_{Cr} show variable degree of dependence on refocusing pulse spacing and may be indicative of differences in the fat content of adipocytic neoplasms. Subcutaneous fat exhibits a very narrow and specific range of all T₂ and Spin Coupling related metrics instead in the resulting changes of signal produced. S_{Cr} calculation does not require special hardware or software nor post processing expertise. It requires minimal acquisition time and has excellent spatial resolution, exploiting rather than being weakened by tissue heterogeneity as in the case of MR spectroscopy.

Results of the present study show that T₂ relaxometry in conjunction with spin coupling ratio can achieve differentiation between any pair of the five different adipocytic moieties. As seen in Fig. 3 S_{Cr} decreases with increased differentiation grade. Well differentiated liposarcomas lose a significant percentage (38.9%) of their signal due to spin coupling at TE=80 ms which is comparable to normal fat signal loss (42.9%), myxoid have almost identical signal intensity

between the two acquisitions-probably because of the dominant long T2 component- and, at the other end, pleomorphic and poorly differentiated tumors have even lower SCr. In fact, the latter group exhibits negative values which was unexpected as zero loss was considered to be the lower limit by theory. However this finding was consistent among all examined patients and requires more detailed study in a molecular and chemical level.

In fast SE sequences each echo reading has a distinct phase encoding in order to represent a different line of k-space within a given TR interval .The effect of spin coupling in signal modulation cannot be decomposed and measured separately to other concurrent spin dephasing phenomena during acquisition, such as magnetization exchange effects, stimulated echoes or diffusion of water molecules through a local field inhomogeneities (Constable *et al.*, 1992). However, the process of subtraction of images with identical parameters apart from ESP accentuates contrast mechanisms affected significantly by pulse spacing. For this reason, we believe that, if not uniquely, the observed differences can be attributed mainly to spin coupling.

A definite constrain of our study is the number of patients that participated in the study but these preliminary results show that SCr can be introduced into the clinical routine and to build a larger database for use in the future. However it is promising that structures of similar origin but different molecular inner structure or composition have a different imaging identity and the proposed biomarker of spin coupling ratio highlights the imaging spectrum of fat that remains otherwise unperceivable.

Chapter 6 Combined qualitative inverse Laplace transform and multi-exponential fitting study of T2 relaxometry data on a fat containing phantom: application of multi-exponential fitting on adipocytic tumors

6.1 Motivation

The aim of this part of the study is to qualitatively evaluate the transverse relaxation properties of fat containing samples by deploying two different methodologies: inverse laplace transform (ILT) which is the gold standard and a proposed method based on mono and double exponential fitting. The number of discrete exponentially decaying components is derived by statistical methods and are then correlated with the spectrum of T2 components as obtained by the ILT method for validation. In order to validate the results against the ILT method, we use a phantom with samples of known exponential decay patterns of the transverse magnetization and different compositions, either aqueous or fatty or mixed aqueous and fatty with variable percentages. The proposed method is then applied to benign and malignant lipomatous soft tissue masses to reveal the different decaying patterns depending on the histologic similarity of the lesion to the normal adult fat cell (cell differentiation).

Taking into account that the number of exponentially decaying proton compartments depends on tumor tissue micro-environment, a voxel by voxel tissue description with no a priori assumption for the number of exponential components can contribute to a non-invasive characterization of fat containing soft tissue masses and support radiological diagnosis.

6.2 Method

Patient Population - Histological assessment

The imaging protocol was submitted and approved by the local ethics committee. All patients signed an informed consent for the use of clinical and imaging data for research purposes.

Patients with primary lipomatous tumors who underwent MRI examination from July 2017 to February 2019 prior to the planned surgical excision were included in the study. Patients with recurrent or residual tumors and those submitted to preoperative treatment were excluded. Subsequently, one patient was excluded because of compromised cooperation resulting in severe motion artifacts and two patients that refused to perform the examination because of claustrophobia. A total of 24 patients with primary lipomatous tumors of the lower limb (11), the upper limb (7) and the retroperitoneal space (6) were studied. The surgeon marked the specimen with sutures or surgical staples in predefined points in order to enable the actual three-dimensional orientation of the specimen in relation with the patient's body and to warrant the implementation of sections of the tumor in its true axial plane. For each patient at least 3 slices (at the top and bottom end and a slice in the middle of the tumor) were analyzed in terms of differentiation, cell type, cellular atypia, cellularity, mitotic activity, vascularity and presence of necrosis. Histopathologic analysis revealed 6 lipomas, 4 well-differentiated liposarcomas, 3 myxoid liposarcomas, 4 pleomorphic liposarcomas and 7 dedifferentiated liposarcomas.

Imaging protocol

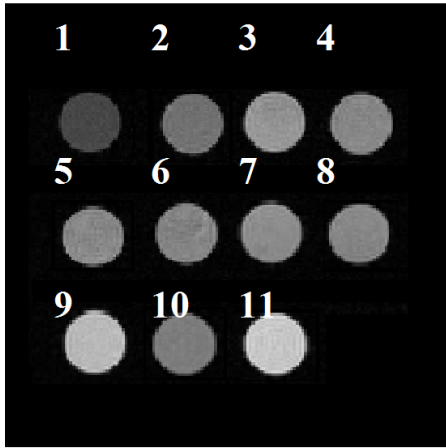
All MRI exams were performed on a 1.5T MR scanner (Vision/Sonata hybrid System, Siemens, Erlangen, Germany). For the patient study, conventional dual echo turbo spin echo (PD and T2) as well as T1 sequences offered complete coverage of the region in question and were used for the design of quantitative study. The Field of View (FOV) and the choice of the coil depended on the site of the tumor and were determined on the basis of highest SNR and adequate spatial coverage. Two possible schemes were used for the FOV, either 200 x200 or 400x400 as masses differed substantially in their size. The T_2 quantitative MRI protocol consisted of 2D single slice Multi Echo Spin Echo (MESE) based on a 2D multi echo Carr-Purcell-Meiboom-Gill (CPMG) spin echo sequence with alternating 180° RF pulses under the phase-alternating-phase-shift (PHAPS) scheme (Fransson *et al.*, 1993a). The final result was a single slice, PD-to-T2-weighted sequence with no interslice delay time. PD-to-T2-weighted sequence were obtained with no interslice delay time. A TR of 2500 ms, using 25 equidistant spin echoes (TEs starting at 13.4 ms, Echo Spacing, ESP = 13.4 ms, last TE = 335ms). 7 to 14 axial slices, depending on tumor size, of 5 mm slice thickness and 5 mm inter slice gap were obtained. A rectangular reconstruction matrix (384 × 320 pixels) was chosen. The same single slice MESE sequence was used for the phantom study, with a standard FOV of 230 x 144 mm. A selective refocusing RF pulse scheme was utilized for elimination of stimulated echoes (Hennig, 1991).

Data pre-processing

In the MESE/PHAPS sequence the first echo signal is not accurate because of B1 field imperfections (Milford *et al.*, 2015) (Majumdar *et al.*, 1986) and is usually either extrapolated or ignored. In this study we did not correct for the first echo as extrapolation process requires the choice of a proper model and this would in turn introduce bias to the next step of mono or double exponential fitting model selection. The first TE used for both ILT and the multi-exponential T2 analysis was therefore, the second acquired TE at 26.8 ms. from the original MESE/PHAPS sequence. This confounds the minimum bound for T_2 estimation, which was chosen at 30 ms for the present study.

Phantom study

As a first step the fitting method was tested on an in-house built phantom composed of 11 samples with different relaxation patterns. More specifically mixtures with variable fat/water content (milk cream with different fat content and mixtures of different number of egg yolks and whites), pure corn oil and double distilled water were analyzed with the same sequence.



- 1: Acetone**
- 2: Double Distilled Water**
- 3: Milk Cream 35%**
- 4: Milk Cream 20%**
- 5: Milk Cream 15%**
- 6: Milk Cream 12%**
- 7: 1 White 3 Yolks (mix)**
- 8: 3 White 1 Yolk (mix)**
- 9: 1 White 1 Yolk (mix)**
- 10: 1 Yolk**
- 11: Corn Oil**

Mono-Bi exponential model classification

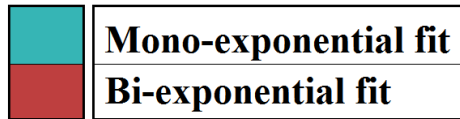
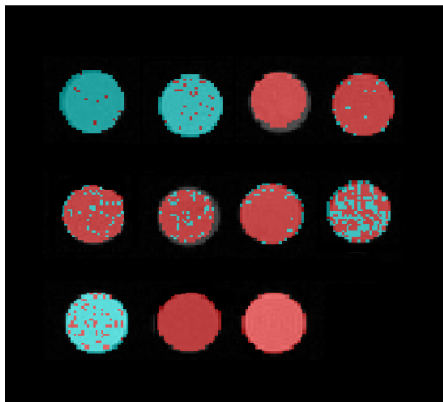


Figure 41 Phantom configuration and multi-exponential classification of the samples

T_2 relaxometry

All numerical calculations concerning Mexp T_2 relaxometry were implemented in Python 3.5 (www.python.org) apart from the ILT method which was implemented in Matlab (MathWorks, Natick, Massachusetts) . The graphical user interface (GUI) and results visualization were accomplished by the use of PyQt4 and PyQtGraph (www.pyqtgraph.org) libraries respectively. Below the mathematical framework and technical details for the T_2 relaxation are presented below.

Inverse Laplace Transform method

A continuous MR relaxometry signal $y(t)$ is of the form:

$$y(t) = \int_0^{\infty} e^{-\frac{t}{T_2}} f(T_2) dT_2 + e(t) \quad (2)$$

Where, T_2 denotes the relaxation time, $f(T_2)$ represents the amplitude of the corresponding component and $e(t)$ is the instrumentation noise. After the discretization of (2) the goal is to extract the distribution of the $f(T_2)$ amplitudes through (3) below.

$$g(t_i) = y(t_i) - e(t) = \sum_{j=1}^N e^{-\frac{t_i}{T_{2j}}} f(T_2) \quad (3)$$

In equation (3) the index i stands for the number of echoes. In matrix notation the main aim is to solve the linear system $g = Af$ where: $A_{ij} = e^{-\frac{t_i}{T_{2j}}}$ is the discrete Laplace transform and $g(t_i) = y(t_i) - e(t)$. For the purpose of our analysis $e(t)$ was considered to be the vector containing the mean background noise for every TE. The problem thus is to find the vector f by minimizing (4) below.

$$f = \arg \min_{f \geq 0} \|g - Af\|_2^2 \quad (4)$$

Taking into consideration that the inverse Laplace transform is a highly ill-posed problem and therefore intrinsically affected by numerical instability, its solution may not be unique. To address this limitation, a penalty term (a) is introduced (Tikhonov, A. N. and Arsenin, 1977) to increase stability in the inversion as illustrated in (5). This technique is known as Tikhonov regularization.

$$f = \arg \min_{f \geq 0} \|g - Af\|_2^2 + a \|f\|_2^2 \quad (5)$$

Additionally, for the phantom study, signal $y(t)$ was the mean ROI signal from all voxels assigned as a certain sample. Lastly, the Matlab's `fminsearch` function equipped with the Nelder-Mead simplex direct search was used to obtain the vector f with $a = 0.01$.

Proposed T_2 Multi-exponential Analysis (Mexp method)

Supposing an MR signal $S(TE_k)$, measured at echo times TE_k ($k = 1, 2, \dots, K$), the decay of the transverse magnetization can be represented as the sum of up to N exponential decays as shown in (6).

$$S(TE_k) - e(TE_k) = \sum_{i=1}^N A_i \exp\left(-\frac{TE_k}{T_{2i}}\right), \quad N = 1, 2 \quad (6)$$

Whittall and MacKay in (Whittall and MacKay, 1989) stated that mono or bi-exponential analysis of materials with different T_2 time constants is relatively accurate as opposed to more complex systems with $N \geq 3$ the T_2 relaxometry is a nontrivial problem. Thus, our analysis was based on searching a maximum of two components. To be more precise, for every voxel in the region of interest Eq. (6) was fitted twice for all N (N = 1,2) meaning mono and double exponential fit respectively by using non-linear least squares (NLLS). The number of exponentials was determined by the highest \bar{R}^2 described in the “Goodness of fit” section.

As an iterative procedure, NLLS needs to be provided with an initial starting point which can be considered as a disadvantage because an inaccurate starting point might lead to NLLS convergence to a local minimum rather than the global minimum. This limitation is handled by repeating the procedure of fitting with different starting points for converging to the global minimum (Li *et al.*, 2016) (typically by comparing the norm of the residuals between each fit). NLLS have the advantage of passing arguments such as the bound constraints for each variable for optimization. In our case, the optimization of (6) was succeeded with $A_i, (i = 1,2)$ in the range of 0 to 2000 and $T_{21} \in [30, 120] \text{ ms}$ and $T_{22} \in [120.1 2000] \text{ ms}$. The trust region reflective algorithm of the `scipy.optimize.least_squares` (www.scipy.org) was used in order to extract A_i and T_{2i} values from the raw relaxometry data. To avoid local minima, the fitting process for every voxel and model was performed 20 times having as an initial starting points equally distributed within the range of each parameter bound. NLLS is preferable to ILT for voxel-wise T_2 mapping as it has lower computational cost. It is worth noting that even for a single voxel the ILT method returns a T_2 distribution (vector outcome for each voxel) rather than a discrete T_2 value. Similarly, for a ROI study the ILT result is a distribution where the metric of interest is the shape and number of the distinct T_2 peaks.

Goodness of fit

Having an analytical form of the model fitted to the data, the adjusted R squared (\bar{R}^2) can be computed in order to acquire information about the goodness of fit. \bar{R}^2 is a generalized metric based on the R squared (R^2) and its value is always less than or equal to that of $R^2 \in [0,1]$. This metric was proposed to overcome the limitation of R^2 concerning that its value increases when more explanatory variables are added to the model. Therefore, \bar{R}^2 was considered more suitable for this study than R^2 since it takes into account the number of data points (K), the number of the explanatory variables (m) of the model function and the residuals between the model function (G_i) and the data (y_i) as can be seen in equations (7) and (8). Index i stands for the number of the measured data points.

$$\bar{R}^2 = 1 - (1 - R^2) \frac{K - 1}{K - m - 1} \quad (7)$$

$$R^2 = 1 - \frac{\sum_{i=1}^k (G_i - \bar{y})^2}{\sum_{i=1}^k (y_i - \bar{y})^2} \quad (8)$$

A graphical representation of the workflow used in this study is shown in Fig. 431

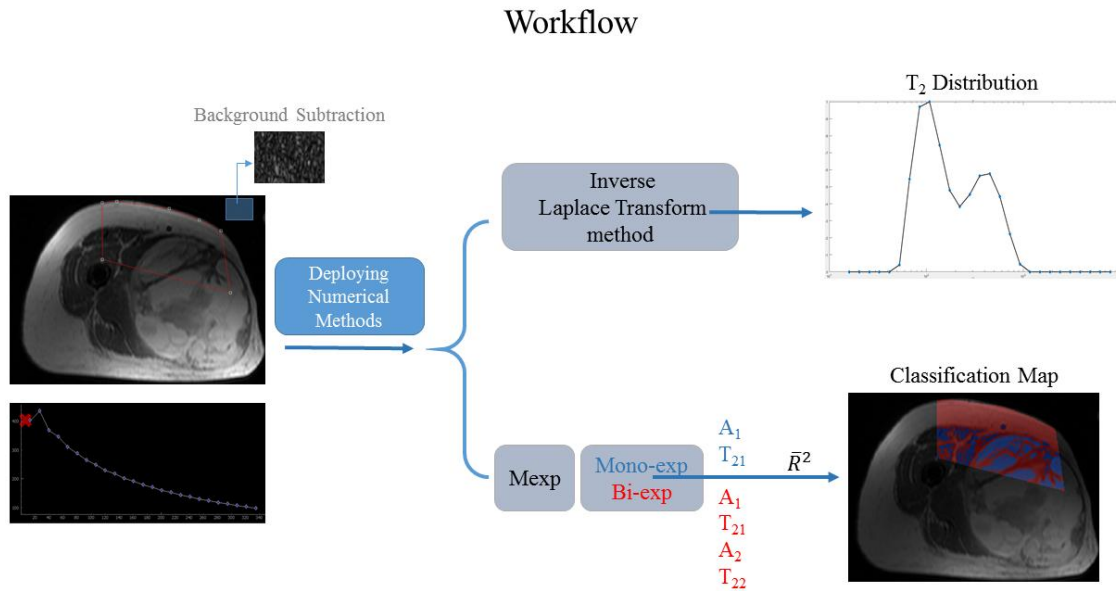


Figure 42 Study workflow

6.3 Results

Phantom study

Eleven samples with different composition were analyzed using both T_2 relaxometry methods in order to test the proposed Mexp method in regard to the number of distinct T_2 components. Sample composition varied from aqueous, to pure fat containing also mixtures of variable fat ratio. Aqueous samples, acetone and double distilled water were positioned in 1-2 respectively, showing $\geq 97\%$ mono exponential behavior by Mexp method Fig. 2. This result is in agreement with the results from ILT method showing a single T_2 distribution characteristics such as the mean value Fig. 343.

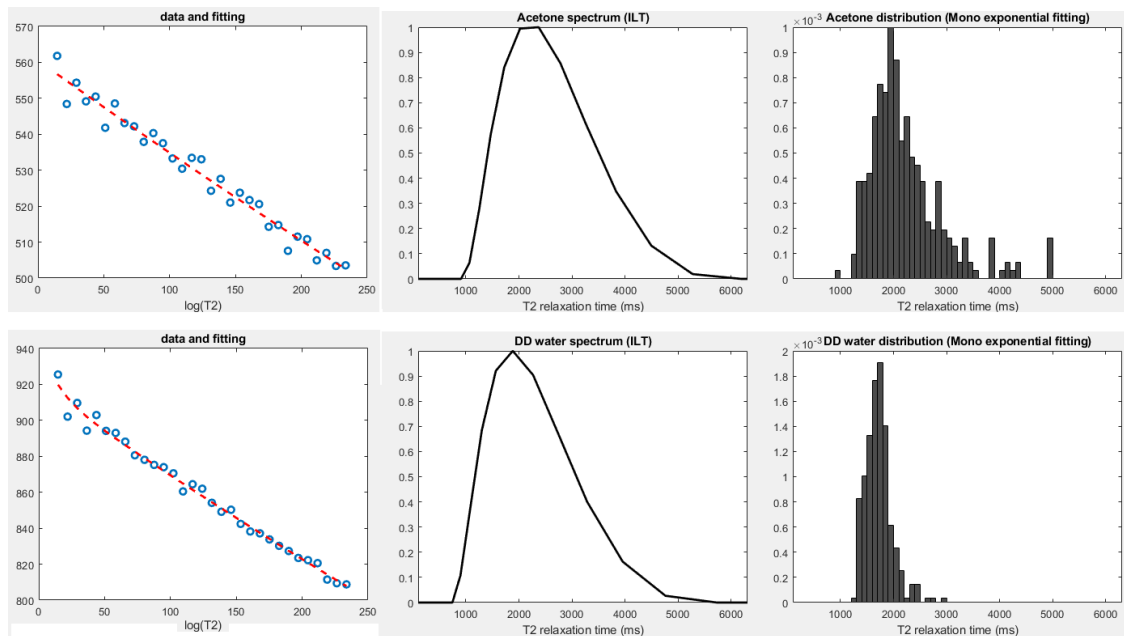


Figure 43 Data fitting, ILT distribution and Mexp results for aqueous samples

In analogy, the estimation regarding the number of components from different fat samples (Egg yolk and corn oil in positions 10 and 11 respectively) exhibited the presence of two different relaxation components for the 100% for the sample voxels Fig. 4. Since imaging data from healthy appearing adipose tissue were available, we extended our analysis to a subcutaneous fat ROI showing 100% bi-exponential behavior (also appended in Fig. 4).

Mixtures of aqueous and fatty composition were also studied and presented in Fig. 345 and Fig. 346.

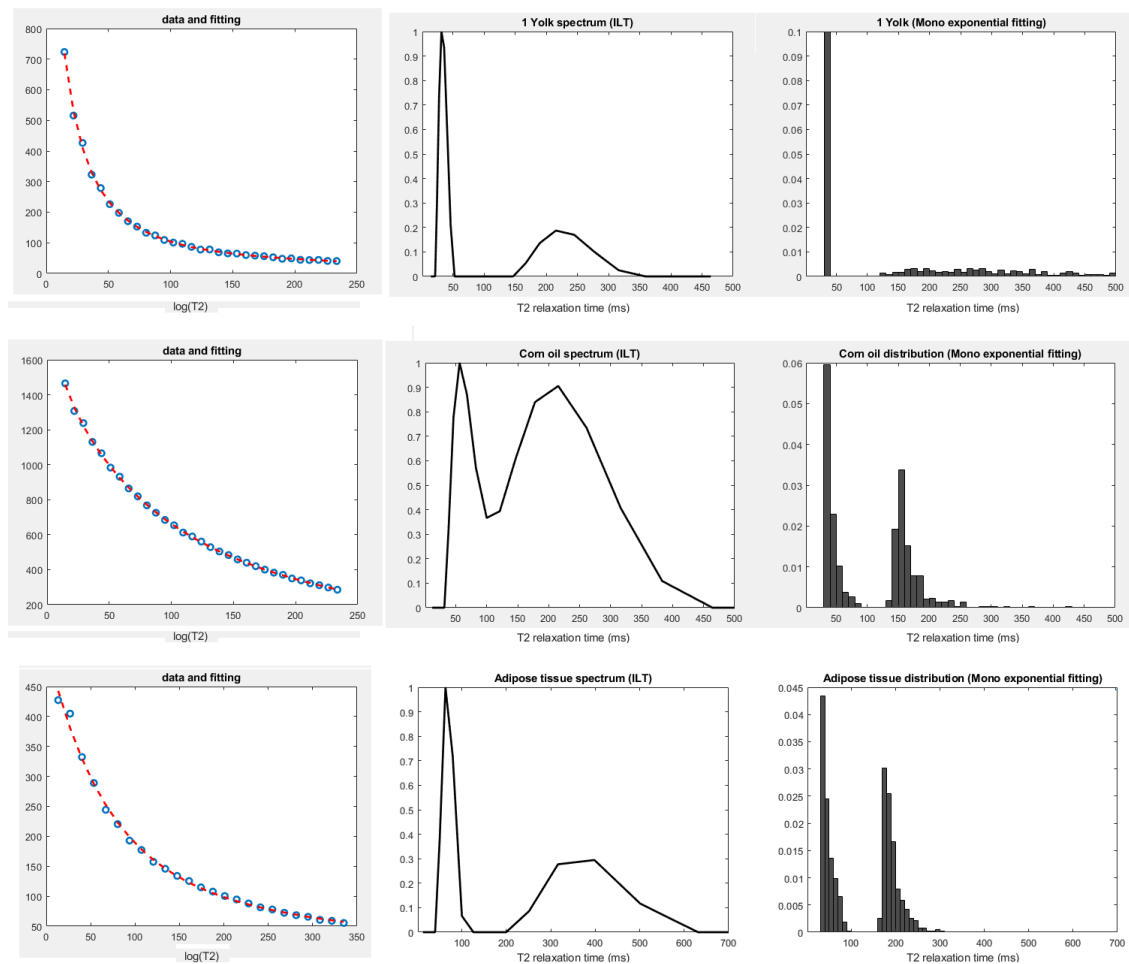


Figure 44 Data fitting, ILT distribution and Mexp results for egg yolk, corn oil and adipose tissue..

Specifically, milk creams with different fat contents, namely: 35, 20, 15 and 12% present in positions 3,4,5 and 6 respectively (Fig. 2), showed dominance of the bi-exponential model with variable degree of voxel percentage. This result was in agreement with the result obtained from the ILT analysis. Bi-exponential dominance varied from 100% to 85% voxel percentage for milk creams of 35% and 12% respectively, with increased fat content favoring double exponential pattern for all 4 samples. Furthermore, the area of the shorter T_2 component distribution varies with fat content, as it seems to progressively decrease with decreasing fat content. A mono-exponential behavior was observed in a voxel percentage of above 10% only for milk cream with the least fat content (12%).

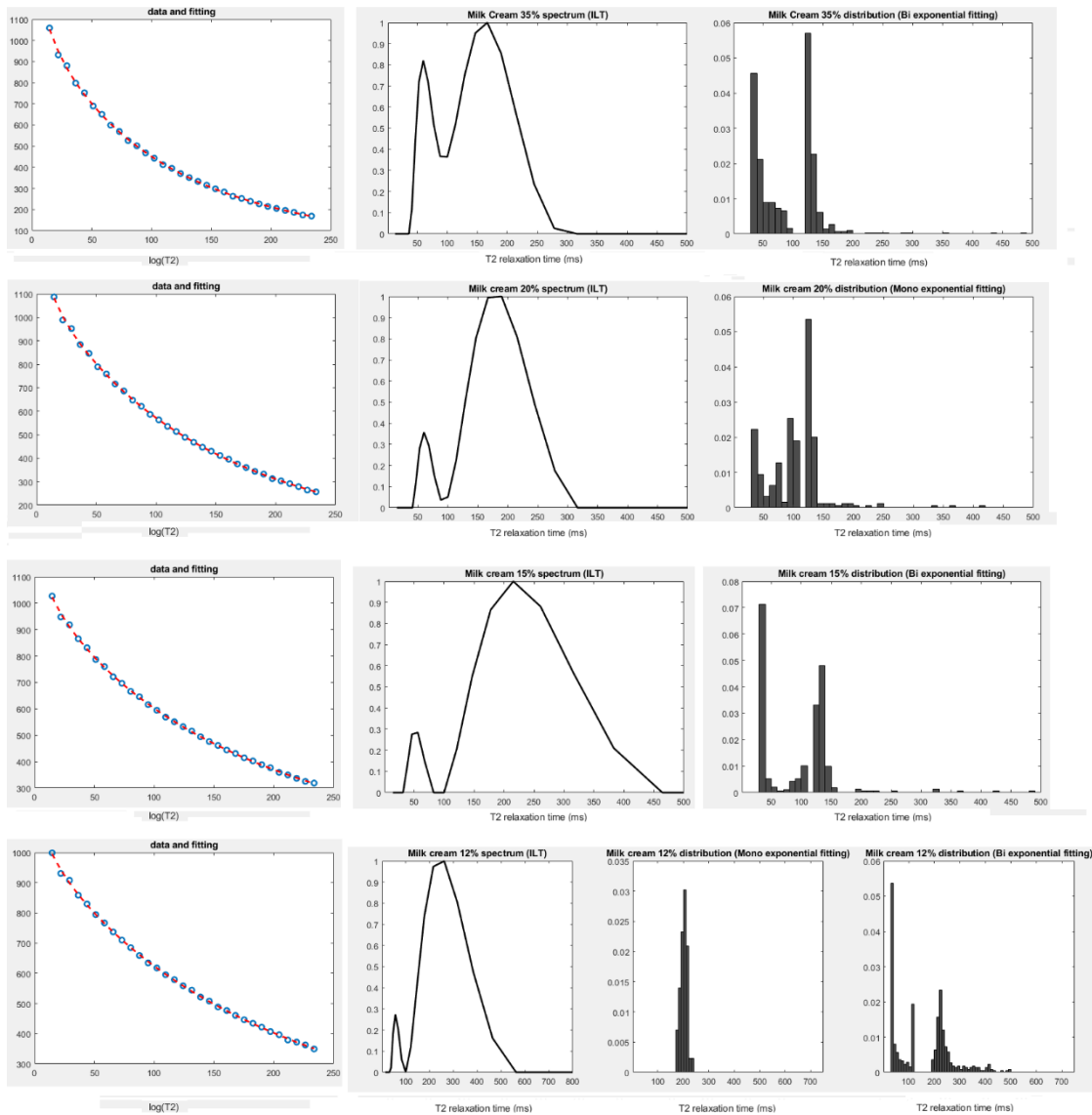


Figure 45 Data Fitting, ILT distribution and Mexp results for milk creams of different fat fractions

The corresponding mono-exponential distribution is also presented in Fig. 5. Additionally, mixtures of egg whites and yolks (Fig.6) were studied. These mixtures are present in positions 7-9 in Fig. 2 and again, a wider bi-exponential dominance is noticed as the fatty component is increased. In more detail, the sample containing a mixture of one egg white and 3 yolks had mono/bi-exponential voxel dominance ratio of 10/90% while at the other end a mixture of increased aqueous component (three egg whites, one yolk) had a ratio of 40/60%. The mixture of one white and one yolk had 91% mono-exponential dominance. Interestingly, for the mixture of one egg white and three yolks, the ILT method failed to recognize the fat contribution and shows a single distribution while the Mexp method shows 60% bi-exponential behavior. All the aforementioned results are presented in Table 1.

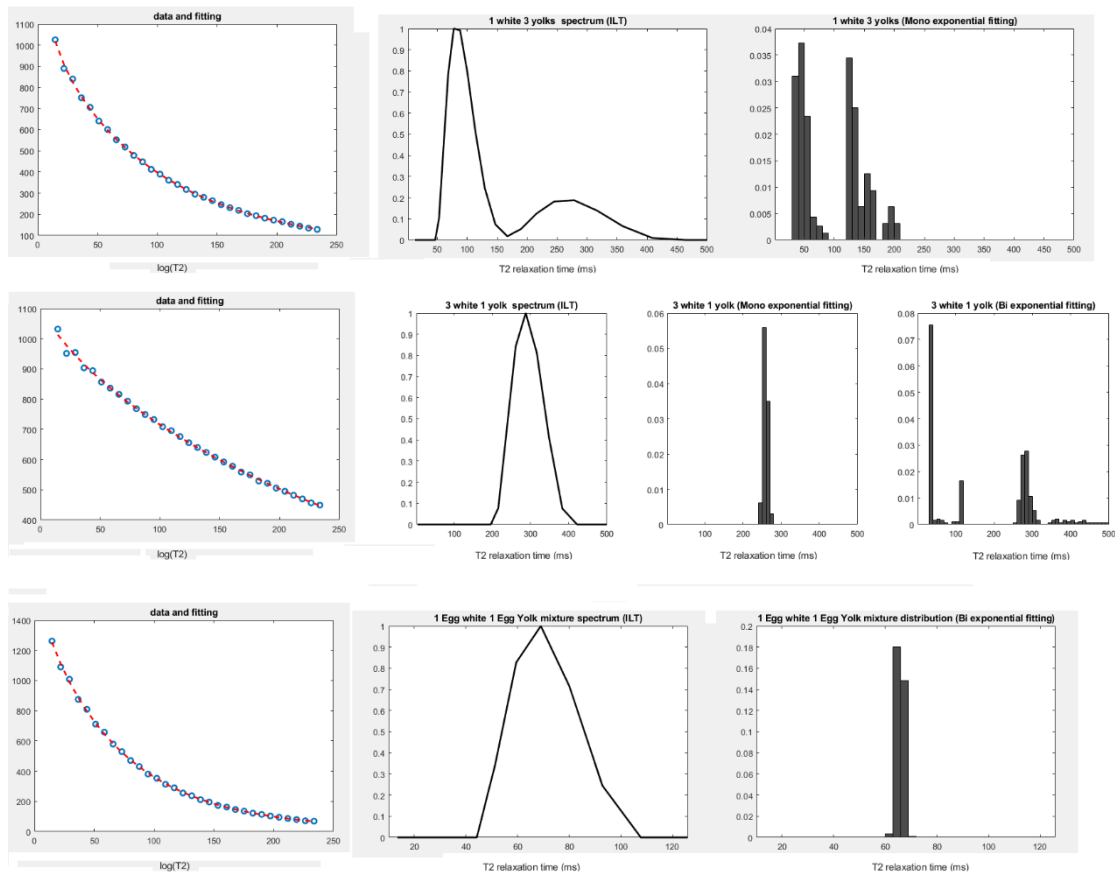


Figure 46 Data fitting, ILT distribution and Mexp results for egg white and yolk mixtures

Patient study

Having verified the sensitivity of Mexp methodology to identify water compartments in samples with known relaxation patterns in the literature (Jones, MacKay and Rutt, 1998; Yahya, Tessier and Fallone, 2011; Mitsouras, Mulkern and Maier, 2016), we proceeded to a patient study with benign and malignant lipomatous tumors based on the proposed Mexp method. For the histopathologically distinct entities described in the patient population the mono/bi exponential classification per pathology was calculated as barplots in Fig. 7. Apart from lipoma all other categories exhibit mixed mono/bi-exponential behavior with different degree of contribution. It is important to note that data come from regions within the tumor excluding macroscopic cystic or necrotic areas identifiable in conventional MRI as this could introduce bias to the results. Voxels used for the analysis were indicative of viable tumor characteristics. Indicatively, Fig. 8 shows voxel by voxel classification for: (a) a benign lipoma of the left shoulder, (b) a well differentiated liposarcoma of the right thigh, (c) a myxoid liposarcoma of the left thigh, (d) a poorly differentiated liposarcoma of the left thigh and (e) a pleomorphic liposarcoma of the left thigh.

Relaxation pattern for lipoma resembles the chosen tissue mimicking sample of corn oil (Constable *et al.*, 1992) presenting more than 99.7% bi exponential behavior. On the basis of strong agreement on the bi-exponential behavior of both methods we took a further step of presenting the lipoma T_2 distributions per patient in Fig. 9. ILT results (left plot Fig. 9) show a

Phantom study

strong qualitative resemblance with results from Mexp method (right plot Fig. 9). Tissue heterogeneity within liposarcomas cannot permit a similar per patient analysis for the rest of the patient cohort. Calculated values for A_i and T_{2i} for all lipomatous tissue subtypes are shown in Table 1.

Phantom Samples	Mono/Biexponent prevalence (%)	$A_1 \pm \text{std}$	$T_{21} \pm \text{std}$	$A_2 \pm \text{std}$	$T_{22} \pm \text{std}$
Acetone	98/2	532.982 ± 20.1	2231.083 ± 206		
DD water	97/3	893.132 ± 24.4	1716.445 ± 240		
Milk Cream 35%	0/100	519.836 ± 218	41.269 ± 16.163	794.440 ± 236	$240.320 \pm 55.$
Milk Cream 20%	5/95	339.084 ± 246	44.615 ± 24.823	871.756 ± 261	$304.354 \pm 66.$
Milk Cream 15%	10/90	409.935 ± 352	46.750 ± 26.811	830.871 ± 374	$411.115 \pm 48.$
Milk Cream 12%	15/85	1012.082 ± 47	200.652 ± 13.08		
		313.229 ± 208	57.604 ± 35.135	764.865 ± 225	$349.630 \pm 64.$
1 White 3 Yolks	10/90	1115.686 ± 41	91.433 ± 1.993		
		518.258 ± 141	46.127 ± 10.934	674.145 ± 152	$177.276 \pm 23.$
3 White 1 Yolk	40/60	1021.354 ± 41	258.039 ± 5.86		
		169.016 ± 115	47.971 ± 33.780	910.839 ± 154	$317.543 \pm 50.$
1 White 1 Yolk	91/9	1511.349 ± 71	65.818 ± 1.159		
1 Yolk	0/100	$980.825 \pm 36.$	30.0 ± 1.137	43.578 ± 15.06	$236.501 \pm 20.$
Corn Oil	0/100	666.831 ± 183	40.416 ± 12.035	$1044.111 \pm 10.$	$193.364 \pm 33.$
Adipose Tissue	0/100	$504.498 \pm 69.$	45.690 ± 13.943	751.916 ± 147	$191.284 \pm 21.$
Patient study					
Tissue Type	Mono/Biexponent prevalence (%)	$A_1 \pm \text{std}$	$T_{21} \pm \text{std}$	$A_2 \pm \text{std}$	$T_{22} \pm \text{std}$
Lipoma	0.3 % mono	-	-	-	-
	99.7 % bi	319.943 ± 183	41.807 ± 13.327	630.097 ± 195	$205.197 \pm 64.$
Well differentiated liposarcoma	17.7 % mono	205.911 ± 95.8	322.761 ± 139.8	-	-
	82.3 % bi	279.234 ± 160	42.926 ± 19.644	757.961 ± 260	220.782 ± 112
Myxoid liposarcoma	47.8 % mono	910.357 ± 134	439.581 ± 79.24	-	-
	52.2 % bi	237.412 ± 129	60.801 ± 37.310	793.358 ± 190	469.580 ± 148
Poorly differentiated liposarcoma	53 % mono	469.685 ± 237	152.166 ± 102.1	-	-
	47 % bi	242.496 ± 156	48.166 ± 25.063	525.902 ± 378	223.732 ± 121
Pleomorphic liposarcoma	25 % mono	583.505 ± 99.0	441.506 ± 154.7	-	-
	75 % bi	285.210 ± 95.1	38.531 ± 19.235	678.743 ± 109	263.641 ± 153

Table 6

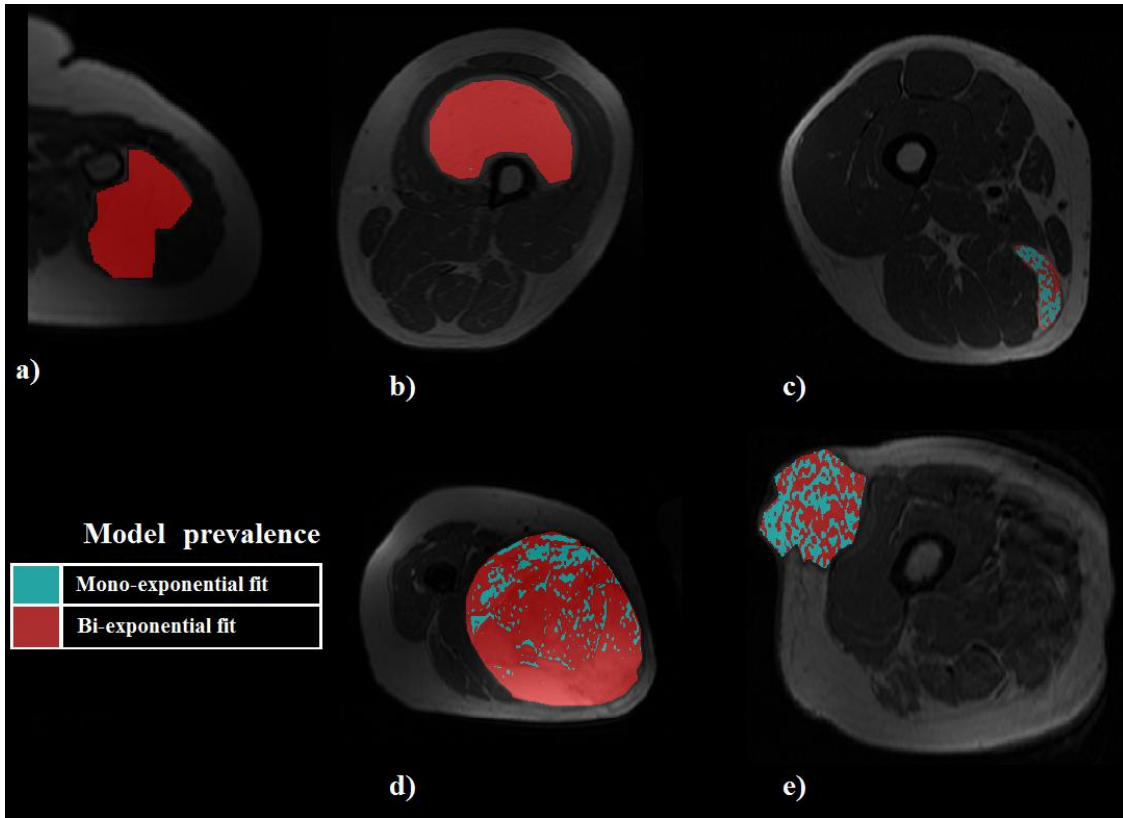


Figure 47 Mexp based voxel by voxel classification indicatively for tissues of variable degree of malignancy

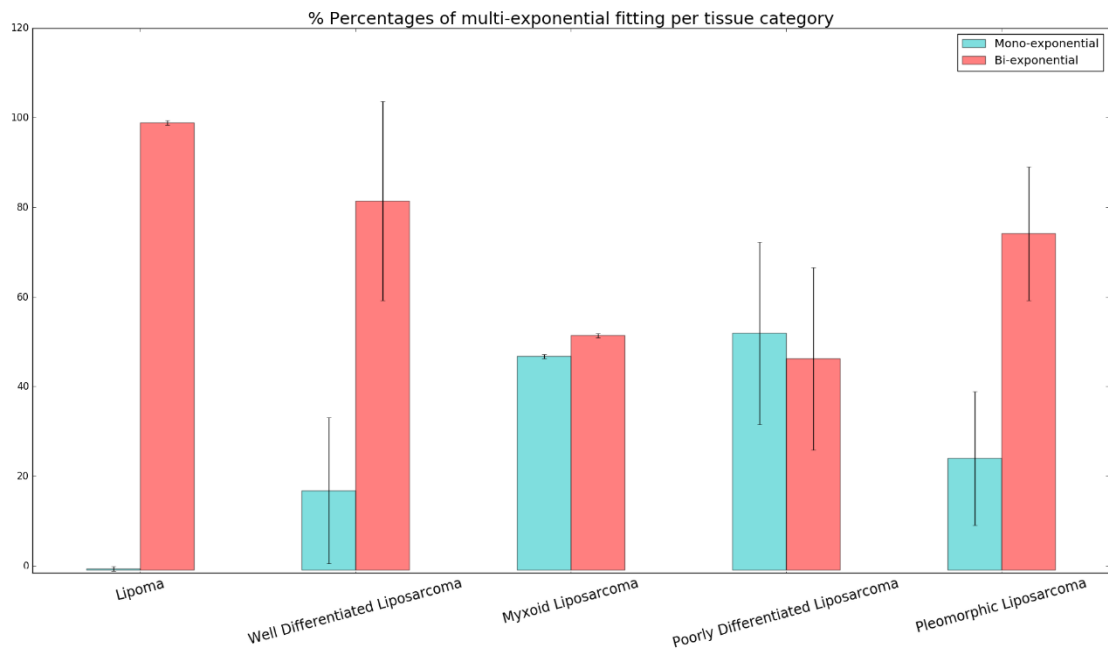


Figure 48 Tissue Classification based on Mexp method

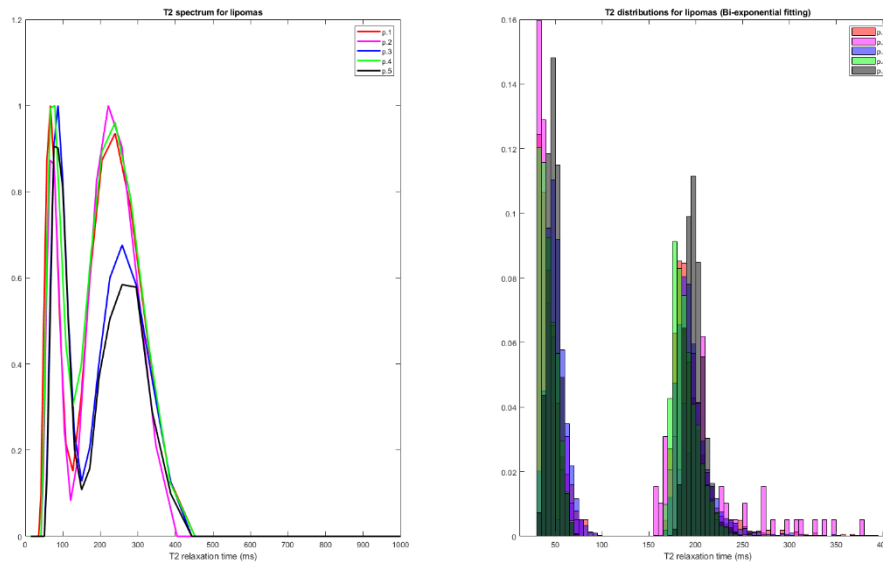


Figure 49: T2 distribution and corresponding M_{exp} results for five lipomas

6.4 Discussion

The observation of Damadian that cancerous tissue has longer T_2 times than normal tissue (Damadian, 1971) has been the cornerstone of clinical MRI. The first proof of concept for tissue characterization from multi-exponential T_2 relaxometry was published from Vasilescu in 1978 (Vasilescu *et al.*, 1978), reporting three micro-anatomically distinct compartments in the excised sciatic frog nerve reasoned to be water closely associated with proteins and phospholipids. This study clearly suggested that it is possible apart from extracting a tissue specific T_2 value, to probe tissue composition at a microscopic level. Assuming slow or minimal exchange between water compartments, the number of distinct exponential decays corresponds to the number of water compartments in tissue with different relaxation rates, with signal intensity amplitude being a measure of its anatomical size. Transverse relaxation (T_2) relaxation rate (spin dephasing) is a measure of the mobility of water molecules in tissue, which in turn is indicative of the microenvironment of tissue and the presence of motion confounding structures or other macromolecules that bind to the water dipole molecule.

The study of myelin in the brain and muscle have been the focus and the driving force for expanding multiexponential T_2 methodology armamentarium. Concerning the former, three distinct water compartments have been identified, assigned to motion-restricted water particles between the lipid layers of the myelin sheath ($10 \text{ ms} < T_2 < 40 \text{ ms}$), more freely moving water in the intra- and extracellular spaces ($80 \text{ ms} < T_2 < 100 \text{ ms}$) and CSF ($T_2 > 2 \text{ s}$) (Mackay *et al.*, 1994; Whittall *et al.*, 1997; Alonso-Ortiz, Levesque and Pike, 2015). For the latter, studies on muscle tissue have identified up to four water compartments with T_2 values ranging from $<5 \text{ ms}$ to $T_2 > 400 \text{ ms}$, assigned to extracellular (slow exponential extracellular component with $T_2 > 0.4 \text{ s}$, intermyofibrillar ($T_2 \approx 0.15 \text{ s}$), myofibrillar ($0.03 \text{ s} < T_2 < 0.06 \text{ s}$) and a rapid component ($T_2 < 0.03 \text{ s}$) residing at the vicinity of the macromolecules (Saab *et al.*, 2001; Kimura *et al.*, 2005).

In the specific domain of lipid or connective tissue, T_2 relaxometry has been subject of a limited number of publications (Torriani *et al.*, 2014) (Chaudhari *et al.*, 2017). However, reported results from MR Spectroscopy have shown evidence that the study of fat content allows for adipose tissue classification on the basis of variable abundance of distinct fat moieties with each one having a different T_2 rate in benign lipomatous tissue and liposarcomas (Millis *et al.*, 1999; Chen *et al.*, 2001). Unlike water that resonates at a single frequency, fat spectrum is more complex with a number of resolvable peaks depending on the imaging hardware and the theoretical assumptions (Simchick *et al.*, 2018). MR signal from fat comes mainly from the triglyceride molecules in fatty tissue, while other compounds such as cholesterol and free fatty acids contribute insignificantly in comparison to triglycerides. Fatty acids in triglycerides have chain lengths ranging between 14 and 18 while they have 0-2 double bonds (Hodson, Skeaff and Fielding, 2008) depending on diet or metabolic activity of adipose tissue depot (Lundbom *et al.*, 2013). Adipose tissue differentiation based on NMR has shown a marked fall in visible triglyceride levels associated with a significant increase in phosphatidylcholine levels, with the latter serving as a measure of cell membrane turnover and cell division. Low grade liposarcoma was found to have similar triglyceride content to normal fat (25). Notwithstanding the significance of these results, in vivo MR spectroscopy is not readily available and moreover has poor spatial resolution and has high software, timing and shimming demands, as opposed to T_2 relaxometry.

Each peak in the fat spectrum has a distinct T_2 relaxation time ranging from 30 to 70 ms at 1.5T (Hamilton *et al.*, 2011) and, at a voxel level, the measured T_2 is the averaged sum of all fat peaks present in the imaging volume. Longer T_2 are conjectured to originate from methyl-H in mobile triglycerides originating from cytoplasmic lipid droplets, most abundant in highly differentiated liposarcomas, while, on the other hand, shorter T_2 components come from rotationally hindered and perhaps intracellularly bound protons of pleomorphic or dedifferentiated liposarcomas. Myxoid neoplasms exhibit higher water content and low

triglyceride and increased levels of phospholipids (Millis *et al.*, 1999). Apart from lipid content, other microscopic structures contribute to the decay signal at a voxel level, such as fibrous or myxoid tissue hosted within malignant neoplasms.

To this end, our study focused on T_2 relaxometry of fat samples for validation and was extended to human tissue in order to describe the relaxation patterns of complex microenvironment within tissue of lipomatous origin. Phantom results were obtained and looked in comparison to the well-established ILT method for obtaining T_2 spectrum, in order to verify qualitative agreement in the distribution shape and the number of distinct T_2 compartments. Indeed, results from the phantom study verified that the algorithm can identify the most appropriate exponential fitting model as samples of known decay pattern were attributed to the theoretically expected model. In more detail, double distilled water or acetone was described by the mono-exponential model, which is considered as the most accurate, and corresponds to the free water compartment in tissue. Corn oil was used as it closely matches the spectrum and longitudinal relaxation times of subcutaneous abdominal fat (Kuroda *et al.*, 1998) and was best described by an exclusively bi-exponential model. Dairy cream of variable fat content were used as they provide a mixed aqueous and fatty environment with measurable contribution from each component (Jones, MacKay and Rutt, 1998). Egg white exhibits two-component decay with intermediate and long T_2 times. Meanwhile, yolk is generally best characterized with triexponential decays, with short, intermediate and very long T_2 decay times. Experimental results have shown that the intermediate component of yolk could be attributed to lipids (Mitsouras, Mulkern and Maier, 2016).

Based on the above results the same numerical procedure was applied to lipomatous tumors and also to reference ROIs from normal tissue (normal adipose tissue). Subcutaneous fat exhibited very similar behavior to corn oil while, from the clinical aspect, resembles to well-differentiated fat. However, the latter also exhibits a small percentage of voxels with mono exponential dominance which in turn is present in all studied tumors of high histological grade. In detail, neoplasms of higher degree of malignancy have a significant presence of mono exponential voxels (Fig. 7). This diverse distribution can be a result of a heterogeneous tumor microenvironment. Moreover, we separately examined and observed shortened T_2 times and mono-exponential behavior in the areas of necrosis identified by histopathology, potentially as a result of macromolecular compounds from the cells released into the extracellular space and binding to free water molecules (Liu *et al.*, 2016).

One of the major constraints inherent in T_2 relaxometry is acquisitions with adequate SNR to ensure accurate and repeatable measurements. Compromised SNR results in peak broadening and confounds accurate multi exponential fitting. In an experimental simulation of a three pool

model an SNR of the order of 500 was reported for accurate detection (>80% of samples) of three exponential curves, while an SNR of 150 detected only 30% (Andrews *et al.*, 2005). However such SNR levels are very challenging in a clinical setting, in terms of spatially localized signal and acquisition timing. In our study SNR ranged from 120-80, depending on tissue type, with the most signal abundant pathology being myxoid liposarcoma and lipomatous masses at the other end. To this end, Mexp results were used quantitatively, assessing the T_2 distribution shape rather than a quantitative estimation of each water pool size.

Additionally, the first (effective) TE is limiting the minimum T_2 rate feasible to be detected by the proposed method and thus one cannot exclude a third compartment in the low T_2 range that cannot be detected with the described sequence parameters. A very short T_2 component could be attributed to water protons motionally restricted, probably strongly bound to macromolecules or physically constrained within cell structures. Here, we set the minimum detectable T_2 at 20 ms for a first –effectively, since the signal from TE=13.4 was ignored–echo at 26.8 ms.

Another important aspect to be noted is that the problem of decomposing the total signal to more than two discrete exponentials becomes non trivial (Whittall and MacKay, 1989) because of the large number of the parameters for optimization (i.e. for N= 3, max. number of parameters=6). Non overlapping bounds had to be set between models as the fitting algorithm is unable to accurately assign components of the same T2 value to different components. The reason for this constrain is that in case of same T2i values the optimization process favors to adapt the weights (Ai in Eq. (1)) rather than the exponential term.

The limited number of samples does not allow for classification of the various types of liposarcomas, but yet it is a feasibility study showing the complex pattern of relaxation among different tissue types that can be sensitive to the chemical and physical environment surrounding water hydrogen protons. The pure bi-exponential behavior characterizing healthy adipose tissue and benign lipoma differs for the malignant tissues of lipomatous origin, where a mono-exponentially decaying component contributes to the signal time intensity curve of CPMG/PHAPS T_2 relaxometry data.

Chapter 7 Conclusion

Considering the importance of accurate pre-operative characterization of soft tissue masses for all subsequent medical procedures we set an advanced oncologic MR imaging protocol comprised of multi-b DWI, high resolution DCE, multi-echo GE and SE T2 relaxometry sequences among other conventional imaging series. During the data acquisition period, we focused our methods to the imaging of benign and malignant tumors of adipocytic origin, as this kind of data vastly outnumbered any other soft tissue tumor subtype and thus would present the most statistically powerful result. Quantitative MR methods were presented in order to extract the clinically relevant information from the proposed protocol according to the best practices as proposed by recent literature. The overall scope of this work is to maximize the impact of pre-operative imaging methods for soft tissue tumors and to present quantitative methods that can be deployed in other fields of oncology, or other medical fields.

The conclusions drawn from this study at the three different stages can be summarized below:

7.1 DWI – DCE imaging sequences

A free correlation study among all DCE and DWI derived pairs of parameters, showed a linear relationship between f-IVIM and vp-GCTT in patients with soft tissue sarcomas. DCE in conjunction with DWI MRI can provide useful information on sites of aggressive characteristics both in terms of cellularity and vascularity. Localization of sites combining dense cell density and increased vascular permeability increases confidence about identification of the most malignant areas within a heterogeneous large neoplasm. This non-invasive mapping can be a useful tool for guiding the pre-operative biopsy and for overall treatment planning.

7.2 T2/T2* relaxometry sequences

The novel biomarker SCr can be introduced as a quantitative adjunct for radiological assessment of lipomatous tissue type and grade with minimal software and time prerequisites. The amount of spin coupling related signal loss differs among entities of different degree of cell differentiation. Clinical implications of this MRI technique may be biopsy guidance in heterogeneous lipomatous tumors to assure for harvesting tissue with the highest malignancy

grade and non-invasive preoperative diagnosis of tumor type and grade, which is essential for adequate treatment planning.

7.3 T2 relaxometry sequence - Multi exponential methods

A proposed Mexp method with no a priori assumptions on the number of components can be used alternatively to the well-established ILT method to identify the number of distinct T2 relaxing compartments. Agreement between the two methods suggests the possible use of MExp to provide valuable tissue specific information stemming from a microscopic tissue scale as an adjunct to conventional radiological assessment of the complex tissue microenvironment. It has the added advantage of producing pixel based parametric maps rather than ROI based distributions as resulting from the ILT method. The number of fast/slow relaxing components is indicative of tissue composition and varies among adipocytic neoplasms of different degree of malignancy.

References

(No Title) (no date). Available at: http://myweb.rz.uni-augsburg.de/~eckern/adp/history/einstein-papers/1905_17_549-560.pdf (Accessed: 16 December 2019).

Alonso-Ortiz, E., Levesque, I. R. and Pike, G. B. (2015) 'MRI-based myelin water imaging: A technical review', *Magnetic Resonance in Medicine*. John Wiley & Sons, Ltd, 73(1), pp. 70–81. doi: 10.1002/mrm.25198.

Andrews, T. *et al.* (2005) 'Testing the three-pool white matter model adapted for use with T2 relaxometry', *Magnetic Resonance in Medicine*, 54(2), pp. 449–454. doi: 10.1002/mrm.20599.

Le Bihan, Denis, Eric Breton, D. L. (1988) 'Separation of Diffusion and Perfusion in Intravoxel Incoherent Motion MR Imaging', *Radiology*, 168, pp. 497–505.

Brix, Gunnar *et al.* (2012) 'On impulse response functions computed from dynamic contrast-enhanced image data by algebraic deconvolution and compartmental modeling', *Physica Medica*, 28, pp. 119–128. doi: 10.1016/j.ejmp.2011.03.004.

Callegaro, D. *et al.* (2018) 'Impact of perioperative chemotherapy and radiotherapy in patients with primary extremity soft tissue sarcoma: retrospective analysis across major histological subtypes and major reference centres', *European Journal of Cancer*, 105, pp. 19–27. doi: 10.1016/j.ejca.2018.09.028.

Casali, P. G. *et al.* (2018) 'Soft tissue and visceral sarcomas: ESMO–EURACAN Clinical Practice Guidelines for diagnosis, treatment and follow-up[†]', *Annals of Oncology*, 29(Supplement_4), pp. iv51–iv67. doi: 10.1093/annonc/mdy096.

Chaland, B. *et al.* (2019) '1H nuclear magnetic resonance relaxometric characterization of fat and water states in soft and hard cheese', *Journal of Dairy Research*, 67, pp. 609–618. doi: 10.1017/S0022029900004398.

Chaudhari, A. S. *et al.* (2017) 'Imaging and T2 relaxometry of short-T2 connective tissues in the knee using ultrashort echo-time double-echo steady-state (UTEDESS).', *Magnetic resonance in medicine*. NIH Public Access, 78(6), pp. 2136–2148. doi: 10.1002/mrm.26577.

Chen, J.-H. *et al.* (2001) 'Biochemical Analysis Using High-Resolution Magic Angle Spinning

NMR Spectroscopy Distinguishes Lipoma-Like Well-Differentiated Liposarcoma from Normal Fat'. doi: 10.1021/ja016182u.

Coindre, J. M., Pédeutour, F. and Aurias, A. (2010) 'Well-differentiated and dedifferentiated liposarcomas', *Virchows Archiv*. Springer Verlag, pp. 167–179. doi: 10.1007/s00428-009-0815-x.

Constable, R. T. *et al.* (1992) 'Factors influencing contrast in fast spin-echo MR imaging', *Magnetic Resonance Imaging*. Elsevier, 10(4), pp. 497–511. doi: 10.1016/0730-725X(92)90001-G.

Damadian, R. (1971) 'Tumor Detection by Nuclear Magnetic Resonance', *Science*, 171(3976), pp. 1151–1153. doi: 10.1126/science.171.3976.1151.

Doyle, L. A. (2014) 'Sarcoma classification: an update based on the 2013 World Health Organization Classification of Tumors of Soft Tissue and Bone.', *Cancer*, 120(12), pp. 1763–74. doi: 10.1002/cncr.28657.

Federau, C. *et al.* (2014) 'Measuring brain perfusion with intravoxel incoherent motion (IVIM): Initial clinical experience', *Journal of Magnetic Resonance Imaging*, 39(3), pp. 624–632. doi: 10.1002/jmri.24195.

Fisher, M. and Sotak, C. H. (no date) *Commentary-Diffusion-Weighted MR Imaging and Ischemic Stroke*.

Fletcher, C. D. *et al.* (1996) 'Correlation between clinicopathological features and karyotype in lipomatous tumors. A report of 178 cases from the Chromosomes and Morphology (CHAMP) Collaborative Study Group.', *The American journal of pathology*, 148(2), pp. 623–30. Available at: <http://www.ncbi.nlm.nih.gov/pubmed/8579124> (Accessed: 24 September 2019).

Fransson, A. *et al.* (1993a) 'Properties of the PHase-Alternating Phase-Shift (PHAPS) multiple spin-echo protocol in MRI: A study of the effects of imperfect RF pulses', *Magnetic Resonance Imaging*. Elsevier, 11(6), pp. 771–784. doi: 10.1016/0730-725X(93)90195-J.

Fransson, A. *et al.* (1993b) 'Properties of the PHase-Alternating Phase-Shift (PHAPS) multiple spin-echo protocol in MRI: A study of the effects of imperfect RF pulses', *Magnetic Resonance Imaging*. Elsevier, 11(6), pp. 771–784. doi: 10.1016/0730-725X(93)90195-J.

Gupta, P. *et al.* (2016) 'Spectrum of Fat-containing Soft- Tissue Masses at MR Imaging: The Common, the Uncommon, the Characteristic, and the Some- times Confusing'. doi:

10.1148/rg.2016150133.

Hahn, E. L. and Maxwell, D. E. (1952) 'Spin Echo Measurements of Nuclear Spin Coupling in Molecules', *Physical Review*, 88(5), pp. 1070–1084. doi: 10.1103/PhysRev.88.1070.

Hamilton, G. *et al.* (2011) 'MR properties of brown and white adipose tissues.', *Journal of magnetic resonance imaging: JMRI*. NIH Public Access, 34(2), pp. 468–73. doi: 10.1002/jmri.22623.

Hennig, J. (1991) 'Echoes—how to generate, recognize, use or avoid them in MR-imaging sequences. Part I: Fundamental and not so fundamental properties of spin echoes', *Concepts in Magnetic Resonance*. John Wiley & Sons, Ltd, 3(3), pp. 125–143. doi: 10.1002/cmr.1820030302.

Henze, J. and Bauer, S. (2013) 'Liposarcomas', *Hematology/Oncology Clinics of North America*, pp. 939–955. doi: 10.1016/j.hoc.2013.07.010.

Hodson, L., Skeaff, C. M. and Fielding, B. A. (2008) 'Fatty acid composition of adipose tissue and blood in humans and its use as a biomarker of dietary intake', *Progress in Lipid Research*, 47(5), pp. 348–380. doi: 10.1016/j.plipres.2008.03.003.

Jones, C., MacKay, A. and Rutt, B. (1998) 'Bi-Exponential T2 Decay in Dairy Cream Phantoms', *Magnetic Resonance Imaging*. Elsevier, 16(1), pp. 83–85. doi: 10.1016/S0730-725X(97)00250-6.

Kim, H. S. *et al.* (2014) 'Histogram analysis of intravoxel incoherent motion for differentiating recurrent tumor from treatment effect in patients with glioblastoma: initial clinical experience.', *AJNR. American journal of neuroradiology*. American Journal of Neuroradiology, 35(3), pp. 490–7. doi: 10.3174/ajnr.A3719.

Kimura, M. *et al.* (2005) 'Differential osmotic behavior of water components in living skeletal muscle resolved by 1H-NMR', *Biophysical Journal*. doi: 10.1529/biophysj.105.059717.

Kuroda, K. *et al.* (1998) 'Optimization of chemical shift selective suppression of fat', *Magnetic Resonance in Medicine*. John Wiley & Sons, Ltd, 40(4), pp. 505–510. doi: 10.1002/mrm.1910400402.

Kwee, T. C. *et al.* (2010) 'Comparison of apparent diffusion coefficients and distributed diffusion coefficients in high-grade gliomas.', *Journal of magnetic resonance imaging: JMRI*. NIH Public Access, 31(3), pp. 531–7. doi: 10.1002/jmri.22070.

- Lester, S. C. (2010) *Manual of surgical pathology*. Saunders/Elsevier.
- Li, X. *et al.* (2016) 'Relative sensitivities of DCE-MRI pharmacokinetic parameters to arterial input function (AIF) scaling.', *Journal of magnetic resonance (San Diego, Calif. : 1997)*. NIH Public Access, 269, pp. 104–112. doi: 10.1016/j.jmr.2016.05.018.
- Litjens, G. J. S. *et al.* (2010) 'Pharmacokinetic models in clinical practice: What model to use for DCE-MRI of the breast?', in *2010 IEEE International Symposium on Biomedical Imaging: From Nano to Macro*. IEEE, pp. 185–188. doi: 10.1109/ISBI.2010.5490382.
- Liu, L. *et al.* (2016) 'Changes of T2 Relaxation Time From Neoadjuvant Chemotherapy in Breast Cancer Lesions.', *Iranian journal of radiology : a quarterly journal published by the Iranian Radiological Society*. Kowsar Medical Institute, 13(3), p. e24014. doi: 10.5812/iranjradiol.24014.
- Loskutov, V. and Zhakov, S. (2016) 'Dependence of the liquid transverse relaxation time T2 in porous media on fluid flow velocity', *International Journal of Heat and Mass Transfer*. Pergamon, 101, pp. 692–698. doi: 10.1016/J.IJHEATMASSTRANSFER.2016.05.057.
- Löwenthal, D. *et al.* (2013) 'Differentiation of myxoid liposarcoma by magnetic resonance imaging: A histopathologic correlation', *Acta Radiologica*. SAGE Publications Ltd, 55(8), pp. 952–960. doi: 10.1177/0284185113508114.
- Lundbom, J. *et al.* (2013) 'Deep subcutaneous adipose tissue is more saturated than superficial subcutaneous adipose tissue', *International Journal of Obesity*, 37(4), pp. 620–622. doi: 10.1038/ijo.2012.72.
- Mackay, A. *et al.* (1994) 'In vivo visualization of myelin water in brain by magnetic resonance', *Magnetic Resonance in Medicine*. John Wiley & Sons, Ltd, 31(6), pp. 673–677. doi: 10.1002/mrm.1910310614.
- Majumdar, S. *et al.* (1986) 'Errors in the measurements of T2 using multiple-echo MRI techniques. I. Effects of radiofrequency pulse imperfections', *Magnetic Resonance in Medicine*. John Wiley & Sons, Ltd, 3(3), pp. 397–417. doi: 10.1002/mrm.1910030305.
- Manikis, G. C. *et al.* (2016) 'Diffusion Modelling Tool (DMT) for the analysis of Diffusion Weighted Imaging (DWI) Magnetic Resonance Imaging (MRI) data', in *Proceedings of the 33rd Computer Graphics International on - CGI '16*. New York, New York, USA: ACM Press, pp. 97–100. doi: 10.1145/2949035.2949060.

MANKIN, H. J., MANKIN, C. J. and SIMON, M. A. (1996) 'The Hazards of the Biopsy, Revisited. For the Members of the Musculoskeletal Tumor Society*', *The Journal of Bone & Joint Surgery*, 78(5), pp. 656–63. doi: 10.2106/00004623-199605000-00004.

Maris, T. G. *et al.* (2016) '3D polymer gel MRI dosimetry using a 2D haste, A 2D TSE AND A 2D SE multi echo (ME) T2 relaxometric sequences: Comparison of dosimetric results', *Physica Medica*. Elsevier, 32, pp. 238–239. doi: 10.1016/J.EJMP.2016.07.498.

Mavrogenis, A. F. *et al.* (2011) 'Atypical lipomatous tumors/well-differentiated liposarcomas: Clinical outcome of 67 patients', *Orthopedics*, 34(12). doi: 10.3928/01477447-20111021-11.

Milford, D. *et al.* (2015) 'Mono-Exponential Fitting in T2-Relaxometry: Relevance of Offset and First Echo', *PLOS ONE*. Edited by X. Fan. Public Library of Science, 10(12), p. e0145255. doi: 10.1371/journal.pone.0145255.

Millis, K. *et al.* (1999) *Classification of Human Liposarcoma and Lipoma Using Ex Vivo Proton NMR Spectroscopy, Magn Reson Med.* Available at: <https://onlinelibrary.wiley.com/doi/pdf/10.1002/%28SICI%291522-2594%28199902%2941%3A2%3C257%3A%3AAID-MRM8%3E3.0.CO%3B2-N> (Accessed: 19 February 2019).

Mitsouras, D., Mulkern, R. V. and Maier, S. E. (2016) 'Multicomponent T₂ relaxation studies of the avian egg', *Magnetic Resonance in Medicine*. John Wiley & Sons, Ltd, 75(5), pp. 2156–2164. doi: 10.1002/mrm.25762.

Murphey, M. D., Arcara, L. K. and Fanburg-Smith, J. (2005) 'From the archives of the AFIP: Imaging of musculoskeletal liposarcoma with radiologic-pathologic correlation', *Radiographics*, pp. 1371–1395. doi: 10.1148/rg.255055106.

Ng, C. S. *et al.* (2015) 'Dependence of DCE-MRI biomarker values on analysis algorithm.', *PloS one*. Public Library of Science, 10(7), p. e0130168. doi: 10.1371/journal.pone.0130168.

Nikiforaki, K. *et al.* (2018) '[OA046] Visualizing sites of increased cellularity and high permeability in soft tissue sarcomas', *Physica Medica*. Elsevier, 52, p. 19. doi: 10.1016/J.EJMP.2018.06.118.

Nishida, J. *et al.* (2007) 'Imaging characteristics of deep-seated lipomatous tumors: intramuscular lipoma, intermuscular lipoma, and lipoma-like liposarcoma', *Journal of Orthopaedic Science*. Elsevier, 12(6), pp. 533–541. doi: 10.1007/S00776-007-1177-3.

Pai, V. B. *et al.* (2015) 'Myxoid mesenchymal neoplasm presenting as massive arm and chest wall oedema with pleural effusion', *ecancermedicalscience*. Cancer Intelligence, 9. doi: 10.3332/ecancer.2015.590.

Pan, M., Yang, X. and Tang, J. (2012) 'Research on Interpolation Methods in Medical Image Processing', *Journal of Medical Systems*. Springer US, 36(2), pp. 777–807. doi: 10.1007/s10916-010-9544-6.

Saab, G. *et al.* (2001) 'Two-dimensional time correlation relaxometry of skeletal muscle in vivo at 3 Tesla', *Magnetic Resonance in Medicine*. John Wiley & Sons, Ltd, 46(6), pp. 1093–1098. doi: 10.1002/mrm.1304.

Santos, P. M. *et al.* (2017) 'Non-Invasive Detection of Adulterated Olive Oil in Full Bottles Using Time-Domain NMR Relaxometry', *Article J. Braz. Chem. Soc*, 28(2), pp. 385–390. doi: 10.5935/0103-5053.20160188.

Schabel, M. C. (2012) 'A unified impulse response model for DCE-MRI.', *Magnetic resonance in medicine*, 68(5), pp. 1632–46. doi: 10.1002/mrm.24162.

Simchick, G. *et al.* (2018) 'Fat spectral modeling on triglyceride composition quantification using chemical shift encoded magnetic resonance imaging', *Magnetic Resonance Imaging*. Elsevier, 52, pp. 84–93. doi: 10.1016/J.MRI.2018.06.012.

Singer, S. *et al.* (1997) 'Correlation of lipid content and composition with liposarcoma histology and grade', *Annals of Surgical Oncology*, 4(7), pp. 557–563. doi: 10.1007/BF02305536.

St Lawrence, K. S. and Lee, T.-Y. (no date) 'An Adiabatic Approximation to the Tissue Homogeneity Model for Water Exchange in the Brain: I. Theoretical Derivation', *Journal of Cerebral Blood Flow and Metabolism*, 18, pp. 1365–1377.

Suo, S. *et al.* (2015) 'Intravoxel incoherent motion diffusion-weighted MR imaging of breast cancer at 3.0 tesla: Comparison of different curve-fitting methods.', *Journal of magnetic resonance imaging : JMRI*, 42(2), pp. 362–70. doi: 10.1002/jmri.24799.

Taheri, S. *et al.* (2011) 'Quantitative measurement of blood-brain barrier permeability in human using dynamic contrast-enhanced MRI with fast T1 mapping.', *Magnetic resonance in medicine*. NIH Public Access, 65(4), pp. 1036–42. doi: 10.1002/mrm.22686.

Teniola, O. *et al.* (2018) 'Imaging of liposarcomas for clinicians: Characteristic features and differential considerations', *Journal of Surgical Oncology*. John Wiley and Sons Inc., pp. 1195–

1203. doi: 10.1002/jso.24949.

Tikhonov, A. N. and Arsenin, V. Y. (1977) *Solutions of Ill-posed problems*. W.H.~Winston.

Todd Constable, R., Smith, R. C. and Gore, J. C. (1993) 'Coupled-spin fast spin-echo MR imaging', *Journal of Magnetic Resonance Imaging*, 3(3), pp. 547–552. doi: 10.1002/jmri.1880030319.

Tofts, P. (2003) *Quantitative MRI of the Brain*. John Wiley & Sons Ltd.

Tofts, P. S. (1997) 'Modeling tracer kinetics in dynamic Gd-DTPA MR imaging.', *Journal of magnetic resonance imaging : JMRI*, 7(1), pp. 91–101.

Torriani, M. *et al.* (2014) 'T2 relaxometry of the infrapatellar fat pad after arthroscopic surgery.', *Skeletal radiology*. NIH Public Access, 43(3), pp. 315–21. doi: 10.1007/s00256-013-1791-4.

Vasilescu, V. *et al.* (1978) 'Water compartments in the myelinated nerve. III. Pulsed NMR result', *Experientia*. Birkhäuser-Verlag, 34(11), pp. 1443–1444. doi: 10.1007/BF01932339.

Whittall, K. P. *et al.* (1997) 'In vivo measurement of T2 distributions and water contents in normal human brain', *Magnetic Resonance in Medicine*. John Wiley & Sons, Ltd, 37(1), pp. 34–43. doi: 10.1002/mrm.1910370107.

Whittall, K. P. and MacKay, A. L. (1989) 'Quantitative interpretation of NMR relaxation data', *Journal of Magnetic Resonance (1969)*. Academic Press, 84(1), pp. 134–152. doi: 10.1016/0022-2364(89)90011-5.

'WHO Classification of Soft Tissue Tumours' (2006), 139(9), pp. 35–9. Available at: <http://www.iarc.fr/en/publications/pdfs-online/pat-gen/bb5/bb5-classifsofttissue.pdf> (Accessed: 3 July 2018).

Yahya, A., Tessier, A. G. and Fallone, B. G. (2011) 'Effect of J-coupling on lipid composition determination with localized proton magnetic resonance spectroscopy at 9.4 T', *Journal of Magnetic Resonance Imaging*. Wiley-Blackwell, 34(6), pp. 1388–1396. doi: 10.1002/jmri.22792.



Original paper

T₂, T₂^{*} and spin coupling ratio as biomarkers for the study of lipomatous tumors



Katerina Nikiforaki^{a,b,*}, Georgios C. Manikis^{a,b}, Eleftherios Kontopodis^{a,b}, Eleni Lagoudaki^c, Eelco de Bree^d, Kostas Marias^{a,e}, Apostolos H. Karantanas^{a,b}, Thomas G. Maris^b

^a Computational BioMedicine Laboratory, Institute of Computer Science, Foundation for Research and Technology-Hellas (FORTH), Heraklion, Crete, Greece

^b Department of Radiology, University of Crete, Heraklion, Crete, Greece

^c Department of Pathology, University Hospital of Crete, Heraklion, Crete, Greece

^d Department of Surgical Oncology, University of Crete, Heraklion, Crete, Greece

^e Technological Educational Institute of Crete, Department of Informatics Engineering, Heraklion, Crete, Greece

ARTICLE INFO

Keywords:

MR diagnosis

Tumors/lipomatous

Spin coupling ratio/biomarker

T₂ relaxometry

T₂^{*} relaxometry

ABSTRACT

Background: Subcutaneous fat may have variable signal intensity on T₂w images depending on the choice of imaging parameters. However, fatty components within tumors have a different degree of signal dependence on the acquisition scheme. This study examined the use of T₂, T₂^{*} relaxometry and spin coupling related signal changes (Spin Coupling ratio, SCr) on two different imaging protocols as clinically relevant descriptors of benign and malignant lipomatous tumors.

Materials and methods: 20 patients with benign lipomas or liposarcomas of variable histologic grade were examined at an 1.5 T scanner with Multi Echo Spin Echo (MESE) different echo spacing (ESP) in order to produce bright fat T₂w images (ESP: 13.4 ms, 25 equidistant echoes) and dark fat images (ESP: 26.8 ms with 10 equidistant echoes). T₂^{*} relaxometry acquisition comprises 4 sets of in-opposed echoes (2.4–19.2 ms, ESP: 2.4 ms) Multi Echo Gradient Echo (MEGRE) sequence. All parametric maps were calculated on a pixel basis.

Results: Significant differences of SCr were found for five different types of lipomatous tumors (Pairwise *t*-test with Bonferroni correction): lipomas, well differentiated liposarcomas, myxoid liposarcomas, pleomorphic liposarcomas and poorly differentiated liposarcomas. SCr surpassed the classification performance of T₂ and T₂^{*} relaxometry.

Data conclusion: A novel biomarker based on spin coupling related signal loss, SCr, is indicative of lipomatous tumor histological grading. We concluded that T₂, T₂^{*} and SCr can be used for the classification of fat containing tumors, which may be important for biopsy guidance in heterogeneous masses and treatment planning.

1. Introduction

Fat containing tumors can be benign (lipomas) or malignant (liposarcomas). Liposarcomas which account for approximately 20% of all sarcomas comprise different degrees of malignancy, including low (well differentiated), intermediate (myxoid) and high (pleomorphic, dedifferentiated) [1]. Histologic type and grade is important to predict the clinical behavior of liposarcomas, i.e. rate of growth, possibility to metastasize, risk of recurrence and survival rate.

Preoperative diagnosis of soft tissue tumor type and grade is essential for treatment planning. In the case of a malignant soft tissue tumor (sarcoma) wide excision of the tumor together with a rim of adjacent structures is the surgical treatment of choice to reduce the risk

of involved margins and local recurrence, while in the case of a benign tumor marginal resection is adequate. Marginal resection is preferred where appropriate since it decreases the risk of short-term, functional and cosmetic morbidity, which are frequently observed after wide tumor excision. Moreover, depending on the exact tumor type and grade preoperative radiotherapy or chemotherapy may be indicated.

While MRI is the imaging method of choice for soft tissue tumors, unfortunately as yet reliable preoperative diagnosis is only accomplished by core needle or open biopsy. Since soft tissue tumors may be heterogeneous and the area with the highest malignancy grade determines its biological behavior, it is essential to harvest tissue samples from this site of the tumor. MRI may determine this specific area and consequently be helpful in directing the biopsy, either performed

* Corresponding author.

E-mail address: nikiforakik@gmail.com (K. Nikiforaki).

<https://doi.org/10.1016/j.ejmp.2019.03.023>

Received 15 February 2019; Received in revised form 19 March 2019; Accepted 21 March 2019

Available online 28 March 2019

1120-1797/ © 2019 Associazione Italiana di Fisica Medica. Published by Elsevier Ltd. All rights reserved.

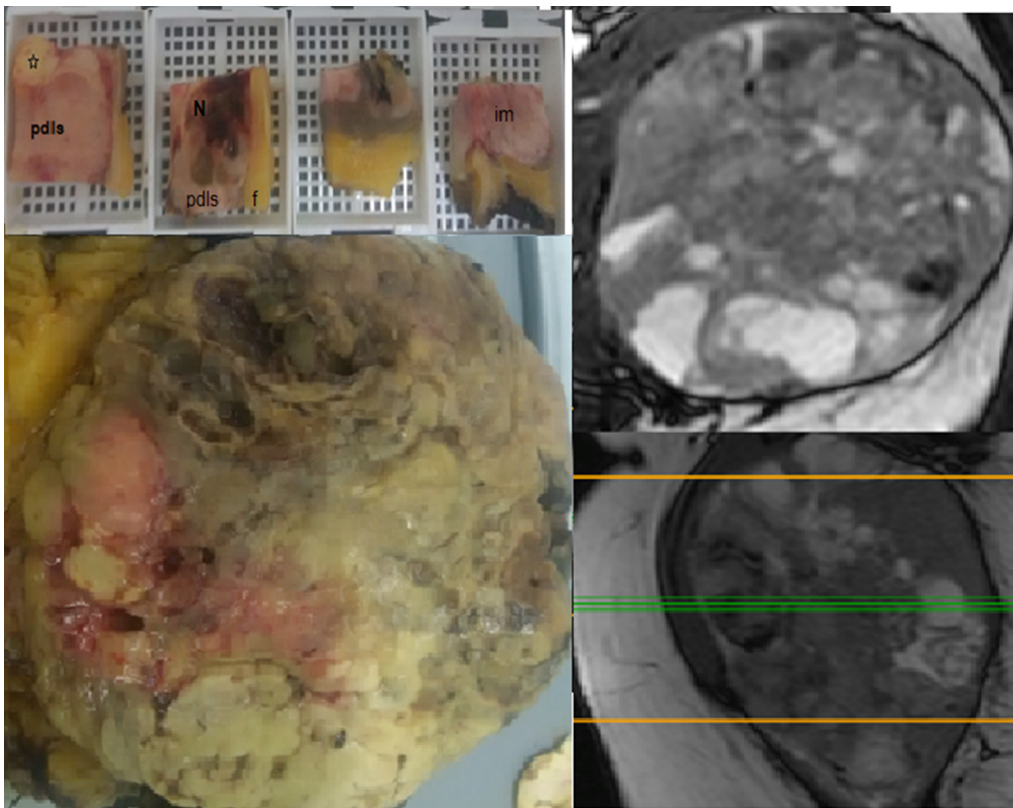


Fig. 1. Surgical specimen (dedifferentiated liposarcoma of the thigh). The central slice was divided into 26 orthogonal sections. Area of well differentiated liposarcoma (asterisk) is adjacent to area of poor differentiation (pdls). Necrotic (N), hemorrhagic areas and fat (f) were identified as well as infiltrated muscle (im). Corresponding axial and coronal T2/T1-w (trueFISP) images are shown on the right.

imaging-guided or by palpation. However, non-invasive achievement of the correct assessment of soft tissue tumor type and grade would avoid the potential complications of a biopsy, such as spillage of tumor cells, wound breakdown with tumor growth through the wound, pain, bleeding, wound infection and patient's discomfort. Moreover, since the vast majority of patients with a soft tissue tumor undergoes nevertheless MRI, additional costs of preoperative biopsy and histological examination may be saved. Hence, it would be a great accomplishment when type and grade of soft tissue tumors, including lipomatous tumors, and their heterogeneous areas can be determined in a non-invasive manner by MRI techniques.

Benign and malignant tumors of lipomatous origin can share a number of overlapping imaging characteristics on conventional MRI. Radiological diagnosis is based on lesion size, depth, presence of enhancing septa, etc. [2,3]. However tissue histopathological sample examination is needed to assess parameters as cell type, cellular atypia, number of mitoses and presence of necrosis for definitive tumor characterization.

However, apart from conventional MRI, quantitative biomarkers derived from an extended protocol can non-invasively offer an insight into tissue that can support radiological diagnosis. In this study we examined 2 widely used biomarkers and we introduce a novel biomarker related to spin coupling (Spin Coupling ratio, SCr).

T2 relaxometry has been a robust and long standing method for tissue or material characterization based on MRI, as T2 relaxation constant can be considered as a definite signature of the inner structure of the imaging object, used not only in medicine but in other fields such as food science, geological studies, radiation dosimetry etc. [4–6]. As opposed to water that resonates at a single frequency, lipid protons give rise to at least 8 distinct resonance peaks [7]. Each lipid spectral peak exhibits a different relaxation rate and consequently different T2 constant [8]. Estimation of T2 depends on the relevant abundance of each peak in the selected region and thus is indicative of the microscopic inner structure of the sample.

Secondly, T2* can enhance the information obtained from standard

T2 relaxometry, by presenting a quantitative metric of local field inhomogeneity which is indicative of the presence of paramagnetic molecules, i.e. blood products, iron rich structures, etc. [9]. The utility of measuring T2* in combination with T2 lies on its ability to correlate well with a number of semantic physiological parameters such as local tissue oxygenation and iron concentration.

Lastly, the concept behind measuring spin coupling signal loss is based mainly on the object of this study, which is fat containing tissue. From the early days of MRI the bright appearance of fat on images with short echo spacing was reported as opposed to other structures of similar T2 relaxation constant and darker appearance [10]. Since this phenomenon is selectively observed on fat, the purpose of this study is to quantitatively evaluate signal changes for lipomatous tumors of different degree of malignancy in order to examine the clinical relevance of a novel biomarker.

Unlike water that resonates at a single frequency, fat has a complex spectrum because of its composition in different triglycerides. At clinical field strengths six distinct spectral peaks are visible at different resonant frequencies (5.3, 4.2, 2.7, 2.1, 1.3, 0.9 ppm) corresponding to different spectral components/proton moieties that collectively represent the total fat signal. The interactions through chemical bonds in the spectrum (spin coupling) result in the splitting of spectral peaks in doublets or triplets that in turn lead to signal changes of the coupled system. In particular, spin coupling evolution induces a sinusoidal modulation in addition to the T2 exponential decay of the echo train, resulting in a faster decay of the MR signal. Thus, when moving to imaging scale, fat appearance on conventional T2w Carr–Purcell–Meiboom–Gill (CPMG) images may vary significantly between different acquisition schemes, mainly depending on the time distance between consecutive 180 refocusing pulses (different ESP). Interaction between coupled spins present in fatty acid chain (hydrogen in methyl and methylene) introduce field inhomogeneities at a very local level, inducing thus an additional signal modulation to the exponential T2 decay. However, in the case of closely spaced radio-frequency pulses-small ESP- spin coupling related signal modulation

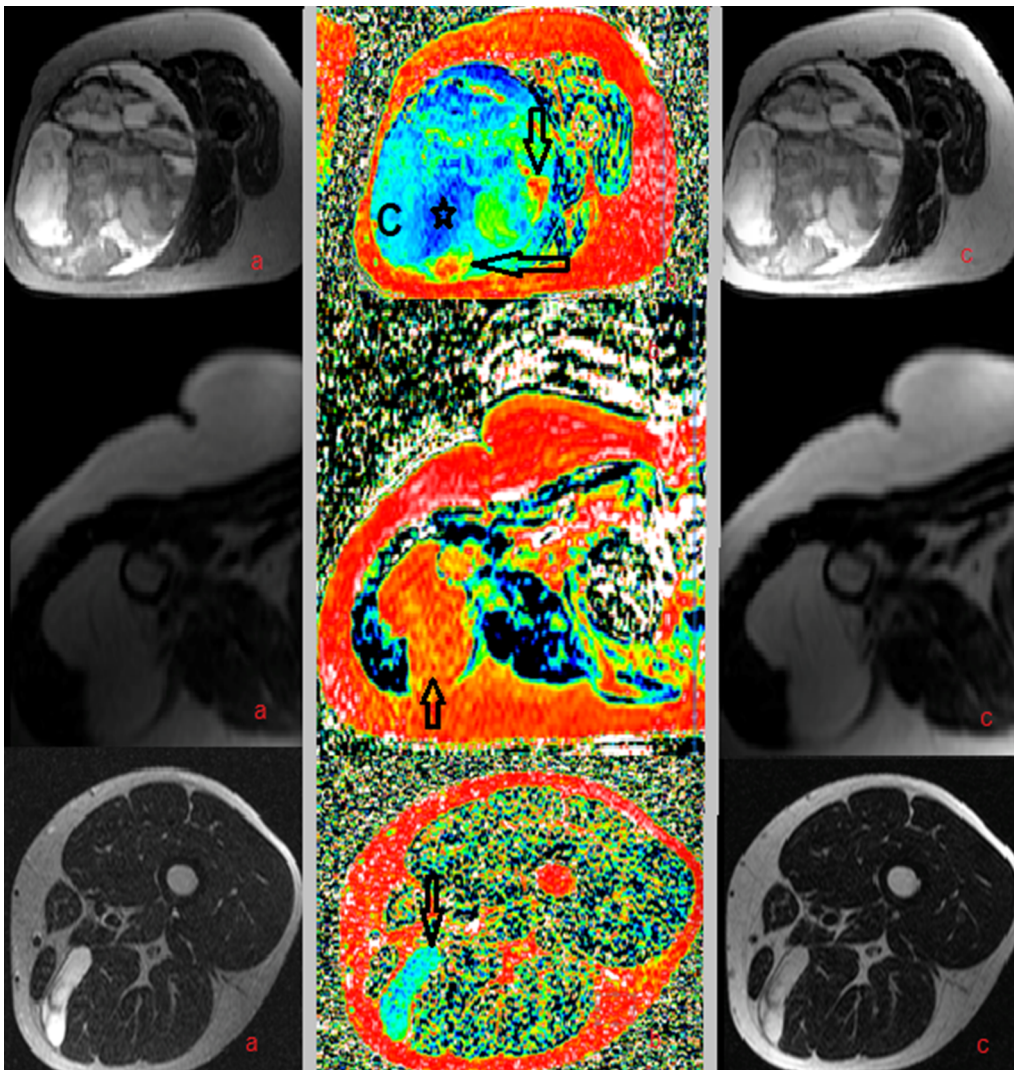


Fig. 2. SCratio maps for three lipomatous masses of variable degree of malignancy. Above: Dedifferentiated liposarcoma of the thigh: a) T2 MESE ESP: 26.8 ms, TE: 80.4 ms, b) SCr map [−10, 50] %, c) T2MESE ESP:13.4 ms TE: 80.4 ms. Histopathologic examination confirmed sites of well differentiation at the tumor periphery at locations 6o'clock and 3o' clock respectively at the periphery (arrows) that should be avoided for needle biopsy. Cystic components (C) were also observed and also sites of poor differentiation (asterisk). **Fig. 2 middle:** Benign Lipoma a) T2 MESE ESP: 26.8 ms, TE: 80.4 ms, b) SCr map [−10, 50], c) T2MESE ESP: 13.4 ms TE: 80.4 ms. **Fig. 2 below:** Myxoid Liposarcoma Lipoma a) T2 MESE ESP: 26.8 ms, TE: 80.4 ms, b) SCr map [−10, 50], c) T2MESE ESP:13.4 ms TE: 80.4 ms. All MR images are displayed at [0,1000] a.u.

(dephasing) is affected, resulting in slower relaxation rate and consequently brighter signal intensity of fat. [11]. An empirical threshold of 20 ms [12] referring to the inter pulse interval is reported, above which the fast rate of RF refocusing pulses decelerates spin coupling evolution and leads to bright fat appearance. Explicit explanation regarding the theory of multiple spin systems and the fat bi-phasic appearance can be found in references [13–15].

A phantom study from our team showed different amount of spin coupling related signal loss between oil samples of different botanical origin and thus different spectral identity, indicating that the specific inner structure of each oil sample relates to magnetic behavior of the fat and its appearance on T2w MRI [16]. The aim of the present study is to extend this research to the clinical field and examine the role of spin coupling and T2 relaxometry in supplementing pathognomonic evidence for the characterization of fat containing soft tissue masses.

2. Materials and Methods

2.1. Imaging protocol

All MRI exams were performed on a 1.5T MR scanner (Vision/Sonata hybrid System, Siemens, Erlangen, Germany). Conventional imaging sequences presented lesion location (dual echo Proton density and T2w TSE with fat suppression) in axial and coronal plane for localization of the lesion margins (TR/TE1/TE2/TI: 3360/14/83 msec,

5 mm slice thickness/0.5 mm gap, 19 slices) and functional imaging sequences showed tumor cellularity (8-b values 2D EPI DWI TR/TE: 2900/100 msec, 5 mm slice thickness/0 mm gap, b values: 0/50/100/150/200/500/800/1500, 19 axial slices) and vascularity (a dynamic 3D T1w fast low angle shot (FLASH) (TR/TE: 7.09/3.27msec, temporal resolution 7.09 sec 5 mm slice thickness/1.6 mm gap, 14 axial slices). Imaging planes were non-oblique for easier co-localization of imaging slice and site of histological examination.

The T2 quantitative MRI protocol consists of two 2D multislice MESE, PD-to-T2-weighted sequence were obtained with no interslice delay time. For the first sequence: $n = 25$ equidistant spin echoes with $TE_1 = 13.4$ ms, ESP = 13.4 ms and for the second $n = 10$, $TE_1 = 26.8$ ms, ESP = 26.8 ms while TR was 2500 ms for both sequences.. The latter sequence (10 echoes: 26.8, ..., 80.4, ..., 268 ms) was used for T2 relaxometry as it does not suffer from the bright fat appearance from spin coupling while the former sequence (25 TEs: 13.4, 26.8, ..., 80.4, ..., 335) was used for subtraction of images between the two relaxometry sequences at identical echo times. Fourteen axial slices of 5 mm slice thickness and 5 mm interslice distance were obtained. A rectangular field of view (280 × 210 mm) with a rectangular reconstruction matrix (256 × 192 pixels) was utilized. The final 3D spatial resolution was therefore: $1.1 \times 1.1 \times 8$ mm³. The MESE sequence was based on a 2D multiecho CPMG spin echo sequence with alternating 180 degrees RF pulses under the phase-alternating-phase-shift (PHAPS) scheme [17]. A selective refocusing RF pulse scheme was

Table 1

T2, T2*, Spin coupling percentage (SC) and Spin Coupling ratio (SCr) for 5 lipomas, 1 hibernoma (not included in further statistics), 4 well differentiated liposarcomas (wdls), 3 myxoid liposarcomas (mls), 2 pleomorphic liposarcomas and 4 poorly differentiated liposarcomas (pdls). Subscripts l and sf declare lesion and subcutaneous fat respectively. SCr is the ratio of spin coupling loss of the lesion over the same value of uninvolved healthy fat of the same acquisition. SD = Standard Deviation.

	T2l (ms)	T2sf (ms)	T2* _l (ms)	T2* _{sf} (ms)	SCL (%)	SCsf (%)	SCr l
lipoma 1	104,9	102,8	31,4	29,8	39,9	40,4	0,99
lipoma 2	100,4	100,9	29,2	28,0	41,3	42,0	0,98
lipoma 3	103,6	96,9	30,8	30,6	37,8	36,9	1,02
lipoma 4	102,3	99,6	28,6	29,5	38,7	36,2	1,07
lipoma 5	103,5	98,0	30,4	30,6	40,1	39,8	1,01
Mean	102,9	99,6	30,1	29,7	39,6	39,1	1,01
SD	1,5	2,1	1,0	1,0	1,2	2,2	0,03
hibernoma	196,7	96,5	103,7	29,2	-0,4	35,2	-0,01
wdls 1	103,4	99,7	44,6	29,8	36,7	39,8	0,92
wdls 2	102,5	98,7	28,8	28,5	37,1	39,7	0,93
wdls 3	101,5	98,2	31,7	29,3	49,0	51,8	0,95
wdls 4	105,5	102,0	57,3	28,4	31,9	40,3	0,79
Mean	103,2	99,7	40,6	29,0	38,7	42,9	0,90
SD	1,7	1,5	11,3	0,6	6,3	5,1	0,1
mls 1	572,0	99,5	287,0	32,0	0,2	40,5	0,00
mls 2	535,1	99,4	370,7	29,6	0,1	36,9	0,00
mls 3	383,8	100,5	282,4	28,8	7,3	41,7	0,18
Mean	497,0	99,8	313,4	30,1	2,5	39,7	0,06
SD	99,7	0,6	49,7	1,7	4,1	2,5	0,1
pls 1	144,6	100,2	78,6	28,5	6,1	34,9	0,17
pls 2	135,4	104,7	90,1	29,0	0,0	34,1	0,00
Mean	140,0	102,5	84,4	28,8	3,1	34,5	0,09
SD	6,5	3,2	8,1	0,4	4,3	0,6	0,1
pdls 1	145,4	100,7	69,3	27,1	-20,1	32,1	-0,62
pdls 2	169,3	94,9	129,5	29,5	-6,2	41,4	-0,15
pdls 3	144,3	100,5	84,4	28,8	-12,6	45	-0,28
pdls 4	131,9	99,7	59,4	30,2	-7,1	41,8	-0,17
Mean	147,7	98,9	85,6	28,9	-11,5	40,1	-0,3
SD	15,6	2,7	31,0	1,3	6,4	5,6	0,2

Table 2

Classification performance for T2, T2*, SC and SCr between lipomatous tumors. p-value is marked by “*”, “**”, “***”, and “ns” for values between [0.01–0.05], [0.001–0.01], [0–0.001] and [0.05–1] respectively.

T2	lipoma	wdls	mls	pls	SC	lipoma	wdls	mls	pls
wdls	ns				wdls	ns			
mls	***	***			mls	***	***		
pls	ns	ns	***		pls	***	***	ns	
pdls	ns	ns	***	ns	pdls	***	***	*	ns
T2*					SCr				
wdls	ns				wdls	ns			
mls	***	***			mls	***	***		
pls	ns	ns	***		pls	***	***	ns	
pdls	ns	ns	***	ns	pdls	***	***	*	*

utilized. Additionally, a multi echo T2* MEGRE with 4 in phase echoes (4.77, 9.59, 14.41, 19.23) and 4 out of phase echoes (2.38, 7.18, 12, 16.82) was used for the calculation of T2* maps.

2.2. Data post processing

Pixel based parametric T2/T2* maps were produced after mono-exponential fitting of the multi echo MESE/MEGRE data from in-house built software platform [18]. Mean T2/T2* was calculated for each Region of Interest (ROI) which was delineated by an expert radiologist within the tumor central slice at a homogeneous region, excluding necrosis and hemorrhage. In the case of dedifferentiated liposarcoma, ROI delineation was performed after the pathologist suggested areas of poor differentiation. Image based calculations (subtraction and division of T2MESE images to calculate relative signal loss at identical TE) were performed with Mango software (Mango Software, Research Imaging Institute, UTHSCSA). Statistical analysis was performed using R. Each

examined biomarker was descriptively summarized and presented as mean ± standard deviation (SD). Pairwise comparisons were assessed quantitatively using Student’s T-test. Boxplots depicting the different subject groups were displayed. For all tests, a p-value of less than 0.05 was considered to indicate statistical significance.

2.3. Patient population – histological correlation

Twenty patients with lipomatous tumors underwent MRI from July 2017 to May 2018 prior to the planned surgical excision. One patient was excluded because of compromised cooperation resulting in severe motion artifacts. All patients signed an informed consent for the use of clinical and imaging data for research purposes. Surgeon marked the specimen with sutures in predefined points in order to enable the actual three-dimensional orientation of the specimen in relation with the patient’s body and to warrant the implementation of sections of the tumor in its true axial plane. The intact surgical specimen was transported promptly to the pathology department, where it was delivered to and handled by a trained pathologist who performed the gross examination, photographed and marked the specimen with permanent ink according to the surgical markings and margins. Furthermore, after identifying the upper and lower margins of the tumor, in the superior-inferior direction, parallel sections perpendicular to the axial plane of 1 cm thickness were taken. The central slice of the tumor, corresponding to the lesion’s central imaging slice, was selected after measuring the distances from the upper and lower margins, was divided in orthogonal slabs (in a grid-manner), and placed into plastic cassettes (Fig. 1). Tumor tissue sections were processed according to CAP guidelines and recommendations for specimen handling [19]. In brief after 48 h’ fixation into 10% neutral buffered formalin, sections were embedded into paraffin, dehydrated through a series of graded ethanol baths, infiltrated with wax and then embedded into wax blocks. 4 μm thick

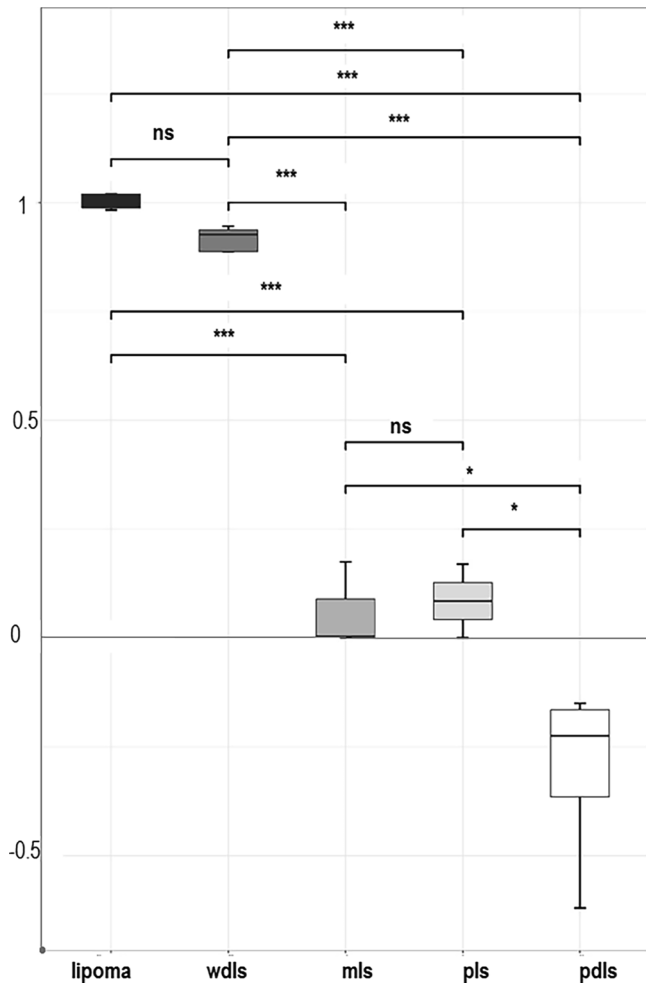


Fig. 3. Box plot graphically representing mean value and standard deviation for each category based on SCr. for all lipomatous tumor types. p-value is marked by “”, “*”, “**”, and “***” for values between [0.01–0.05], [0.001–0.01], [0–0.001] and [0.05–1] respectively.

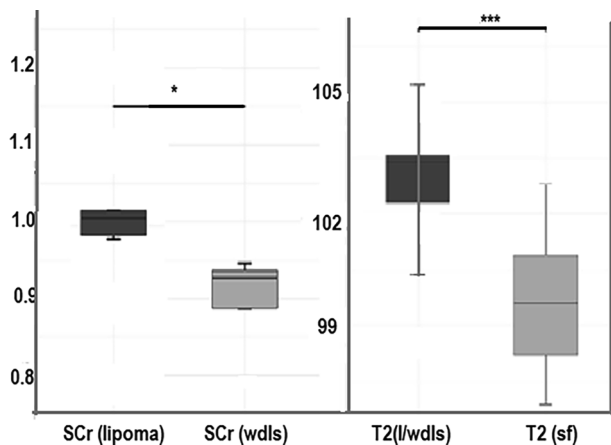


Fig. 4. Classification problem simplified to two categories. Left: Significant difference is found between lipoma and well differentiated liposarcoma based on SCr. Right: Lipoma or well differentiated liposarcoma have significant differences in measured T2 value from uninvolved subcutaneous fat (sf).

sections of each tumor slab were cut, placed into glass slides, stained with H/E and examined microscopically (Nikon Eclipse E-200) in order to characterize each area of the central tumor slice in terms of differentiation, cell type, cellular atypia, cellularity, mitotic activity,

vascularity and presence of necrosis.

The histopathologic topographic characterization guided the imaging post-processing stage so as to recognize the histologically designated “benign”, “necrotic”, malignant areas and also to conclude on differentiation grade on a very locally restricted area which could be used for ROI measurements. The corresponding site was located on the central imaging slice as distance from the center and angle in a virtual axially located 360 degree cycle.

A case of hibernoma was included in the patient cohort because of its interest but was not included in the statistical analysis as it cannot constitute a category by itself. Data from patients diagnosed with dedifferentiated liposarcoma were assigned as either well or poorly differentiated tissue according to the result of histological examination for the selected slice.

The relative signal loss percentage of the fatty tissue between two T2 acquisitions of different echo spacing, 13.4 ms and 26.8 ms respectively was calculated (Spin Coupling, SC) for all image pixels (Eq. (1)).

$$SC = \frac{T2_1 - T2_2}{T2_1} \quad (1)$$

SC value calculated for the tumor ROI was then divided by SC value calculated for subcutaneous fat ROI of the same patient from the same acquisition in order to produce a patient specific metric, Spin Coupling ratio, (SCr) (Eq. (2)).

$$SC_{ratio} = \frac{SC_{tumor}}{SC_{fat}} \quad (2)$$

3. Results

Resulting pixel based parametric maps of SCr are shown on Fig. 2, complemented by original bright and dark fat T2w images, ROI based mean apparent T2, mean apparent T2* were calculated for the lesion as well as for uninvolved fat adjacent to the tumor volume to be used as reference for protocol robustness (Table 1). Subcutaneous fat sustains a relatively constant value for mean apparent T2/T2* within the patient population, unlike fat containing tumors that exhibit an extensive range of values. Similarly SCr remains relatively constant for healthy fat among all patients while there is a significant range of measured values between different types of fat containing neoplasms.

Statistical analysis (pairwise t-test with Bonferroni correction) was performed to find significant differences in mean apparent T2, mean apparent T2* and SCr between five distinct categories, i.e lipoma, well differentiated liposarcoma, myxoid liposarcoma, pleomorphic liposarcomas and poorly differentiated liposarcoma. Difference was considered significant for p less than 0.05, and is marked by “” for p between [0.01–0.05], “*” for p [0.001–0.01] and lastly marked with “***” for p between [0–0.001] as shown in Table 2. Non-significant differences are noted as ns. Fig. 3 graphically represents SCr results, as this was proved (from results shown on Table 2) the metric with the higher discriminative power among all three.

It is of note that only SCratio succeeded in classification between pleomorphic liposarcoma and poorly differentiated part of dedifferentiated liposarcoma, both of which are graded as highly malignant (histologic specific grade: 3) and have similar imaging characteristics.

No metric could find significant differences between lipoma and well differentiated liposarcoma in the 5-class problem. However, when performing a 2-class classification between the two classes of low malignancy and very similar imaging characteristics, SCr shows significant differences between lipoma and well differentiated liposarcoma while all the other metrics fail (Fig. 4 left).

Furthermore a pairwise t-test was performed between an “extended” class including two entities (lipoma and well differentiated liposarcoma) tested versus healthy subcutaneous fat visible in the same acquisition based on T2 relaxation constant. Significant differences are found between tumors and normal appearing adjacent fatty tissue

(Fig. 4 right).

4. Discussion

Fat quantification and fat content determination has been a long standing target of quantitative MRI. To our knowledge, the first use of spin coupling as contrast for clinical imaging was published in 1993 [20].

Currently, the most widely used NMR based method for the study of tissue structure is in vivo MR spectroscopy. It offers direct recognition of each spectral peak and its relative amplitude for a given sample, but it has many inherent constraints that prevent extensive use in a routine basis. It requires special software and post processing, human expertise, adequate sample homogeneity and main field homogeneity. Ex-vivo ^{13}C MRS has been used by S. Singer et al to differentiate between fat-containing tumors based on tissue biochemistry [21]. The major findings of this study were significant differences in the fatty acyl chain content (ratio between lipomas: wdl: pls or dediff. liposarcomas is 1 : 3 : 0.01) probably attributed to the increase of the poly-unsaturation degree of high grade sarcomas as compared to intermediate or low grade. The latter suggests an increase in the number of double bonds present in the fatty acyl chain which affects the motion and order of the acyl chain and in turn affects membrane proteins. This can be an important factor determining the invasive and metastatic capacity of the high grade liposarcoma cell types. Moreover they remarked the presence of free fatty acids and phospholipids in dedifferentiated/pleomorphic sarcomas which were not detectable in normal fat, lipoma or well differentiated liposarcoma.

The proposed method based on spin coupling ratio does not rely on direct detection of tissue composition but taking into account the biochemical differences observed in the spectrum, changes in lipid specific imaging contrast are expected. Differences in the measured SCr show variable degree of dependence on refocusing pulse spacing and may be indicative of differences in the fat content of adipocytic neoplasms. Subcutaneous fat exhibits a very narrow and specific range of all T2 and Spin Coupling related metrics instead in the resulting changes of signal produced. SCr calculation does not require special hardware or software nor post processing expertise. It requires minimal acquisition time and has excellent spatial resolution, exploiting rather than being weakened by tissue heterogeneity as in the case of MR spectroscopy.

Results of the present study show that T2 relaxometry in conjunction with spin coupling ratio can achieve differentiation between any pair of the five different adipocytic moieties. As seen in Fig. 3 SCr decreases with increased differentiation grade. Well differentiated liposarcomas lose a significant percentage (38.9%) of their signal due to spin coupling at TE = 80 ms which is comparable to normal fat signal loss (42.9%), myxoid have almost identical signal intensity between the two acquisitions-probably because of the dominant long T2 component and, at the other end, pleomorphic and poorly differentiated tumors have even lower SCr. In fact, the latter group exhibits negative values which was unexpected as zero loss was considered to be the lower limit by theory. However this finding was consistent among all examined patients and requires more detailed study in a molecular and chemical level.

In FSE each echo has a distinct phase encoding in order to represent a different line of k-space within a given TR interval. The effect of spin coupling in signal modulation cannot be decomposed and measured separately to other concurrent spin dephasing phenomena during acquisition, such as magnetization exchange effects, stimulated echoes or diffusion of water molecules through a local field inhomogeneities [22]. However, the process of subtraction of images with identical parameters apart from ESP accentuates contrast mechanisms affected significantly by pulse spacing. For this reason, we believe that, if not uniquely, the observed differences can be attributed mainly to spin coupling.

A definite constrain of our study is the number of patients that

participated in the study but these preliminary results show that SCr can be introduced into the clinical routine and to build a larger database for use in the future. However it is promising that structures of similar origin but different molecular inner structure or composition have a different imaging identity and the proposed biomarker of spin coupling ratio highlights the imaging spectrum of fat that remains otherwise unperceivable.

In conclusion, the novel biomarker SCr can be introduced as a quantitative adjunct for radiological assessment of lipomatous tissue type and grade with minimal software and time prerequisites. Clinical implications of this MRI technique may be biopsy guidance in heterogeneous lipomatous tumors to assure for harvesting tissue with the highest malignancy grade and non-invasive preoperative diagnosis of tumor type and grade, which is essential for adequate treatment planning.

References

- [1] Nassif NA, Tseng W, Borges C, Chen P, Eisenberg B. Recent advances in the management of liposarcoma. *F1000Res* 2016;5:2907. <https://doi.org/10.12688/f1000research.10050.1>.
- [2] Gupta P, Potti TA, Wuertzer SD, Lenchik L, Pacholke DA. Spectrum of fat-containing soft-tissue masses at mr imaging: the common, the uncommon, the characteristic, and the sometimes confusing. *RadioGraphics* 2016;36:753–66. <https://doi.org/10.1148/rg.2016150133>.
- [3] Nishida J, Morita T, Ogose A, Okada K, Kakizaki H, Tajino T, et al. Imaging characteristics of deep-seated lipomatous tumors: intramuscular lipoma, intermuscular lipoma, and lipoma-like liposarcoma. *J Orthop Sci* 2007;12:533–41. <https://doi.org/10.1007/S00776-007-1177-3>.
- [4] Santos PM, Vinicius F, Kock C, Santos MS, Lobo CMS, Carvalho AS, et al. Non-invasive detection of adulterated olive oil in full bottles using time-domain NMR relaxometry. *Artic J Braz Chem Soc* 2017;28:385–90. <https://doi.org/10.5935/0103-5053.20160188>.
- [5] Loskutov V, Zhakov S. Dependence of the liquid transverse relaxation time T2 in porous media on fluid flow velocity. *Int J Heat Mass Transf* 2016;101:692–8. <https://doi.org/10.1016/J.IJHEATMASSTRANSFER.2016.05.057>.
- [6] Maris TG, Pappas E, Boursianis T, Kalaitzakis G, Papanikolaou N, Watts L, et al. 3D polymer gel MRI dosimetry using a 2D haste, A 2D TSE AND A 2D SE multi echo (ME) T2 relaxometric sequences: Comparison of dosimetric results. *Phys Medica* 2016;32:238–9. <https://doi.org/10.1016/J.EJMP.2016.07.498>.
- [7] Brix G, Heiland S, Bellemann ME, Koch T, Lorenz WJ. MR imaging of fat-containing tissues: valuation of two quantitative imaging techniques in comparison with localized proton spectroscopy. *Magn Reson Imaging* 1993;11:977–91. [https://doi.org/10.1016/0730-725X\(93\)90217-2](https://doi.org/10.1016/0730-725X(93)90217-2).
- [8] Hamilton G, Smith DL, Bydder M, Nayak KS, Hu HH, Hu HH. MR properties of brown and white adipose tissues. *J Magn Reson Imaging* 2011;34:468–73. <https://doi.org/10.1002/jmri.22623>.
- [9] He T, Gatehouse PD, Smith GC, Mohiaddin RH, Pennell DJ, Firmin DN. Myocardial T2' measurements in iron-overloaded thalassemia: An in vivo study to investigate optimal methods of quantification. *Magn Reson Med* 2008;60:1082–9. <https://doi.org/10.1002/mrm.21744>.
- [10] Hardy PA, Henkelman RM, Bishop JE, Poon ECS, Plewes DB. Why fat is bright in rare and fast spin-echo imaging. *J Magn Reson Imaging* 1992;2:533–40. <https://doi.org/10.1002/jmri.1880020511>.
- [11] Yahya A, Tessier AG, Fallone BG. Effect of J-coupling on lipid composition determination with localized proton magnetic resonance spectroscopy at 9.4 T. *J Magn Reson Imaging* 2011;34:1388–96. <https://doi.org/10.1002/jmri.22792>.
- [12] Stables LA, Kennan RP, Anderson AW, Gore JC. Density matrix simulations of the effects of j coupling in spin echo and fast spin echo imaging. *J Magn Reson* 1999;140:305–14. <https://doi.org/10.1006/JMRE.1998.1655>.
- [13] Hennig J, Thiel T, Speck O. Improved sensitivity to overlapping multiplet signals in in vivo proton spectroscopy using a multiecho volume selective (CPRESS) experiment. *Magn Reson Med* 1997;37:816–20. <https://doi.org/10.1002/mrm.1910370603>.
- [14] Allerhand A, Thiele E. Analysis of carr–purcell spin-echo nmr experiments on multiple-spin systems. II. The effect of chemical exchange. *J Chem Phys* 1966;45:902–16. <https://doi.org/10.1063/1.1727703>.
- [15] de Graaf RA, Rothman DL. In vivo detection and quantification of scalar coupled 1H NMR resonances. *Concepts Magn Reson* 2001;13:32–76. [https://doi.org/10.1002/1099-0534\(2001\)13:1<32::AID-CMR4>3.0.CO;2-J](https://doi.org/10.1002/1099-0534(2001)13:1<32::AID-CMR4>3.0.CO;2-J).
- [16] Nikiforaki K, Manikis GC, Boursianis T, Marias K, Karantanas A, Maris TG. The impact of spin coupling signal loss on fat content characterization in multi-echo acquisitions with different echo spacing. *Magn Reson Imaging* 2017;38. <https://doi.org/10.1016/j.mri.2016.12.011>.
- [17] Fransson A, Ericsson A, Jung B, Sperber GO. Properties of the PHase-Alternating Phase-Shift (PHAPS) multiple spin-echo protocol in MRI: a study of the effects of imperfect RF pulses. *Magn Reson Imaging* 1993;11:771–84. [https://doi.org/10.1016/0730-725X\(93\)90195-J](https://doi.org/10.1016/0730-725X(93)90195-J).
- [18] Manikis GC, Nikiforaki K, Papanikolaou N, Marias K. Diffusion Modelling Tool (DMT) for the analysis of Diffusion Weighted Imaging (DWI) Magnetic Resonance

- Imaging (MRI) data. Proc. 33rd Comput. Graph. Int. – CGI '16 New York, New York, USA: ACM Press; 2016. p. 97–100. <https://doi.org/10.1145/2949035.2949060>.
- [19] Lester SC. *Manual of surgical pathology*. Saunders/Elsevier 2010.
- [20] Todd Constable R, Smith RC, Gore JC. Coupled-spin fast spin-echo MR imaging. *J Magn Reson Imaging* 1993;3:547–52. <https://doi.org/10.1002/jmri.1880030319>.
- [21] Singer S, Millis K, Souza K, Fletcher C. Correlation of lipid content and composition with liposarcoma histology and grade. *Ann Surg Oncol* 1997;4:557–63. <https://doi.org/10.1007/BF02305536>.
- [22] Constable RT, Anderson AW, Zhong J, Gore JC. Factors influencing contrast in fast spin-echo MR imaging. *Magn Reson Imaging* 1992;10:497–511. [https://doi.org/10.1016/0730-725X\(92\)90001-G](https://doi.org/10.1016/0730-725X(92)90001-G).